# PYROELECTROCHEMICAL CELL – A DIRECT THERMAL TO ELECTROCHEMICAL ENERGY CONVERSION DEVICE

by

Fariha Tasnim Khan

A dissertation submitted to the faculty of
The University of Utah
in partial fulfillment of the requirements for the degree of

Doctor of Philosophy

Department of Electrical and Computer Engineering

The University of Utah

May 2022

Copyright © Fariha Tasnim Khan 2022

All Rights Reserved

# The University of Utah Graduate School

# STATEMENT OF DISSERTATION APPROVAL

The dissertation of		Fariha Tasnim Khan			
has been approved by the following supervisory committee members:					
	Shadrach J. Roundy		, Chair	01/28/2022  Date Approved	
	Roseanne Warren		, Member	01/28/2022  Date Approved	
	Florian Solzbacher		, Member	01/28/2022  Date Approved	
	Bruce K. Gale		, Member	01/31/2022  Date Approved	
	Prashant Tathireddy		, Member	02/02/2022  Date Approved	
	Darrin J. Young		, Member		
and by	Floriar	ı Solzbacher		, Chair/Dean of	
the Department	/College/School of	Electrical a	and Computer	· Engineering	
and by David B	. Kieda, Dean of The Gra	aduate School.			

#### **ABSTRACT**

The maintenance and replacement of batteries can be a time-consuming and expensive task that limits the deployment of large-scale wireless networks for the Internet of Things (IoT). Replacing or supplementing batteries with energy harvesting units can enable self-sustaining systems for maintenance-free infinite-life power for modern wireless systems. The broad goal of this research is to explore a new mechanism and structure for integrated thermal energy harvesting and electrochemical storage called a pyroelectrochemical cell (PEC). The pyroelectric properties of PVDF-BaTiO<sub>3</sub> composite films are utilized to harvest low-grade thermal energy (<200°C). The composite film replaces commercial polyethylene (PE) separators in an electrochemical cell. As the cell is heated or cooled, the pyroelectric effect of the separator creates an electric field which serves as the driving force to charge the cell. A comprehensive study on developing an electroactive composite film with through-pores to enable free ion migration in the cell has been presented here. The design and construction of cells to both demonstrate the PEC working mechanism and enable high-temperature electrochemical cell study for relevant applications has been detailed in this research. The charging-discharging mechanism of the PEC under heating cycles has been investigated to demonstrate the proof-of-concept. The stored energy and conversion efficiency of the PEC has been presented to show the scope for this new self-sustaining energy harvesting technology.



# TABLE OF CONTENTS

ABSTRACT	iii
LIST OF TABLES	Vii
ACKNOWLEDGMENTS	viii
Chapters	
1. INTRODUCTION	1
1.1 Motivation	1
1.2 Pyroelectric Energy Harvesters	
1.3 Integrated Self-Charging Cells	
1.4 Thermal Effects on Electrochemical Cells	
1.5 Research Objectives	10
1.6 Dissertation Overview	13
1.7 References	15
2. STRETCHING-INDUCED PHASE TRANSITIONS IN PVDF-BATIO <sub>3</sub> FLEXIB COMPOSITE PIEZOELECTRIC FILMS	
2.1 Introduction	25
2.2 Methods	
2.3 Uniaxial Stretching of Composite Films.	
2.4 Analysis of Electroactive Phase Content	
2.5 Qualitative Comparison of FTIR and XRD Data	
2.6 Conclusion and Summary	
2.7 References	
3. EFFECT OF PORE STRUCTURE ON THE PIEZOELECTRIC PROPERTIES OF PVDF-BATIO <sub>3</sub> COMPOSITE FILMS	43
3.1 Introduction.	43
3.2 Methods	
3.3 Results and Discussion	
3.4 Conclusion and Summary	
2.5 Pafaranag	

4. DESIGN OF HEATED CELLS FOR IN-SITU ABSORPTION AND	
REFLECTANCE UV-VIS SPECTROELECTROCHEMISTRY	64
4.1 Introduction	64
4.2 Experimental	
4.3 Results and Discussion	
4.4 Conclusion	
4.5 References	
5. HYBRIDIZATION OF THERMAL ENERGY HARVESTING IN A	
PYROELECTROCHEMICAL CELL	78
5.1 Introduction	
5.2. Methods	80
5.3 Results	84
5.4 Theory of PEC Operation	89
5.5 Conclusion	
5.6 References	
6. CONCLUSION	103
6.1 Future Work	105
6.2 References	108
APPENDIX A. QUANTIFICATION OF β AND γ PHASES	110
APPENDIX B. MANUFACTURING DETAILS	117

# LIST OF TABLES

# Tables

1.1. Pyroelectric coefficient of some common materials	. 22
2.1. Quantitative comparison of electroactive phase content	. 39
3.1. Average film porosity and Young's modulus measurements of PVDF-BaTiO <sub>3</sub> films prepared under varying coagulation bath conditions compared with commercial, non-porous PVDF.	
4.1. Sealing pressure and temperature test results for cuvette and disc cell designs	. 74
5.1. Energization time, ramp rate, voltage, and energy generated per cycle in the three-electrode cell.	
A.1. Calculated F (β) content in the composite films using Equation A.2	114
B.1. Cuvette cell bill-of-materials	118
B 2 Disc cell bill-of-materials	119

#### ACKNOWLEDGMENTS

I would like to acknowledge all the people who have made this journey possible and a memorable one. First, I would like to express my sincere gratitude to my advisors Dr. Shad Roundy and Dr. Roseanne Warren. Their guidance, support, and patience have made this journey possible. They have mentored me to become a better researcher and have supported me in my goals.

I would like to say thanks to my committee members for their valuable time and guidance. I would like to acknowledge the technical advice and supports from Steve Prichett, Paulo Perez, Brian Van Devener (Utah Nanofab), and Kim Watts (Material Characterization Lab) throughout my research work.

I would like to thank my lab mates from both Integrated Self-Powered Sensing lab (ISS) and Advanced Energy Innovations Lab (AEIL) for their support. They were always happy to help and eager to answer any questions I had. Particularly, I would like to mention my fellow project mate, Tim Kowalchik, for his support. I would like to acknowledge my friends who mentally supported me. Thanks to my husband for his encouragement and motivation through this long journey here in Utah.

Lastly, I would like to acknowledge my parents. Whatever I have achieved or will achieve in life is because of them. Nothing can comprehend the support and encouragement they have given me all my life. In addition, I would like to acknowledge the financial support from National Science Foundation (NSF) for this research work.

#### CHAPTER 1

#### INTRODUCTION

# 1.1 Motivation

Energy harvesting can collect free ambient energy from the environment for use by low energy/low power devices. Energy harvesting systems are particularly interesting for applications utilizing networks of wireless sensors, such as those that make up the Internet-of-Things (IoT). The maintenance and replacement of batteries can be a time-consuming and expensive task that limits the deployment of large-scale wireless networks. Replacing or supplementing batteries with energy harvesting units can provide self-sustaining systems for maintenance-free infinite-life power for wireless systems. This research aims to explore a new mechanism and structure for integrated thermal energy harvesting and electrochemical storage. We call this new structure the pyroelectrochemical cell (PEC).

Although the goal of the research presented in this dissertation is to explore this new type of energy harvesting and storage mechanism to understand its potential, and not necessarily to power any specific end system, it is important to keep potential end-use scenarios in mind. In order to be useful, an energy harvester should supply enough power, on average, to support the critical function of the system it powers. That function is typically to make a measurement and transmit the resulting data point. Many systems

currently exist for which a single sensing and data transmission operation requires 35-300 μJ or less [1]–[4]. The average power consumption of an industrial ISO standard mesh networking protocol device is about 2.2 mW [3], however, many research systems consume less. Even at 2 mW power usage, an energy budget of approximately 100 µJ per operation leaves 50 ms to take and transmit a measurement, which is reasonable. Li et al. demonstrated an ultra-low-power node controlling system-on-chip for IoT networks with a minimum power requirement of 85 nW at 0.45 V [5]. Rabaey et al. developed a lowpower node (PicoRadio) enabling an ad- hoc wireless network with power dissipation level <100 µW [6]. The active power of an existing transmitters using ultra low power receivers can be limited to <100 µW [7]. Most energy harvesting powered systems have an intermediate energy storage reservoir, a rechargeable battery, or supercapacitor, which is charged by the energy harvester. It is important to note that, unlike a cell phone, this battery or supercapacitor is typically never completely depleted and then recharged, but is kept at some intermediate state-of-charge by slow recharging from the energy harvester. This is the type of operation we envision for the PEC. Temperature changes would periodically boost the charge state of the integrated electrochemical cell enabling continuous operation.

Low-grade thermal energy (<200 °C) can be harvested using thermoelectric and pyroelectric materials. Thermoelectric materials utilize a spatial temperature difference to generate an electric field by the Seebeck effect. Pyroelectric materials have spontaneous polarization that changes with a temporal thermal gradient (Figure 1.1) [8]. The increase/decrease in temperature with time impacts the thermal vibration of the dipoles in the polar dielectric material. Increased thermal vibration causes a reduced polarization and generates a voltage across the material. The opposite phenomenon occurs when the

temperature is decreased. The pyroelectric effect is reversible and the generated voltage is temporary due to internal leakage currents. The dipoles stabilize again at their equilibrium position when the temperature returns to the original temperature. Alternatively, if the temperature settles at the new temperature, the generated voltage diminishes through leakage current. Figure 1.1a shows a pyroelectric material at equilibrium temperature. Figures 1.1b and 1.1c show the polarization change with increasing (dT/dt > 0) and decreasing (dT/dt < 0) temperature gradients with time, respectively. When the pyroelectric material is connected to an external circuit, surface charges arise on the pyroelectric material's surface to attain charge neutrality, screening the thermally-induced polarization and generating an electric field across the material. A pyroelectric energy harvesting system is promising for environments where the device is subjected to temperature changes or intermittent temperature fluctuations throughout the day. For instance, the temperature changes 2 °C per 1000 ft when an airplane takes off/lands [9]. Low-grade waste heat is also generated in almost every mechanical system. Pyroelectric energy harvesters can provide solutions to harvest this intermittent thermal energy at low-cost.

# 1.2 Pyroelectric Energy Harvesters

Recently, many researchers have demonstrated flexible pyroelectric or hybrid pyropiezoelectric energy harvesters [8], [10]–[13]. Dalola et al. demonstrated a thick PZT film based thermal energy harvester to supply low power autonomous sensor systems [14]. Fang et al. demonstrated a device using porous poly(vinylidene fluoride–trifluoroethylene) (PVDF- TrFE) achieved a 0.2% efficiency and a 0.84 mWcm<sup>-2</sup> electrical power output for  $\Delta T$ = 115 °C between the sources [10]. The effectiveness of pyroelectric materials is

characterized by their ability to generate charge density when temperature changes 1 °C. The pyroelectric coefficient is defined as the net change in spontaneous polarization of materials resulting from a change in temperature [15]. Equation 1.1 shows the pyroelectric coefficient where  $P_s$  is the spontaneous polarization and Equation 1.2 relates the output voltage to the load resistance and pyroelectric coefficient in the system.

$$p = \frac{dP_S}{dt} \tag{1.1}$$

$$V_o = pA \frac{dT}{dt} R \tag{1.2}$$

where  $V_o$  is load voltage, R is the load resistance, p is the pyroelectric coefficient, A is the sample surface area, and  $\frac{dT}{dt}$  is the temperature ramp rate. The open circuit voltage depends on the pyroelectric coefficient and higher voltage leads to higher efficiency of the system. Pyroelectric energy harvesters have been limited by their low energy conversion efficiencies due to low pyroelectric coefficients, and low thermal conductivities of the materials. Low thermal conductivity can lead to decreased temperature ramp of the separator and thus decreased pyroelectric field across the separator. However, several approaches have been implemented for new materials (copolymers, composite structures, structure-controlled polymers) with higher pyroelectric coefficients and functional designs of harvesters to increase heat conductivity of the system [16]–[18]. Table 1.1 shows some common pyroelectric materials used in previous studies.

Ferroelectric polyvinylidene difluoride (PVDF) and its copolymers have attracted a lot of attention as a low cost, flexible pyroelectric material [12], [19]–[21]. PVDF polymer is easy to fabricate and has been used as thin films, nanowires and nanofibers [8], [22]. In the case of nanowires and nanofibers, the high electric field applied during the

electrospinning process increases the electroactive phase content in PVDF fibers [23]–[26]. Also, ceramic fillers (i.e., Barium Titanate (BaTiO<sub>3</sub>), Lithium Niobate (LiNbO<sub>3</sub>), Zinc Oxide (ZnO)) provide nucleation sites and have been shown to increase pyroelectric performance in PVDF polymer by ceramic-polymer surface interactions [27], [28]. Moreover, perovskite-structured ferroelectric ceramics (i.e. BaTiO<sub>3</sub>, Lead Zirconate (PZT)) have high dielectric constant and pyroelectric properties [8], [29]. These ceramic fillers can increase the energy density of PVDF nanogenerators by complementing their pyroelectric performance. Additionally, mechanical stretching (2-5x) of PVDF polymer has also been applied to increase electroactive phase content [27], [30], [31], and therefore improve the pyroelectric coefficient.

BaTiO<sub>3</sub> is a lead-free ceramic particle which has high piezoelectric and pyroelectric coefficients. PVDF- BaTiO<sub>3</sub> has a 0-3 connectivity which enables flexible structure formation and there are facile methods available for fabrication of this composite. The properties (piezoelectric coefficient, Young's modulus, dielectric constant) of PVDF-BaTiO<sub>3</sub> composite can be easily manipulated for specific applications. BaTiO<sub>3</sub> particles also lowers the required poling voltage to orient the dipoles in the composite structure. For the demonstration of the PEC, we decided to use this composite structure to increase the pyroelectric coefficient of the separator and thus the harvested energy density of the device while maintaining the flexibility of the electrochemical separator.

# 1.3 Integrated Self-Charging Cells

Any energy harvesting system constitutes at least two major parts: a generation unit to convert different types of energy to electrical energy and a storage unit to store the electrical energy as chemical energy in an electrochemical cell [32], [33]. These two separate physical units are based on two distinct physical phenomena. An additional signal conditioning circuit (i.e., rectifiers, amplifier) increases the overall size and complexity of the system. There has been growing interest in the hybridization of the two units–energy harvesting and storage–in a single device. Researchers have demonstrated self-charging systems for triboelectric [32], [34], solar [35], [36] and chemical energy harvesting [37], [38]. Wang et al. demonstrated a self-charging power cell utilizing the piezoelectric nature of PVDF. They harvested low-frequency mechanical vibration and simultaneously stored the energy in an electrochemical cell by replacing the separator of the cell with a piezoelectric PVDF thin film [39], [40]. To date, no one has demonstrated integration of thermal energy harvesting via pyroelectric materials with electrochemical energy storage.

In this dissertation, we explore the use of the pyroelectric effect to harvest changes in temperature and simultaneously store that energy in an integrated PEC. We first demonstrate the working principle of the PEC using a porous electroactive PVDF-barium titanate (BaTiO<sub>3</sub>) composite film as a separator. Under a temporal temperature change, the generated electric field in the pyroelectric separator induces migration of ions through the porous separator. The positive and negative ions migrate in opposite directions. The ionic movement causes electrostatic charge separation on the two opposite electrodes balancing the generated electric potential on the separator. The positive and negative ions are inserted into the electrochemical double layer in the supercapacitor cell electrodes, thus charging the cell. Figure 1.2 illustrates the migration of electrolyte ions under the influence of generated electric fields towards the electrodes. The PEC converts thermal energy to electrochemical energy and simultaneously stores the energy in the cell. Moreover, all

pyroelectric energy harvesters reported have used an external reservoir (i.e. capacitor or battery) for charge storage. The pyroelectric energy harvester is coupled to the battery or supercapacitor through some signal conditioning circuits. These external circuits also cause some harvested energy loss. In the integrated self-charging cell proposed here, the thermal energy is directly converted and stored in the electrochemical cell. Therefore, there is no external circuit with its associated losses to condition the converted electrical energy for electrochemical storage. This dissertation represents the first exploration of the integrated self-charging pyroelectrochemical cell for direct thermal energy conversion to stored electrochemical energy.

# 1.4 Thermal Effects in Electrochemical Cells

Low grade waste heat is a potential source of energy to produce electrical energy. Existing thermal energy harvesting systems utilize spatial thermal gradients. Thermoelectric devices convert a spatial thermal gradient to a potential difference due to the Seebeck effect. In solid state thermoelectric devices, under the thermal gradient electron-hole pairs are generated in the p and n type semiconductor materials between the hot and the cold electrodes and thus the diffusion of electron and holes in opposite direction generates a voltage across the device. The generated voltage is dependent on high electrical conductivity, the Seebeck coefficient, and low thermal conductivity. The generated voltage is in the range of  $\mu V K^{-1}$  due to significant tradeoff between these parameters, which limits the application of these devices at small temperature differences around ambient temperature [41], [42],[43].

In thermo-electrochemical cells, or thermocells, ideally continuous electrical

generation is possible with highly concentrated electrolytes containing a redox couple. In the presence of a thermal gradient across the same type electrodes, redox reactions happen due to their temperature difference. But these cells also suffer low conversion efficiencies (<1% relative to Carnot efficiency) [44], [45]. The efficiency of thermocells depends on high mass transport, low thermal conductivity, and high ionic conductivity of the electrolyte. Aqueous electrolytes have high diffusion of ions but are limited to <100 °C due to their low boiling point [46], [47]. On the other hand, non- aqueous ionic liquids are stable up to 130 °C but have low mass transfer capability due to increased viscosity [48], [49]. The highest reported power for thermocells is with aqueous electrolytes. The maximum open circuit voltage generated by a conventional thermocell is 1.3 mV at the temperature gradient of 12 K [44].

Another liquid based thermal energy harvesting technique is thermally regenerative electrochemical cycles (TREC). The cell is charged at a higher temperature ( $T_H$ ) and discharged at a lower temperature ( $T_L$ ). The voltage at charging is lower than the voltage at discharging and the voltage difference leads to the net energy production [50]–[52]. These cells have higher efficiency than other thermoelectric cells (maximum efficiency is 5.7% at  $T_H$ = 60 °C and  $T_L$ = 10 °C) [51], [53]. TRECs typically require high-cost anion exchange membranes and external electrical power for charging. Moreover, these cells still need work on their durability and electrode reversibility for large scale energy harvesting [53].

Under transient temperature change, the double layer of charge on the electrodes responds much faster than the charge-transfer adsorption process on the electrodes [54]. That is reflected in the open circuit potential of the cell measured. The differential

capacitance of the double layer is defined as the derivative of surface charge density with potential drop [55]. Ming Chen et al. reported a temperature dependent differential capacitance due to changing surface charge density across the double layer [56]. According to the law of conservation of charge [55], the potential of the electrode should increase to balance the changed surface density [57]. However, the adsorption of charge with longer temperature application causes the equilibrium potential to decrease following the Nernst equation. In an integrated pyroelectrochemical cell, this transient temperature effect is crucial. High diffusion rate or ionic conductivity of the electrolyte is desired along with high thermal conductivity of the electrolyte. Unlike thermoelectric cells, the efficiency of PEC cell is not dependent on the tradeoff between these two properties. However, it is important to understand the transient thermal effect on electrochemical cells to understand the PEC working mechanism and differentiate pyroelectric effect from themral effect.

Previous studies indicate the operating temperature range for aforementioned energy harvesting systems are 10-130°C. Pyroelectric materials operating temperature depends on their Curie temperature. PVDF and BaTiO<sub>3</sub> have a Curie temperature of 195 °C and 120 °C respectively [58], [59]. The operating temperature range for a thermal energy harvesting electrochemical cell is also largely dependent on the constituent materials in the electrochemical cell. The restricted temperature range for typical LiBs are -20 to 60 °C [60]. Beyond operating temperature range, LiBs suffer from non-ideal Faradaic reactions that contributes to irreverisble damage to the cell resulting in reduced cell capacity, failure and often risks explosions. Feng Leng et al. studied the effect of temperature on the components of an electrochemical cell at different temperatures using an electrochemistry-based electrical model [61]. They observed increased initial capacitance and diffusivity of

ions at increased temperature. The resistance of the cell or the electrode- electrolyte interface decreases with increased temperature due to increased charge transfer rate between the electrode and electrolyte. They also predicted thermal runaway beyond 90 °C as observed in previous studies on the LiBs. Researchers have been working towards finding alternative electrode and electrolyte materials for higher temperature operations. Mazharul Haque et al. reported two ionic liquids with activated carbon electrodes stable at temperatures up to 200 °C [62]. Lithium iron phosphate (LiFePO<sub>4</sub>) has been widely accepted for high temperature LiBs positive electrode material [63], [64]. Thermally reactive LiPF<sub>6</sub> can be replaced with alternative lithium salt chemistries which are stable at high temperatures as electrolytes [65], [66]. In conclusion, the selected electrolyte and electrode materials along with the pyroelectric separator decide the operating temperature range. When designing a PEC, it is important to consider the ambient temperature range to select the electrolyte and electrode optimal for the operating conditions.

# 1.5 Research Objectives

The primary objective of this research is to demonstrate and characterize the concept of an integrated PEC and open the possibility of a new energy harvesting pathway for a self-sustaining wireless system. This objective comprises three major aims: i) to explore methods of achieving enhanced electroactive response from the pyroelectric separator, ii) to understand how different pore structures impact the electroactive and mechanical properties of the pyroelectric separator, and iii) to understand the charge-discharge mechanism of the PEC, including distinguishing thermal vs. pyroelectric effects occurring in the cell. We have used a PVDF separator for its simple fabrication process,

mechanical flexibility, and electroactive properties. Typical electrochemical separators have a Young's modulus of 200-400 MPa [67], [68], which is enough to sustain mechanical stress during cell construction, and ~40% [69] porosity to ensure proper channels for ion migration. However, with 40% porosity, we risk a substantially lower figure of merit for the pyroelectric PVDF separator, thus reducing the energy density and efficiency of the self-charging cell. We have taken different measures to balance the impact of high porosity in the electrochemical separator. Both mechanical stretching and the addition of fillers in the PVDF films have independently been shown to improve the electroactive phase content in PVDF film. However, until now, there has been no investigation of the combined effects of these methods—i.e., the efficacy of stretching composite PVDF films to increase PVDF polar phases. In this study, we have stretched composite films uniaxially to understand the effects of the ceramic particles in combination with mechanical stretching on electroactive performance of PVDF films.

Replacing a commercial electrochemical separator with a pyroelectric thin film requires maintaining good ionic conductivity while preserving the integrity of the electroactive thin film. Phase inversion is a well-studied method to create controlled pores in polymer thin films [70]. To date, phase inversion has not been applied to ceramic-polymer composite piezoelectric thin films, and questions remain as to the effect of this method on the porous structure and resulting piezo-activity of the composite. For the first time, this work investigates the effects of pore structure on the piezoelectric activity and mechanical properties of PVDF- BaTiO<sub>3</sub> composite films. These results can guide future designs of highly porous ceramic-polymer piezoelectric materials synthesized by phase inversion.

Conventional electrochemical cell designs (including coin cells and beaker cells) are not set-up to enable rapid heating or cooling of the cell separator, as required for PEC testing. To test the PEC, we have made two electrochemical designs based on two different heating mechanisms (convection and conduction). These cell designs enable us to understand the charging-discharging mechanism and ion migration pattern due to changing polarization of the separator in the PEC. Additionally, the cell designs enable future testing of the PEC cell in-operando via spectroelectrochemistry (SEC). SEC enables ultravioletvisible (UV-Vis) spectroscopic study of electrochemical cells to explore the evolution of different cell components and understand cell mechanisms. Researchers have demonstrated different modified cells to accommodate SEC, however existing designs do not permit easy temperature ramp techniques to examine high-temperature conditions or rapid temperature fluctuations as required for PEC testing. Beyond the current work, in-operando SEC measurements are also of considerable value in the study of lithium-ion batteries (LIBs). As researchers explore alternative electrolytes and electrodes for high-temperature rechargeable batteries, SEC can be leveraged to investigate and characterize the components of the high-temperature LIBs. Easy-to-replicate cell designs that support hightemperature LIB SEC research are needed for the continued advancement of this field. To demonstrate the working mechanism and ease optimization of the PEC, we designed heated SEC cells that are easy to make and have potential for different applications like high temperature LIB research.

Lastly, the demonstration of a working PEC involves electrochemical characterization. Although there have been studies at elevated temperatures on electrochemical cell performance [71], temporal temperature change and how it affects the

electrode-electrolyte interface is yet to be explored. In our study, the cells are subjected to thermal excitation over time. Thermal fluctuations are the charging mechanism for this novel device. It is critical to understand the difference between thermal and pyroelectric effects for such transient changes. Additionally, the use of a ceramic-polymer thin film as an electrochemical cell poses some questions on the electrochemical performance of the cell (i.e., series resistance, leakage current). This work will address the fundamental mechanism of ion transportation in the PEC which has not been explored in previous works on self-charging cells. Moreover, the functionality of a PEC in terms of generated energy per cycle and energy conversion efficiency are key parameters for demonstrating its viability in practice. Full thermo-electrochemical characterization of the cell enables understanding of the limitations of the device technology and the directions for device optimization.

# 1.6 Dissertation Overview

The dissertation is divided into five chapters. The first chapter underlines the motivation and scope of this research. In Chapter 2 we have incorporated ceramic particles in pure PVDF films, and studied the efficacy of stretching the composite film to enhance its pyroelectric performance.

Chapter 3 details our findings on how different morphology impacts the electroactive performance of our films. The effect of pore structure on the mechanical properties and the piezoelectric voltage response of the composite films is examined along with the mechanical limitation that the structure imposes on the films.

In Chapter 4, we have detailed two easy-to-fabricate SEC cell designs to

demonstrate the PEC prototype. The chapter includes the fabrication details with information on the components used. The chapter also discussed the unique capabilities of the cells.

Chapter 5 describes the construction process and electrochemical characterization of the cell. The electrochemical stability and charging-discharging of the cell under temporal temperature change are studied in different configurations. Repeated tests on the cells with and without a pyroelectric separator distinguish between the thermal effect and the pyroelectric effect on the charge state of an electrochemical cell. Finally, we characterize the energy harvesting performance and efficiency of a working pyroelectrochemical cell. Chapter 6 summarizes the key findings of the research.

## 1.7 References

- [1] EnOcean Alliance, "EnOcean The world of energy harvesting wireless technology," EnOcean, Sandy, UT, USA, White Paper, Feb 2016, [Online]. Available: https://www.enocean.com/wp-content/uploads/redaktion/pdf/white paper/WhitePaper Getting Started With EnOcean v4.0.pdf.
- [2] S. Roundy, "Energy harvesting for tire pressure monitoring systems: Design considerations," *Proc. PowerMEMS*, Nov. 9-12, 2008. https://iss.mech.utah.edu/wp-content/uploads/sites/103/2012/10/001-6-Roundy-S.pdf (accessed Nov. 07, 2021).
- [3] D. Klan, K. Hose, and K. U. Sattler, "Developing and deploying sensor network applications with AnduIN," *ACM Int. Conf. Proc. Ser.*, Aug. 2009, pp. 35–40, doi: 10.1145/1594187.1594202/FORMAT/PDF.
- [4] W. Trappe, R. Howard, and R. S. Moore, "Low-energy security: Limits and opportunities in the internet of things," *IEEE Secur. Priv.*, vol. 13, no. 1, pp. 14–21, Feb. 2015, doi: 10.1109/MSP.2015.7.
- [5] S. Li, J. Breiholz, S. Kamineni, J. Im, D. D. Wentzloff, and B. H. Calhoun, "An 85 nW IoT node-controlling SoC for MELs power-mode management and phantom energy reduction," *2020 IEEE Int. Symp. Circuits Syst. (ISCAS)*, Oct. 12-14, 2020, pp. 1-5, doi: 10.1109/ISCAS45731.2020.9180473.
- [6] J. M. Rabaey, M. J. Ammer, J. L. Da Silva, D. Patel, and S. Roundy, "PicoRadio supports ad hoc ultra-low power wireless networking," *Computer*, vol. 33, no. 7, pp. 42–48, Jul. 2000, doi: 10.1109/2.869369.
- [7] D. D. Wentzloff and A. Alghaihab, "Ultralow-power receivers: Overcoming battery limitations to facilitate self-powered operation," *IEEE Solid-State Circuits Mag.*, vol. 13, no. 3, pp. 33–37, Aug. 2021, doi: 10.1109/MSSC.2021.3088967.
- [8] C. R. Bowen, J. Taylor, E. Leboulbar, D. Zabek, A. Chauhan, and R. Vaish, "Pyroelectric materials and devices for energy harvesting applications," *Energy Environ. Sci.*, vol. 7, no. 12, pp. 3836–3856, Dec. 2014, doi: 10.1039/C4EE01759E.
- [9] S. Arbogast, "International standard atmosphere: How it affects flight Understanding the basics," Universal Weather and Aviation Inc. https://www.universalweather.com/blog/international-standard-atmosphere-how-it-affects-flight-understanding-the-basics/ (accessed Nov. 07, 2021).
- [10] J. Fang, H. Frederich, and L. Pilon, "Harvesting nanoscale thermal radiation using pyroelectric materials," *J. Heat Transfer*, vol. 132, no. 9, pp. 1–10, Sep. 2010, doi: 10.1115/1.4001634.
- [11] H. Xue *et al.*, "A wearable pyroelectric nanogenerator and self-powered breathing sensor," *Nano Energy*, vol. 38, pp. 147–154, Aug. 2017, doi:

- 10.1016/J.NANOEN.2017.05.056.
- [12] J. Tao and J. Hu, "Energy harvesting from pavement via polyvinylidene fluoride: Hybrid piezo-pyroelectric effects," *J. Zhejiang Univ. Sci. A*, vol. 17, no. 7, pp. 502–511, Jul. 2016, doi: 10.1631/JZUS.A1600166.
- [13] H. Li *et al.*, "A wearable solar-thermal-pyroelectric harvester: Achieving high power output using modified rGO-PEI and polarized PVDF," *Nano Energy*, vol. 73, p. 104723, Jul. 2020, doi: 10.1016/J.NANOEN.2020.104723.
- [14] S. Dalola, V. Ferrari, and D. Marioli, "Pyroelectric effect in PZT thick films for thermal energy harvesting in low-power sensors," *Procedia Eng.*, vol. 5, pp. 685–688, Sep. 2010, doi: 10.1016/j.proeng.2010.09.202.
- [15] D. Damjanovic, "Ferroelectric, dielectric and piezoelectric properties of ferroelectric thin films and ceramics," *Rep. Prog. Phys*, vol. 61, no. 9, pp. 1267–1324, Sep. 1998.
- [16] Q. Wang *et al.*, "Improved heat transfer for pyroelectric energy harvesting applications using a thermal conductive network of aluminum nitride in PMN–PMS–PZT ceramics," *J. Mater. Chem. A*, vol. 6, no. 12, pp. 5040–5051, Mar. 2018, doi: 10.1039/C8TA00235E.
- [17] C. C. Hsiao, A. S. Siao, and J. C. Ciou, "Improvement of pyroelectric cells for thermal energy harvesting," *Sensors*, vol. 12, no. 1, pp. 534–548, Jan. 2012, doi: 10.3390/S120100534.
- [18] C. C. Hsiao, and A. S. Siao. "Improving pyroelectric energy harvesting using a sandblast etching technique." *Sensors (Basel)*, vol. 13, no. 9, pp.12113-12131, Sep. 2013, doi:10.3390/s130912113
- [19] D. Zabek, K. Seunarine, C. Spacie, and C. Bowen, "Graphene ink laminate structures on poly(vinylidene difluoride) (PVDF) for pyroelectric thermal energy harvesting and waste heat recovery," *ACS Appl. Mater. Interfaces*, vol. 9, no. 10, pp. 9161–9167, Mar. 2017, doi: 10.1021/ACSAMI.6B16477/SUPPL\_FILE/AM6B16477 SI 001.PDF.
- [20] H. Nguyen, A. Navid, and L. Pilon, "Pyroelectric energy converter using co-polymer P(VDF-TrFE) and Olsen cycle for waste heat energy harvesting," *Appl. Therm. Eng.*, vol. 30, no. 14–15, pp. 2127–2137, Oct. 2010, doi: 10.1016/J.APPLTHERMALENG.2010.05.022.
- [21] S. Sukumaran, S. Chatbouri, D. Rouxel, E. Tisserand, F. Thiebaud, and T. Ben Zineb, "Recent advances in flexible PVDF based piezoelectric polymer devices for energy harvesting applications," *J. Intell. Mater. Syst. Struct.*, vol. 32, no. 7, pp. 746–780, Oct. 2020, doi: 10.1177/1045389X20966058.
- [22] Y. Yang et al., "Flexible pyroelectric nanogenerators using a composite structure of

- lead-free KNbO<sub>3</sub> nanowires," *Adv. Mater.*, vol. 24, no. 39, pp. 5357–5362, Oct. 2012, doi: 10.1002/ADMA.201201414.
- [23] A. Lund, C. Gustafsson, H. Bertilsson, and R. W. Rychwalski, "Enhancement of β phase crystals formation with the use of nanofillers in PVDF films and fibres," *Compos. Sci. Technol.*, vol. 71, no. 2, pp. 222–229, Jan. 2011, doi: 10.1016/j.compscitech.2010.11.014.
- [24] M. Abbasipour, R. Khajavi, A. A. Yousefi, M. E. Yazdanshenas, F. Razaghian, and A. Akbarzadeh, "Improving piezoelectric and pyroelectric properties of electrospun PVDF nanofibers using nanofillers for energy harvesting application," *Polym. Adv. Technol.*, vol. 30, no. 2, pp. 279–291, Feb. 2019, doi: 10.1002/PAT.4463.
- [25] J. D. Zook and S. T. Liu, "Pyroelectric effects in thin film," J. Appl. Phys., vol. 49, no. 8, pp. 4604–4606, Aug. 1978, doi: 10.1063/1.325442.
- [26] X. Chen, J. Shao, X. Li, and H. Tian, "A flexible piezoelectric-pyroelectric hybrid nanogenerator based on P(VDF-TrFE) nanowire array," *IEEE Trans. Nanotechnol.*, vol. 15, no. 2, pp. 295–302, Mar. 2016, doi: 10.1109/TNANO.2016.2522187.
- [27] A. Ferri *et al.*, "Probing the local piezoelectric behavior in stretched barium titanate/poly(vinylidene fluoride) nanocomposites," *Compos. Sci. Technol.*, vol. 186, p. 107914, Jan. 2020, doi: 10.1016/j.compscitech.2019.107914.
- [28] R. Gregorio, M. Cestari, and F. E. Bernardino, "Dielectric behaviour of thin films of β-PVDF/PZT and β-PVDF/BaTiO<sub>3</sub> composites," *J. Mater. Sci.*, vol. 31, no. 11, pp. 2925–2930, Jun. 1996, doi: 10.1007/BF00356003.
- [29] D. Lingam, A. R. Parikh, J. Huang, A. Jain, and M. Minary-Jolandan, "Nano/microscale pyroelectric energy harvesting: Challenges and opportunities," *Int. J. Smart Nano. Mater.*, vol. 4, no. 4, pp. 229–245, Dec. 2014, doi: 10.1080/19475411.2013.872207.
- [30] L. Li, M. Zhang, M. Rong, and W. Ruan, "Studies on the transformation process of PVDF from α to β phase by stretching," *RSC Adv.*, vol. 4, no. 8, pp. 3938–3943, Dec. 2013, doi: 10.1039/c3ra45134h.
- [31] R. Gregorio and E. M. Ueno, "Effect of crystalline phase, orientation and temperature on the dielectric properties of poly (vinylidene fluoride) (PVDF)," *J. Mater. Sci.*, vol. 34, no. 18, pp. 4489–4500, Sep. 1999, doi: 10.1023/A:1004689205706.
- [32] Y. Zi *et al.*, "Effective energy storage from a triboelectric nanogenerator," *Nat. Commun.*, vol. 7, no. 1, pp. 1–8, Mar. 2016, doi: 10.1038/ncomms10987.
- [33] H. Sun, Y. Zhang, J. Zhang, X. Sun, and H. Peng, "Energy harvesting and storage in 1D devices," *Nat. Rev. Mater.*, vol. 2, no. 6, pp. 1–12, Apr. 2017, doi: 10.1038/natreymats.2017.23.

- [34] S. Wang *et al.*, "Motion charged battery as sustainable flexible-power-unit," *ACS Nano*, vol. 7, no. 12, pp. 11263–11271, Dec. 2013, doi: 10.1021/NN4050408/SUPPL FILE/NN4050408 SI 001.PDF.
- [35] B. D. Boruah, B. Wen, and M. De Volder, "Light rechargeable lithium-ion batteries using V<sub>2</sub>O<sub>5</sub> cathodes," *Nano Lett.*, vol. 21, no. 8, pp. 3527–3532, Apr. 2021, doi: 10.1021/ACS.NANOLETT.1C00298/SUPPL FILE/NL1C00298 SI 001.PDF.
- [36] S. F. Hoefler *et al.*, "New solar cell-battery hybrid energy system: Integrating organic photovoltaics with Li-ion and Na-ion technologies," *ACS Sustain. Chem. Eng.*, vol. 8, no. 51, pp. 19155–19168, Dec. 2020, doi: 10.1021/ACSSUSCHEMENG.0C07984/SUPPL\_FILE/SC0C07984\_SI\_001.PDF.
- [37] L. Liu and S. Choi, "A self-charging cyanobacterial supercapacitor," *Biosens. Bioelectron.*, vol. 140, pp. 111354, May 2019, doi: 10.1016/j.bios.2019.111354.
- [38] D. Pankratov, Z. Blum, D. B. Suyatin, V. O. Popov, and S. Shleev, "Self-charging electrochemical biocapacitor," *ChemElectroChem*, vol. 1, no. 2, pp. 343–346, Feb. 2014, doi: 10.1002/CELC.201300142.
- [39] X. Xue, S. Wang, W. Guo, Y. Zhang, and Z. L. Wang, "Hybridizing energy conversion and storage in a mechanical-to-electrochemical process for self-charging power cell," *Nano Lett.*, vol. 12, no. 9, pp. 5048–5054, Sep. 2012, doi: 10.1021/NL302879T/SUPPL FILE/NL302879T SI 001.PDF.
- [40] A. Ramadoss, B. Saravanakumar, S. W. Lee, Y. S. Kim, S. J. Kim, and Z. L. Wang, "Piezoelectric-driven self-charging supercapacitor power cell," *ACS Nano*, vol. 9, no. 4, Mar. 2015, doi: 10.1021/acsnano.5b00759.
- [41] G. J. Snyder and E. S. Toberer, "Complex thermoelectric materials," *Nat. Mater.* 2008, vol. 7, no. 2, pp. 105–114, Feb. 2008, doi: 10.1038/nmat2090.
- [42] T. C. Harman, M. P. Walsh, B. E. Laforge, and G. W. Turner, "Nanostructured thermoelectric materials," *J. Electron. Mater.*, vol. 34, no. 5, pp. L19–L22, May 2005, doi: 10.1007/S11664-005-0083-8.
- [43] A. R. M. Siddique, S. Mahmud, and B. Van Heyst, "A review of the state of the science on wearable thermoelectric power generators (TEGs) and their existing challenges," *Renew. Sustain. Energy Rev.*, vol. 73, pp. 730–744, Jun. 2017, doi: 10.1016/J.RSER.2017.01.177.
- [44] M. F. Dupont, D. R. MacFarlane, and J. M. Pringle, "Thermo-electrochemical cells for waste heat harvesting progress and perspectives," *Chem. Commun.*, vol. 53, no. 47, pp. 6288–6302, Jun. 2017, doi: 10.1039/C7CC02160G.
- [45] M. S. Romano, J. M. Razal, D. Antiohos, G. Wallace, and J. Chen, "Nano-carbon electrodes for thermal energy harvesting," *J. Nanosci. Nanotechnol.*, vol. 15, no. 1, pp. 1–14, Jan. 2015, doi: 10.1166/JNN.2015.9731.

- [46] H. Im *et al.*, "High-efficiency electrochemical thermal energy harvester using carbon nanotube aerogel sheet electrodes," *Nat. Commun.*, vol. 7, pp. 10600, Feb. 2016, doi: 10.1038/NCOMMS10600.
- [47] R. Hu *et al.*, "Harvesting waste thermal energy using a carbon-nanotube-based thermo-electrochemical cell," *Nano Lett.*, vol. 10, no. 3, pp. 838–846, Mar. 2010, doi: 10.1021/NL903267N/SUPPL FILE/NL903267N SI 001.PDF.
- [48] D. R. Macfarlane *et al.*, "Energy applications of ionic liquids," *Energy Environ. Sci.*, vol. 7, no. 1, pp. 232–250, Dec. 2013, doi: 10.1039/C3EE42099J.
- [49] D. R. MacFarlane *et al.*, "Ionic liquids and their solid-state analogues as materials for energy generation and storage," *Nat. Rev. Mater.*, vol. 1, no. 2, pp. 1–15, Jan. 2016, doi: 10.1038/natrevmats.2015.5.
- [50] Y. Yang *et al.*, "Membrane-free battery for harvesting low-grade thermal energy," *Nano Lett.*, vol. 14, no. 11, pp. 6578–6583, Nov. 2014, doi: 10.1021/NL5032106/SUPPL FILE/NL5032106 SI 001.PDF.
- [51] S. W. Lee *et al.*, "An electrochemical system for efficiently harvesting low-grade heat energy," *Nat. Commun.*, vol. 5, no. 1, pp. 1–6, May 2014, doi: 10.1038/ncomms4942.
- [52] Y. Yang *et al.*, "Charging-free electrochemical system for harvesting low-grade thermal energy," *Proc. Natl. Acad. Sci. U.S.A.*, vol. 111, no. 48, pp. 17011–17016, Dec. 2014, doi: 10.1073/PNAS.1415097111/-/DCSUPPLEMENTAL.
- [53] M. Rahimi *et al.*, "Emerging electrochemical and membrane-based systems to convert low-grade heat to electricity," *Energy Environ. Sci.*, vol. 11, no. 2, pp. 276–285, Feb. 2018, doi: 10.1039/C7EE03026F.
- [54] N. Garcia-Araez, V. Climent, and J. Feliu, "Separation of temperature effects on double-layer and charge-transfer processes for platinum|solution interphases. Entropy of formation of the double layer and absolute molar entropy of adsorbed hydrogen and OH on Pt(111)," *J. Phys. Chem. C*, vol. 113, no. 46, pp. 19913–19925, Oct. 2009, doi: 10.1021/JP904638D.
- [55] M. V. Fedorov and A. A. Kornyshev, "Ionic liquids at electrified interfaces," *Chem. Rev.*, vol. 114, no. 5, pp. 2978–3036, Mar. 2014, doi: 10.1021/CR400374X.
- [56] M. Chen, Z. A. H. Goodwin, G. Feng, and A. A. Kornyshev, "On the temperature dependence of the double layer capacitance of ionic liquids," *J. Electroanal. Chem.*, vol. 819, pp. 347–358, Jun. 2018, doi: 10.1016/J.JELECHEM.2017.11.005.
- [57] H. Lim, Y. Shi, M. Wang, and Y. Qiao, "Effects of work function on thermal sensitivity of electrode potential," *Appl. Phys. Lett.*, vol. 106, no. 22, p. 223901, Jun. 2015, doi: 10.1063/1.4921769.

- [58] D. Mao, B. E. Gnade, and M. A. Quevedo-Lopez, "Ferroelectric properties and polarization switching kinetic of poly (vinylidene fluoride-trifluoroethylene) copolymer," in *Ferroelectrics Physical Effects*, M. Lallert, Ed., London, United Kingdom: IntechOpen, 2011, doi: 10.5772/17147.
- [59] K. I. Sakayori *et al.*, "Curie temperature of BaTiO<sub>3</sub>," *Jpn. J. Appl. Phys.*, vol. 34, no. 9, pp. 5443–5445, Sep. 1995, doi: 10.1143/JJAP.34.5443/XML.
- [60] Y. Ji, Y. Zhang, and C. Y. Wang, "Li-ion cell operation at low temperatures," *J. Electrochem. Soc.*, vol. 160, no. 4, pp. A636–A649, Feb. 2013, doi: 10.1149/2.047304JES/XML.
- [61] F. Leng, M. Tan, M. Pecht, and J. Zhang, "The effect of temperature on the electrochemistry in lithium-ion batteries." 2014 Int. Symp. Next-Gen. Electron. (ISNE), May 7-10, 2014, pp. 1-4, doi: 10.1109/ISNE.2014.6839339
- [62] M. Haque, Q. Li, V. Kuzmenko, A. D. Smith, and P. Enoksson, "Ionic liquid electrolyte for supercapacitor with high temperature compatibility," *J. Phys. Conf. Ser.*, vol. 922, no. 1, pp. 012011 Aug. 2017, doi: 10.1088/1742-6596/922/1/012011.
- [63] X. Chen *et al.*, "Mixed salts of LiTFSI and LiBOB for stable LiFePO<sub>4</sub>-based batteries at elevated temperatures," *J. Mater. Chem. A*, vol. 2, no. 7, pp. 2346–2352, Jan. 2014, doi: 10.1039/C3TA13043F.
- [64] J. Zhang *et al.*, "Sustainable, heat-resistant and flame-retardant cellulose-based composite separator for high-performance lithium ion battery," *Sci. Rep.*, vol. 4, no. 1, pp. 1–8, Feb. 2014, doi: 10.1038/srep03935.
- [65] Z. Zhang *et al.*, "LiPF<sub>6</sub> and lithium oxalyldifluoroborate blend salts electrolyte for LiFePO<sub>4</sub>/artificial graphite lithium-ion cells," *J. Power Sources*, Nov. 2010, doi: 10.1016/j.jpowsour.2010.05.056.
- [66] K. Xu, S. S. Zhang, U. Lee, J. L. Allen, and T. R. Jow, "LiBOB: Is it an alternative salt for lithium ion chemistry?" *J. Power Sources*, vol. 146, no. 1–2, pp. 79–85, Aug. 2005, doi: 10.1016/J.JPOWSOUR.2005.03.153.
- [67] N. Liang, J. Fang, and X. Guo, "A simple approach for preparation of porous polybenzimidazole membranes as a promising separator for lithium ion batteries," *J. Mater. Chem. A*, vol. 5, no. 29, pp. 15087–15095, Jul. 2017, doi: 10.1039/C7TA03554C.
- [68] G. Y. Gor, J. Cannarella, J. H. Prévost, and C. B. Arnold, "A model for the behavior of battery separators in compression at different strain/charge rates," *J. Electrochem. Soc.*, vol. 161, no. 11, pp. F3065–F3071, Sep. 2014, doi: 10.1149/2.0111411JES/XML.
- [69] D. R. Rajagopalan Kannan, P. K. Terala, P. L. Moss, and M. H. Weatherspoon, "Analysis of the separator thickness and porosity on the performance of lithium-ion

- batteries," *Int. J. Electrochem.*, vol. 2018, pp. 1–7, Jul. 2018, doi: 10.1155/2018/1925708.
- [70] M. Mulder, "Phase inversion membranes," in *Encyclopedia of Separation Science*, I. D. Wilson, Ed. Cambridge, MA, USA: Academic Press, pp. 3331–3346, Jan. 2000, doi: 10.1016/B0-12-226770-2/05271-6.
- [71] C. E. L. Foss, A. M. Svensson, Ø. Gullbrekken, S. Sunde, and F. Vullum-Bruer, "Temperature effects on performance of graphite anodes in carbonate based electrolytes for lithium ion batteries," *J. Energy Storage*, vol. 17, pp. 395–402, Jun. 2018, doi: 10.1016/J.EST.2018.04.001.

Material	Pyroelectric coefficient (μCm <sup>-2</sup> K <sup>-1</sup> )
PVDF film	27-33
P(VDF-TrFE) film	43.9
ZnO	12–15
KNbO <sub>3</sub>	8
PZT	800
AlN	6–8
CdS	4
CdSe	3.5
BaTiO <sub>3</sub>	225–259

Table 1.1: Pyroelectric coefficient of some common materials.

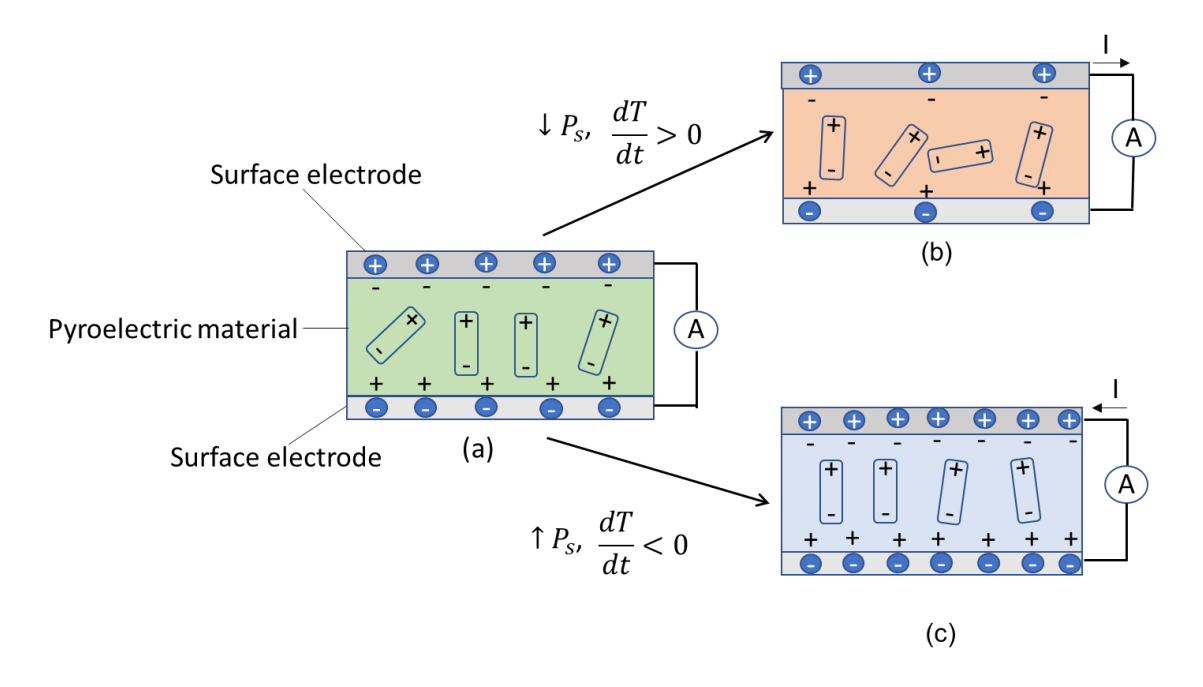


Figure 1.1: Pyroelectric material (a) in thermal equilibrium connected to external circuit through surface electrodes Charges appear on the electrodes screening the spontaneous polarization of the material. (b) Spontaneous polarization decreases under a positive temperature ramp (dT/dt > 0) and thus surface charges flow through external circuit to attain charge neutrality again. (c) With a negative temperature ramp (dT/dt < 0), the increased polarization results in a current in the opposite direction through the external circuit.

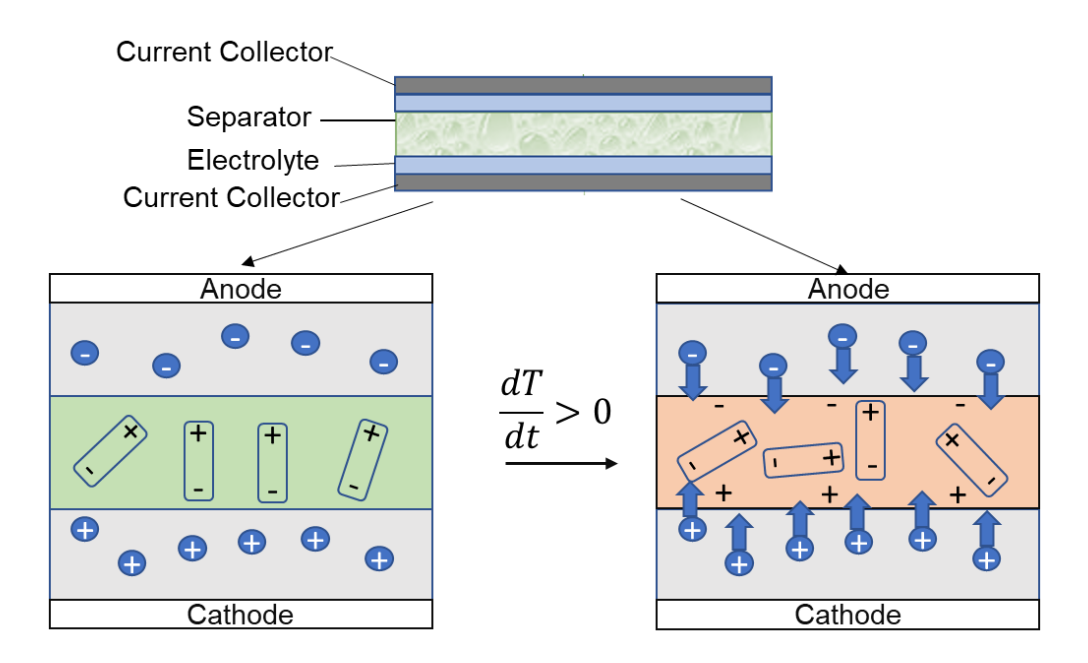


Figure 1.2: The electrochemical cell separator replaced by a pyroelectric film charging under the influence of a positive temperature ramp. An electric field generates across the pyroelectric film due to decreasing polarization which drives ion migration in the cell.

# **CHAPTER 2**

# STRETCHING-INDUCED PHASE TRANSITIONS IN PVDF-BATIO<sub>3</sub> FLEXIBLE COMPOSITE PIEZOELECTRIC FILMS

This work examines the combined effect of stretching and BaTiO<sub>3</sub> addition on phase transformations in PVDF-BaTiO<sub>3</sub> composite films for the first time. The results indicate that an alternative phase transformation mechanism occurs during the stretching of PVDF composite films.

This article was published in *Scripta Materialia*, Volume 193, 2021, Fariha Khan, Tim Kowalchik, Shad Roundy, Roseanne Warren, "Stretching-induced phase transitions in barium titanate-poly(vinylidene fluoride) flexible composite piezoelectric films," pp. 64-70. Copyright Elsevier.

## 2.1 Introduction

Poly(vinylidene fluoride) (PVDF) is a semi-crystalline, polymorph, ferroelectric polymer. Since its discovery as a piezoelectric material in 1961 [17], it has gained popularity due to its mechanical flexibility, good dielectric properties, electroactive response, and simple fabrication. While these properties make PVDF a promising material for sensors, actuators, and energy harvesting devices, its low piezoelectric and pyroelectric coefficients compared to pure ceramics limit the use of PVDF in certain applications. Several approaches (e.g., mechanical drawing [18], [19], introducing ceramic fillers [20], [21], poling at a high electric field [22]) have been tested to enhance PVDF's properties and expand the material's range of application. One promising—but to-date largely untested—approach to increase PVDF β phase content could be a combination of mechanical drawing and ceramic fillers to produce a PVDF-ceramic composite film with improved piezo/pyroelectric response. The goal of this work is to test the effects of varying ceramic filler loading and stretching ratios on the β phase content of PVDF- barium titanate (BaTiO<sub>3</sub>) thin films.

PVDF-BaTiO<sub>3</sub> is a widely studied ceramic-polymer ferroelectric composite that is simple to fabricate by a variety of methods [23], [24]. BaTiO<sub>3</sub> has been shown to increase the  $\beta$  phase content of PVDF polymer matrices when there is a large interaction surface between the polymer and the ceramic particles [18], [25]. According to current theory, BaTiO<sub>3</sub> particles play a crucial role in the nucleation of PVDF crystal phases and promote the formation of highly electroactive  $\beta$  phases in the polymer chain. The three common PVDF phases, which describe different polymer chain conformations, are  $\alpha$ ,  $\beta$ , and  $\gamma$  [26]. The non-polar  $\alpha$  phase is the most prevalent and can be easily formed in the polymer

matrix [17], [23], [27]. While both  $\beta$  and  $\gamma$  are polar phases, the  $\beta$  phase has a higher dipole moment than the  $\gamma$  phase and yields higher piezoelectric constants [26]. Moreover, BaTiO<sub>3</sub> particles help stabilize the  $\beta$  phase of PVDF by reducing the number of defects in the polymer chain [28] and limiting the conversion of the unstable  $\beta$  phase to the otherwise more temperature- and pressure-stable  $\alpha$  phase [20].

Previous research indicates that mechanical drawing of PVDF films can also effectively convert non-polar PVDF phases to the β phase[26], [29]. The predominant α phase can be converted to the β phase if the drawing temperature is below 100°C and stretching ratios are on the order of 2-5 [25]. Stretching influences the position of fluorine atoms in the PVDF chain, inducing polymer phase influences the position of fluorine atoms in the PVDF chain, inducing polymer phase transitions. While both mechanical stretching and the addition of BaTiO<sub>3</sub> particles in the PVDF films have independently been shown to improve the \beta phase content, until now there has been no such investigation of the combined effects of these methods—i.e., the efficacy of stretching PVDF-BaTiO<sub>3</sub> films as a means to increase PVDF polar phases. In this study, PVDF-BaTiO<sub>3</sub> thin films of 0, 5, and 10 wt% BaTiO<sub>3</sub> undergo uniaxial mechanical drawing at various stretching ratios until the point of breaking. The effects of the ceramic particles in combination with mechanical drawing are quantified through Fourier transform infrared spectroscopy (FT-IR) and X-ray diffraction (XRD) measurements at various stages of fabrication to determine the impact of process parameters on β phase content of PVDF-BaTiO<sub>3</sub> composite films.

#### 2.2 Methods

All materials were purchased from Millipore Sigma and used without modification. PVDF powder (average MW~534,000 g/mol) was dissolved in N, N-dimethylformamide (DMF) at 15 wt% (w/w) in a 45°C water bath. BaTiO₃ nanopowder (cubic crystalline phase, <100 nm particle size, ≥99% trace metals basis) was ground using a mortar and pestle for 5 minutes to deagglomerate the particles followed by sonication in DMF for 45 minutes. The homogeneous BaTiO₃ dispersion was added to the PVDF-DMF solution at room temperature and sonicated for 1 hour. PVDF-BaTiO₃ films were made by drop-casting the prepared slurry onto a glass plate using a doctor blade and Kapton tape to obtain uniform film thicknesses. The films were dried at 60°C in an oven to evaporate the DMF solvent and increase β phase content.

After annealing at 90°C for 5 hours, films were then uniaxially stretched by clamping and hanging weights on a custom-made stretching device. Each film was cut into a 12.7 mm by 38.1 mm sample, which was clamped on its ends between a fixed and a moveable plate, initially without tension. The stretching device and sample were placed into an oven at 80°C for 1 hour to reach thermal equilibrium. The film was then loaded by placing weights on the moveable end of the device and maintained for 15 minutes. The deformed film was removed from the oven and allowed to relax. Average elongation was calculated as the ratio of the stretched: unstretched length.

The above procedure was applied to PVDF films with 0, 5, and 10 wt% BaTiO<sub>3</sub> content and three different film thicknesses (50, 100, and 150 µm). Scanning electron microscopy (SEM) (FEI Quanta 600F) imaging was used to examine BaTiO<sub>3</sub> particle agglomeration and dispersion in the films. Elemental analysis of PVDF-BaTiO<sub>3</sub> films was

conducted using energy-dispersive X-ray spectroscopy (EDX) of carbon-coated films. FT-IR spectroscopy (Varian 3100 Excalibur) and XRD (D2 Phaser;  $10^{\circ}$ - $60^{\circ}$ ;  $0.0162^{\circ}$ /step sampling rate) were used to measure the  $\beta$  phase content of all films.

Figure 2.1a provides a conceptual illustration of the stretching-induced phase transition in PVDF-BaTiO<sub>3</sub> composite films. In PVDF, the α phase is characterized by an antiparallel TGTG' conformation of fluorine atoms (T indicating trans arrangement in which the fluorine atoms are oriented at  $\pm 180^{\circ}$  in the torsional bond arrangement, and G indicating gauche arrangement at  $\pm 60^{\circ}$ ). The  $\gamma$  phase is characterized by TTTGTTTG' conformation. In contrast, the β phase consists of a TTTT conformation. In pure PVDF films, stretching primarily causes conversion of  $\alpha$  phase to  $\beta$  phase, with the antiparallel TGTG' conformation converting to TTTT conformation and creating dipole moments perpendicular to the polymer chain [17], [19]. Figure 2.1b provides a SEM image of an unstretched 10 wt% PVDF-BaTiO<sub>3</sub> film. The BaTiO<sub>3</sub> particles are uniformly dispersed, and the film shows minor porosity resulting from the drop-casting method. A SEM image of the same sample, post-stretching (1.1x average elongation) (Figure 2.1c), shows lines on the films arising from the uniaxial stretching as wells as microtears along BaTiO<sub>3</sub> particles. EDX measurements of carbon-coated samples confirm the expected doubling of Ba and Ti atomic content for 5 and 10 wt% PVDF-BaTiO<sub>3</sub> films (Figure 2.1d).

## 2.3 Uniaxial Stretching of Composite Films

Figure 2.2 characterizes the force required to stretch the PVDF-BaTiO<sub>3</sub> films, and the resulting elongation. Data points in Figure 2.2 represent average values of two samples of each film; in all cases, the results differed by <10% between samples. In addition,

elongation values in Figure 2.2 represent average values for the full length of the stretched film; localized film stresses and stretching ratios likely vary across the films and may be higher in areas of the sample closer to the breaking line. This is especially true for 5 and 10 wt% BaTiO<sub>3</sub> films, which did not stretch as uniformly as pure PVDF.

The maximum load applied to the films at their breaking point is an important indication of our ability to mechanically stretch the composite films using a uniaxial stretching setup. The load at breaking increases with film thickness for all values of BaTiO<sub>3</sub> wt% (Figure 2.2a). Pure PVDF shows the highest increase in strength as thickness increases from 50 µm to 150 µm, compared to only a slight increase for the composite films. The observed tendency of PVDF-BaTiO<sub>3</sub> composite films to rip easily during stretching, even at higher thicknesses, is likely due to stress concentrations created by the introduction of BaTiO<sub>3</sub> particles. The introduction of filler particles creates micro-tears in the film during stretching, visible in Figure 2.1c; we suspect that subsequent large-scale tears propagating from these micro-tears are the primary failure mechanism for the composite films.

For all film thicknesses, increasing BaTiO<sub>3</sub> wt% results in decreasing achievable stretching ratios for composite films undergoing uniaxial stretching (Figure 2.2b). As expected, the pure PVDF film shows the most substantial elongation (1.5x for the 150 μm film). At 5 wt% BaTiO<sub>3</sub>, a stretching ratio approaching 1.5x is achieved with 150 μm film thickness; at 10 wt% BaTiO<sub>3</sub>, all films failed with less than 1.2x elongation. While pure PVDF films were observed to deform along their entire length during stretching easily, the composite films deformed in localized regions mid-length before sudden tearing. Variations in localized elongation, along with sample-to-sample differences, may account for the unexpected result observed for 10 wt% BaTiO<sub>3</sub>, where the 100 μm film produced

higher elongation than the 150 µm film. With the significant decrease in maximum elongation observed when BaTiO<sub>3</sub> content increases from 5 to 10 wt%, we conclude that BaTiO<sub>3</sub> content in PVDF-BaTiO<sub>3</sub> thin films should be limited to 5% if mechanical stretching is to be performed.

# 2.4 Analysis of Electroactive Phase Content

To evaluate and compare the changing  $\beta$  phase content of 0, 5, and 10 wt% BaTiO<sub>3</sub>-PVDF films, FTIR and XRD are used in conjunction. For FTIR spectra, the primary peak of  $\alpha$  phase is 763 cm<sup>-1</sup>, with additional  $\alpha$  phase peaks located at 408, 532, 795, 854, 975, and 1209 cm<sup>-1</sup> [23], [26], [29]–[31]. Unique  $\beta$  phase peaks are located at 445,464, 1276, and 1431 cm<sup>-1</sup>; unique  $\gamma$  phase peaks are located at 812 and 1234 cm<sup>-1</sup>. The peak at 840 cm<sup>-1</sup> is characteristic of both  $\beta$  and  $\gamma$  phases [24].

For pure PVDF (0 wt% BaTiO<sub>3</sub>, Figure 2.3a), the unannealed film is predominantly  $\alpha$  phase, missing significant peaks from both  $\beta$  and  $\gamma$  phases. There is a small increase in the  $\gamma$  peak at 812 cm<sup>-1</sup> with annealing, followed by increases in  $\beta$  phase peaks (and corresponding reductions in  $\alpha$  and  $\gamma$  phase peaks) with stretching. Specifically, the stretched PVDF film shows strong peaks at 445,464, 840, 1276, and 1431 cm<sup>-1</sup>. While the 840 cm<sup>-1</sup> peak is representative of both  $\beta$  and  $\gamma$ , the reduction in  $\gamma$  phase peak at 812 cm<sup>-1</sup> indicates the gains at 840 cm<sup>-1</sup> are likely predominantly  $\beta$  phase. This result is consistent with literature reports of pure PVDF film stretching [26], [32]–[34].

There is a considerable improvement in  $\beta$  phase content with the introduction of BaTiO<sub>3</sub> in PVDF, with unstretched 5 and 10 wt% PVDF- BaTiO<sub>3</sub> films (Figure 2.3b and c, respectively) showing higher  $\beta$  phase peaks (445, 464, 840, 1431 cm<sup>-1</sup>) compared to

pure, unstretched PVDF. The stretched PVDF- BaTiO<sub>3</sub> composite films show strong peaks at 445, 464, 840, 1276, and 1431 cm<sup>-1</sup>. Similar to the pure PVDF film, there is a noticeable decrease in γ phase peaks at 812 and 1234 cm<sup>-1</sup> with stretching, suggesting conversion of γ phase to β phase when PVDF- BaTiO<sub>3</sub> films are stretched. Note that as 0, 5, and 10 wt% BaTiO<sub>3</sub> films are stretched, decreasing film thickness results in an overall reduction in FTIR absorbance; therefore, quantitative comparisons of peak heights are needed to evaluate changes in phase content with film stretching more rigorously.

To quantitatively evaluate the electroactive  $(\beta+\gamma)$  phase fraction, we apply the equation proposed by Gregorio *et al.* [23] to the FTIR results of Figure 2.3:

$$F(\beta + \gamma) = \frac{A_{\beta + \gamma}}{A_{\beta + \gamma} + 1.26A_{\alpha}} \tag{2.1}$$

where  $A_{\alpha}$  and  $A_{\beta+\gamma}$  are the absorption bands at 763 cm<sup>-1</sup> and 840 cm<sup>-1</sup>, respectively, and the factor 1.26 represents the absorption coefficient ratio of  $\beta$  and  $\alpha$  phases  $\binom{\kappa_{\beta}}{\kappa_{\alpha}}$  (Table 2.1). We note that Equation 2.1 can be used for pure  $\beta$  phase quantification only when  $\gamma$  phase content can be assumed negligible [35]; Figure 2.2 results clearly indicate the presence of  $\gamma$  phase in the pure PVDF and PVDF- BaTiO<sub>3</sub> films, making this a combined  $\beta+\gamma$  phase content estimate. For unannealed and unstretched films, the results indicate a substantial increase in electroactive phases when the BaTiO<sub>3</sub> fraction increases from to 5 wt% ( $\beta+\gamma$  content increases from 53% to 72%), followed by a smaller increase in electroactive phases when the BaTiO<sub>3</sub> fraction increases from 5 to 10wt% ( $\beta+\gamma$  content increases from 72% to 8%). The effectiveness of increasing BaTiO<sub>3</sub> content in promoting  $\beta+\gamma$  phases likely reduces at higher wt% due to the agglomerating tendency of BaTiO<sub>3</sub> nanoparticles producing proportionally less electroactive phase nucleation per filler particle. Annealing does not appear to have a large impact, with all films remaining at

approximately the same  $\beta+\gamma$  phase content before and after annealing (< 4% change). Stretching results in a significant increase in total electroactive phases for pure PVDF but produces a negligible change in the 5 and 10 wt% composite films. For both 5 and 10 wt% BaTiO<sub>3</sub> films, combined electroactive phase content is approximately the same for unannealed vs. stretched films (within 1.5%). We note that separate quantification of  $\beta$  and  $\gamma$  phases using the peak-to-valley method proposed by Cai et al. [16] is complicated here by the presence of BaTiO<sub>3</sub> particles in the composite films, as BaTiO<sub>3</sub> FTIR peaks overlap with those required for peak-to-valley quantification; this issue is further explained in Appendix A (Table A.1), including close-up views of  $\beta$  and  $\gamma$  phase peaks at 812 cm<sup>-1</sup> (Figure A.1), 445 cm<sup>-1</sup> and 464 cm<sup>-1</sup> (Figure A.2), as well as 1234 cm<sup>-1</sup> and 1276 cm<sup>-1</sup> (Figure A.3).

XRD measurements of annealed and stretched films (0, 5, 10 wt% BaTiO<sub>3</sub>) (Figure 2.4) are used to validate FTIR observations, and to further distinguish between  $\beta$  vs.  $\gamma$  phase transitions occurring in the films. For PVDF,  $\alpha$  phase peaks occur at 2 $\theta$  values of 17.6°, 18.3°, 19.8°, and 26.5°;  $\beta$  phase peaks occur at 20.3°, 20.4°, and 20.6°; and  $\gamma$  phase peaks occur at 18.5°, 19.2° and 20° [32], [36]–[39]. BaTiO<sub>3</sub> peaks occur at 2 $\theta$  values of 22.2°, 31.5°, 38.9°, 45°, 50.8°, and 56°[40], [41].

Figure 2.4a, b compares XRD measurements for annealed and stretched films, respectively, for different BaTiO<sub>3</sub> wt%. For 5 and 10 wt% films, BaTiO<sub>3</sub> peaks are visible as expected. In all cases, the primary  $\beta$  phase peak appears larger in the stretched films, with higher BaTiO<sub>3</sub> content generally corresponding to a higher  $\beta$  phase peak value among the samples. A comparison of annealed vs. stretched films shows an increase in  $\beta$  phase peaks with stretching, and the reduction of a "shoulder" of  $\alpha$  and  $\gamma$  phase content in the

17.5°- 20° region (Figure 2.4a, b). For pure PVDF specifically, we note a decrease in  $\alpha$  phase peaks at 17.6°, 18.3°, and 26.5° with stretching, along with a decrease in the  $\gamma$  phase peak at 19.2° and an increase in  $\beta$  phase peaks at 20.3° and 20.6° (Figure 2.4c). The 5 wt% BaTiO<sub>3</sub> film shows a similar result, with a slight decrease in  $\alpha$  phase peaks at 17.6°, 18.3° and a large decrease in the  $\alpha$  phase peak at 19.8°. The 5 wt% BaTiO<sub>3</sub> film also shows a decrease in the  $\gamma$  phase peaks at 18.5° and 19.2°, and an increase in  $\beta$  phase peaks at 20.3°, 20.4°, and 20.6° (Figure 2.4d). The 10 wt% BaTiO<sub>3</sub> film shows decreased  $\alpha$  phase peaks at 17.6°, 19.8°, and 26.5°; decreased  $\gamma$  phase peaks at 18.5°, 19.2° and 20°; and increased  $\beta$  phase peaks at 20.3°, 20.4°, and 20.6° (Figure 2.4e). These results suggest increased  $\beta$  phase content with loss of  $\alpha$  and  $\gamma$  phase content in every stretched film.

# 2.5 Qualitative Comparison of FTIR and XRD Data

Comparison of FTIR and XRD results suggests that stretching of PVDF- BaTiO<sub>3</sub> films results primarily in the conversion of  $\gamma$  to  $\beta$  phase, while stretching of pure PVDF films results primarily in the conversion of  $\alpha$  to  $\beta$  phase. While quantitative FTIR results in Table 2.1 indicate a negligible change in  $\beta$ + $\gamma$  phase with stretching of BaTiO<sub>3</sub>-PVDF films, a study of individual  $\beta$  and  $\gamma$  phase peaks in FTIR and XRD measurements clearly indicates an increase in  $\beta$  phase content and a decrease in  $\gamma$  phase content. Specifically, FTIR results for 5 and 10 wt% PVDF- BaTiO<sub>3</sub> films show the development of unique  $\beta$  phase peaks at 1274 and 1431 cm-1 and a decrease in unique  $\gamma$  phase peaks at 812 and 833 cm-1 with stretching. These changes leave the 840 cm-1 combined  $\beta$ + $\gamma$  phase peak relatively stable, with the  $\beta$  phase gains balancing the  $\gamma$  phase decrease. There are several probable explanations for the observed difference in predominant phase conversion

mechanisms for pure PVDF vs. PVDF- BaTiO<sub>3</sub> films with stretching. Pure PVDF films have a higher percentage of  $\alpha$  phase in their pre-stretched form compared to PVDF-BaTiO<sub>3</sub>; it is possible that the low  $\alpha$  phase content of the composite films does not effectively convert to  $\beta$  phase with stretching (previous studies of pure PVDF stretching typically report ~20% residual  $\alpha$  phase with 4-5x elongation [13,26]). Another possibility is that organic-inorganic interactions between the BaTiO<sub>3</sub> filler and the polymer decreases the mobility of the polymer chain [1,7], such that higher elongation ratios would be needed for  $\alpha$  to  $\beta$  phase conversion in PVDF- BaTiO<sub>3</sub> composites.

## 2.6 Conclusion and Summary

In conclusion, the results presented here indicate a promising shift of PVDF  $\alpha$  and  $\gamma$  phases to  $\beta$  phase upon stretching of PVDF-BaTiO<sub>3</sub> composite films. The maximum electroactive phase content reached in the stretched composite films is 80%, compared to 68% in stretched PVDF. While increasing BaTiO<sub>3</sub> content from 5 to 10 wt% results in higher  $\beta$  phase content, the 10 wt% films have significantly lower mechanical elasticity and break at lower elongation ratios. Mechanical stretching of the composite films is also observed to be less uniform than pure PVDF films. XRD and the FTIR results indicate that PVDF  $\beta$  phase is dominant in the stretched composite films, as stretching predominantly converts  $\gamma$  phase content to  $\beta$  phase in the composite films. In future work, we suggest that the tradeoff between increased electroactive response and lower mechanical flexibility in -PVDF-BaTiO<sub>3</sub> composite films may be improved with surface modification of the BaTiO<sub>3</sub> nanoparticles. Surface modification reduces BaTiO<sub>3</sub> particle agglomeration and creates stronger interfacial bonding between BaTiO<sub>3</sub> and PVDF [27]. We hypothesize these effects

will improve the mechanical properties PVDF-BaTiO3 composite films, enabling larger elongation ratios than achieved in this work and potentially greater conversion of  $\alpha$  and  $\gamma$  phase to  $\beta$  phase.

### 2.7 References

- [1] Y. Bormashenko, R. Pogreb, O. Stanevsky, and E. Bormashenko, "Vibrational spectrum of PVDF and its interpretation," *Polym. Test.*, vol. 23, no. 7, pp. 791–796, Oct. 2004, doi: 10.1016/j.polymertesting.2004.04.001.
- [2] A. Ferri *et al.*, "Probing the local piezoelectric behavior in stretched barium titanate/poly(vinylidene fluoride) nanocomposites," *Compos. Sci. Technol.*, vol. 186, p. 107914, Jan. 2020, doi: 10.1016/j.compscitech.2019.107914.
- [3] L. Li, M. Zhang, M. Rong, and W. Ruan, "Studies on the transformation process of PVDF from α to β phase by stretching," *RSC Adv.*, vol. 4, no. 8, pp. 3938–3943, Dec. 2013, doi: 10.1039/c3ra45134h.
- [4] A. D. Hussein, R. S. Sabry, O. Abdul Azeez Dakhil, and R. Bagherzadeh, "Effect of adding BaTiO<sub>3</sub> to PVDF as Nano generator," *J. Phys. Conf. Ser.*, vol. 1294, no. 2, Oct. 2019, doi: 10.1088/1742-6596/1294/2/022012.
- [5] A. Baji and Y. W. Mai, "Effect of barium titanate reinforcement on tensile strength and dielectric response of electrospun polyvinylidene fluoride fibers," in *Novel Aspects of Nanofibers*, T. Lin, Ed., London, United Kingdom: IntechOpen, 2018, doi: 10.5772/intechopen.74662.
- [6] A. Hartono, Darwin, Ramli, S. Satira, M. Djamal, and Herman, "Electric field poling 2G V/m to improve piezoelectricity of PVDF thin film," *AIP Conf. Proc.*, vol. 1719, no. 1, pp. 2–6, Mar. 2016, doi: 10.1063/1.4943716.
- [7] R. Gregorio, M. Cestari, and F. E. Bernardino, "Dielectric behaviour of thin films of β-PVDF/PZT and β-PVDF/BaTiO<sub>3</sub> composites," *J. Mater. Sci.*, vol. 31, no. 11, pp. 2925–2930, Jun. 1996, doi: 10.1007/BF00356003.
- [8] C. I. E. Flores, J. Gervacio, F. J. Flores-Ruiz, D. Cardona, E. Camps, J. Muñoz-Saldaña, F.J. Espinoza-Beltrán, "Piezoresponse force microscopy studies of pc-BiFeO<sub>3</sub> thin films produced by the simultaneous laser ablation of Bi and FeO<sub>3</sub>," *Mater. Res. Soc. Symp. Proc.*, vol. 1479, no. 78 pp. 33–38, 2012, doi: 10.1557/opl.2012.
- [9] R. Gregorio and E. M. Ueno, "Effect of crystalline phase, orientation and temperature on the dielectric properties of poly (vinylidene fluoride) (PVDF)," *J. Mater. Sci.*, vol. 34, no. 18, pp. 4489–4500, Sep. 1999, doi: 10.1023/A:1004689205706.
- [10] P. Martins, A. C. Lopes, and S. Lanceros-Mendez, "Electroactive phases of poly(vinylidene fluoride): Determination, processing and applications," *Prog. Polym. Sci.*, vol. 39, no. 4, pp. 683–706, Apr. 2014, doi: 10.1016/j.progpolymsci.2013.07.006.
- [11] Z. Yin, B. Tian, Q. Zhu, and C. Duan, "Characterization and application of PVDF and its copolymer films prepared by spin-coating and Langmuir-Blodgett method,"

- Polymers (Basel), vol. 11, no. 12, Dec. 2019, doi: 10.3390/polym11122033.
- [12] M. Sharma, J. K. Quamara, and A. Gaur, "Behaviour of multiphase PVDF in (1–x)PVDF/(x)BaTiO<sub>3</sub> nanocomposite films: Structural, optical, dielectric and ferroelectric properties," *J. Mater. Sci. Mater. Electron.*, vol. 29, no. 13, pp. 10875–10884, Apr. 2018, doi: 10.1007/s10854-018-9163-4.
- [13] A. Salimi and A. A. Yousefi, "FTIR studies of β-phase crystal formation in stretched PVDF films," *Polym. Test.*, vol. 22, no. 6, pp. 699–704, Sep. 2003, doi: 10.1016/S0142-9418(03)00003-5.
- [14] S. H. Lee and H. H. Cho, "Crystal structure and thermal properties of poly(vinylidene fluoride)-carbon fiber composite films with various drawing temperatures and speeds," *Fibers Polym.*, vol. 11, no. 8, pp. 1146–1151, Dec. 2010, doi: 10.1007/s12221-010-1146-x.
- [15] M. Khalifa, S. Janakiraman, S. Ghosh, A. Venimadhav, and S. Anandhan, "PVDF/halloysite nanocomposite-based non-wovens as gel polymer electrolyte for high safety lithium ion battery," *Polym. Compos.*, vol. 40, no. 6, pp. 2320–2334, Oct. 2019, doi: 10.1002/pc.25043.
- [16] X. Cai, T. Lei, D. Sun, and L. Lin, "A critical analysis of the α, β and γ phases in poly(vinylidene fluoride) using FTIR," *RSC Adv.*, vol. 7, no. 25, pp. 15382–15389, Mar. 2017, doi: 10.1039/c7ra01267e.
- [17] M. Benz, W. B. Euler, and O. J. Gregory, "The role of solution phase water on the deposition of thin films of poly(vinylidene fluoride)," *Macromolecules*, vol. 35, no. 7, pp. 2682–2688, Feb. 2002, doi: 10.1021/ma011744f.
- [18] S. K. Karan, D. Mandal, and B. B. Khatua, "Self-powered flexible Fe-doped RGO/PVDF nanocomposite: An excellent material for a piezoelectric energy harvester," *Nanoscale*, vol. 7, no. 24, pp. 10655–10666, May 2015, doi: 10.1039/c5nr02067k.
- [19] S. F. Mendes, C. M. Costa, C. Caparros, V. Sencadas, and S. Lanceros-Méndez, "Effect of filler size and concentration on the structure and properties of poly(vinylidene fluoride)/BaTiO<sub>3</sub> nanocomposites," *J. Mater. Sci.*, vol. 47, no. 3, pp. 1378–1388, Sep. 2012, doi: 10.1007/s10853-011-5916-7.
- [20] H. Bai, X. Wang, Y. Zhou, and L. Zhang, "Preparation and characterization of poly(vinylidene fluoride) composite membranes blended with nano-crystalline cellulose," *Prog. Nat. Sci. Mater. Int.*, vol. 22, no. 3, pp. 250–257, Jun. 2012, doi: 10.1016/j.pnsc.2012.04.011.
- [21] T. Nishiyama, T. Sumihara, E. Sato, and H. Horibe, "Effect of solvents on the crystal formation of poly (vinylidene fluoride) film prepared by a spin-coating process," *Polym. J.*, vol. 49, no. 3, pp. 319–325, Dec. 2017, doi: 10.1038/pj.2016.116.

- [22] L. Ruan, X. Yao, Y. Chang, L. Zhou, G. Qin, and X. Zhang, "Properties and applications of the β phase poly(vinylidene fluoride)," *Polymers (Basel)*, vol. 10, no. 3, pp. 1–27, Feb. 2018, doi: 10.3390/polym10030228.
- [23] I. Y. Abdullah, M. H. H. Jumali, M. Yahaya, and H. M. Shanshool, "Facile formation of β poly (vinylidene fluoride) films using the short time annealing process," *Adv. Environ. Biol.*, vol. 9, no. 20, pp. 20–27, Sep. 2015.
- [24] N. M. Zali, C. S. Mahmood, S. M. Mohamad, C. T. Foo, and J. A. Murshidi, "X-ray diffraction study of crystalline barium titanate ceramics," *AIP Conf. Proc.*, vol. 1584, no. 1, pp. 160–163, Feb. 2015, doi: 10.1063/1.4866124.
- [25] Z. Lazarević*et al.*, "Characterization of barium titanate ceramic powders by Raman spectroscopy," *Acta Phys. Pol. A*, vol. 115, no. 4, pp. 808–810, Sep. 2009, doi: 10.12693/APhysPolA.115.808.
- [26] V. Sencadas, R. Gregorio, and S. Lanceros-Méndez, "α to β phase transformation and microestructural changes of PVDF films induced by uniaxial stretch," *J. Macromol. Sci. Part B Phys.*, vol. 48, no. 3, pp. 514–525, May. 2009, doi: 10.1080/00222340902837527.
- [27] K. Yu, H. Wang, Y. Zhou, Y. Bai, and Y. Niu, "Enhanced dielectric properties of BaTiO<sub>3</sub>/poly(vinylidene fluoride) nanocomposites for energy storage applications," *J. Appl. Phys.*, vol. 113, no. 3, pp. 034105, Jan. 2013, doi: 10.1063/1.4776740.

Table 2.1: Quantitative comparison of electroactive phase content.

BaTiO <sub>3</sub> content	Sample	F(β+γ)
0 wt%	Unannealed	52.9%
	Annealed	52.4%
	Stretched	67.7%
5 wt%	Unannealed	71.7%
	Annealed	75.2%
	Stretched	70.2%
10 wt%	Unannealed	79.8%
	Annealed	76.2%
	Stretched	79.8%

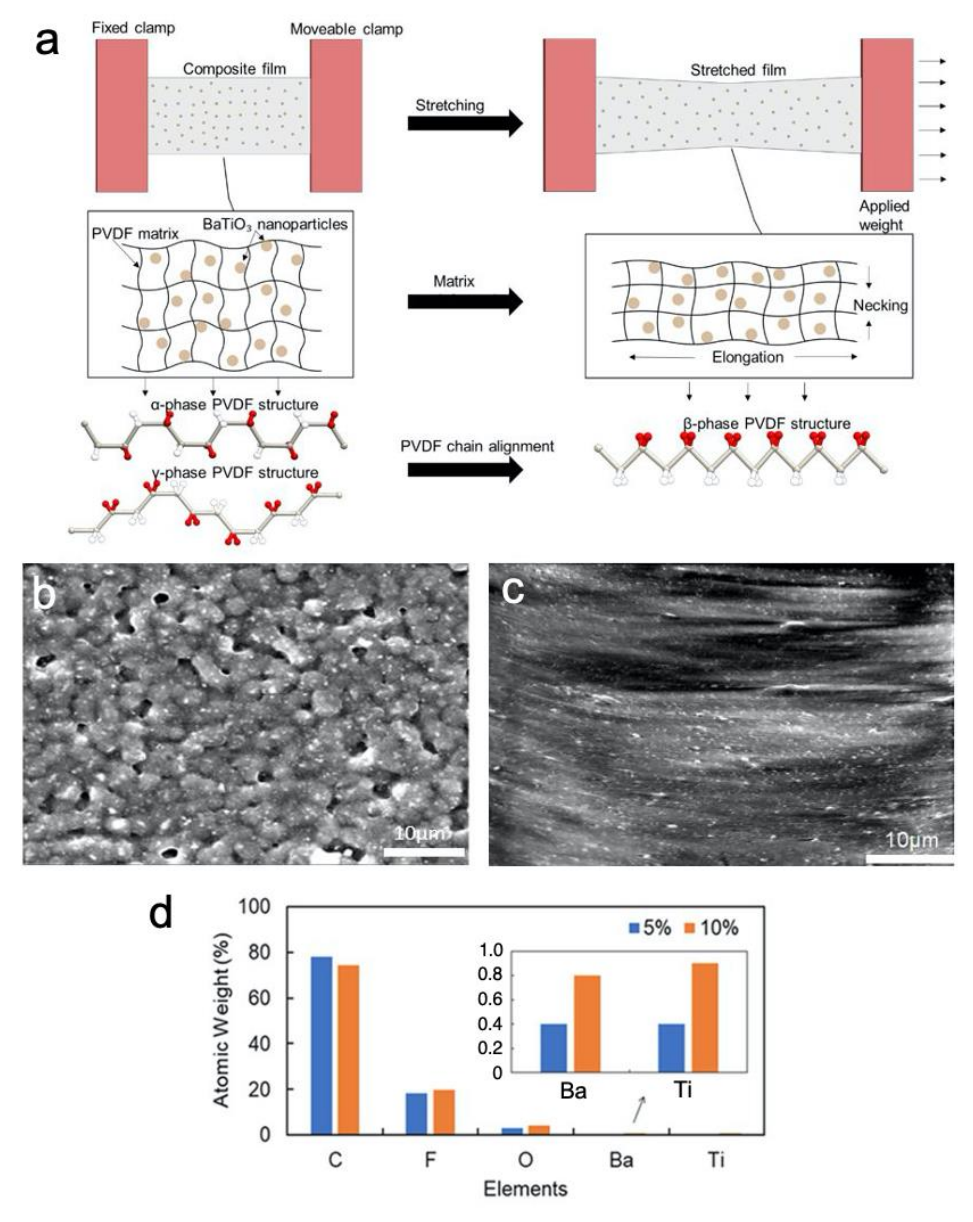


Figure 2.1: a) Conceptual illustration of PVDF-BaTiO<sub>3</sub> composite structure before and after stretching, including the applied uniaxial stretching mechanism, polymer matrix elongation, and conversion of  $\alpha$  and  $\gamma$  phase PVDF to  $\beta$  phase. SEM images of a PVDF-BaTiO<sub>3</sub> composite film (10 wt%) before (b) and after (c) stretching. D) EDX measurements of 5 and 10 wt% PVDF-BaTiO<sub>3</sub> films.

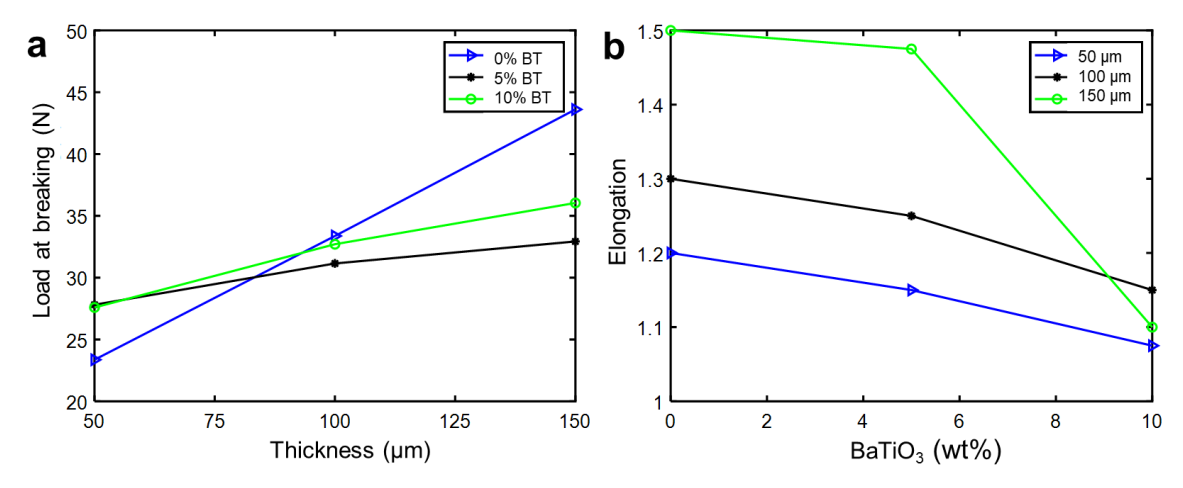


Figure 2.2: Effect of starting film thickness and BaTiO<sub>3</sub> wt% on the maximum load applied to the PVDF-BaTiO<sub>3</sub> films at breaking (a) and the maximum elongation (stretching ratio) at breaking (b).

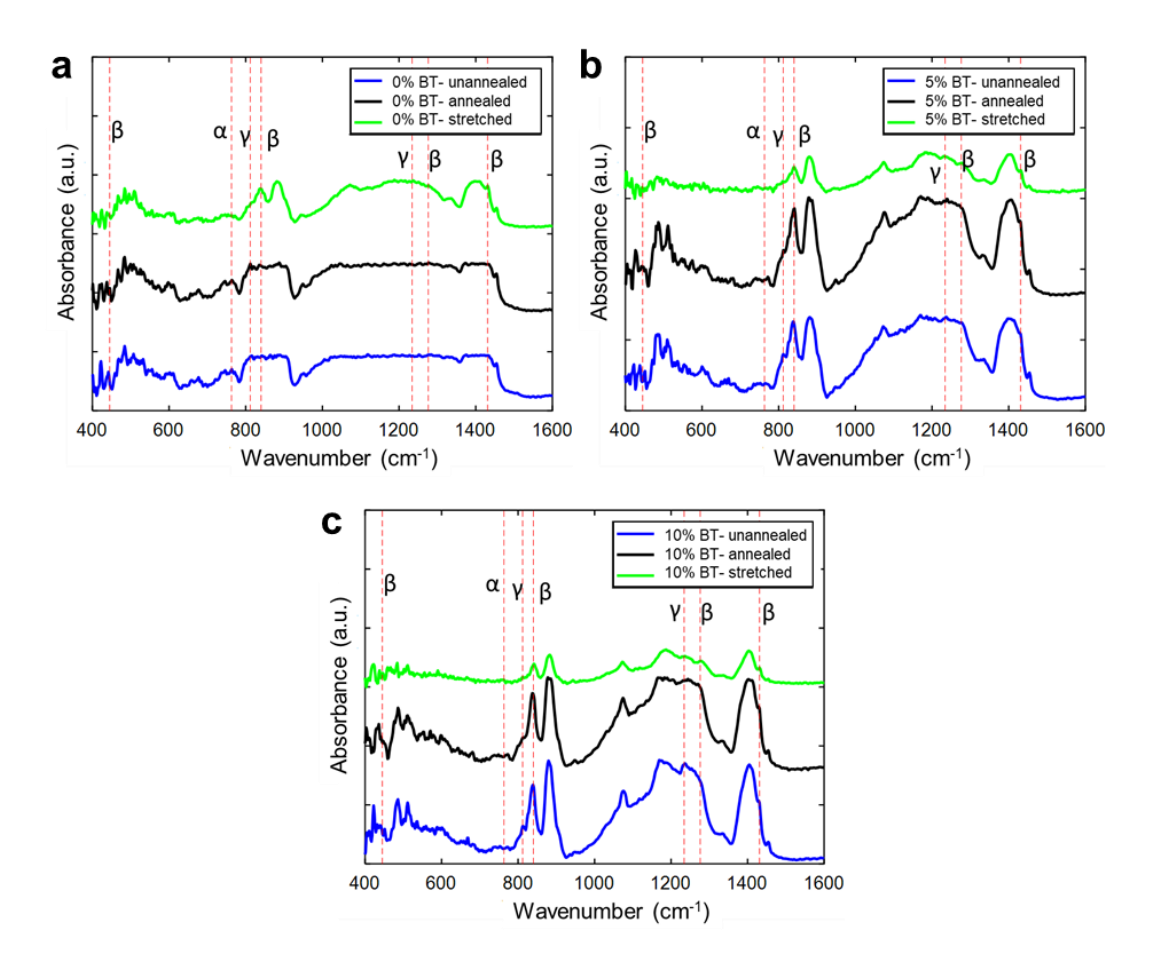


Figure 2.3: FTIR spectrum of unannealed, annealed and stretched PVDF- BaTiO<sub>3</sub> films with: a) 0 wt% BaTiO<sub>3</sub> (pure PVDF), (b) 5 wt% PVDF- BaTiO<sub>3</sub>, (c) 10 wt% PVDF-BaTiO<sub>3</sub>.

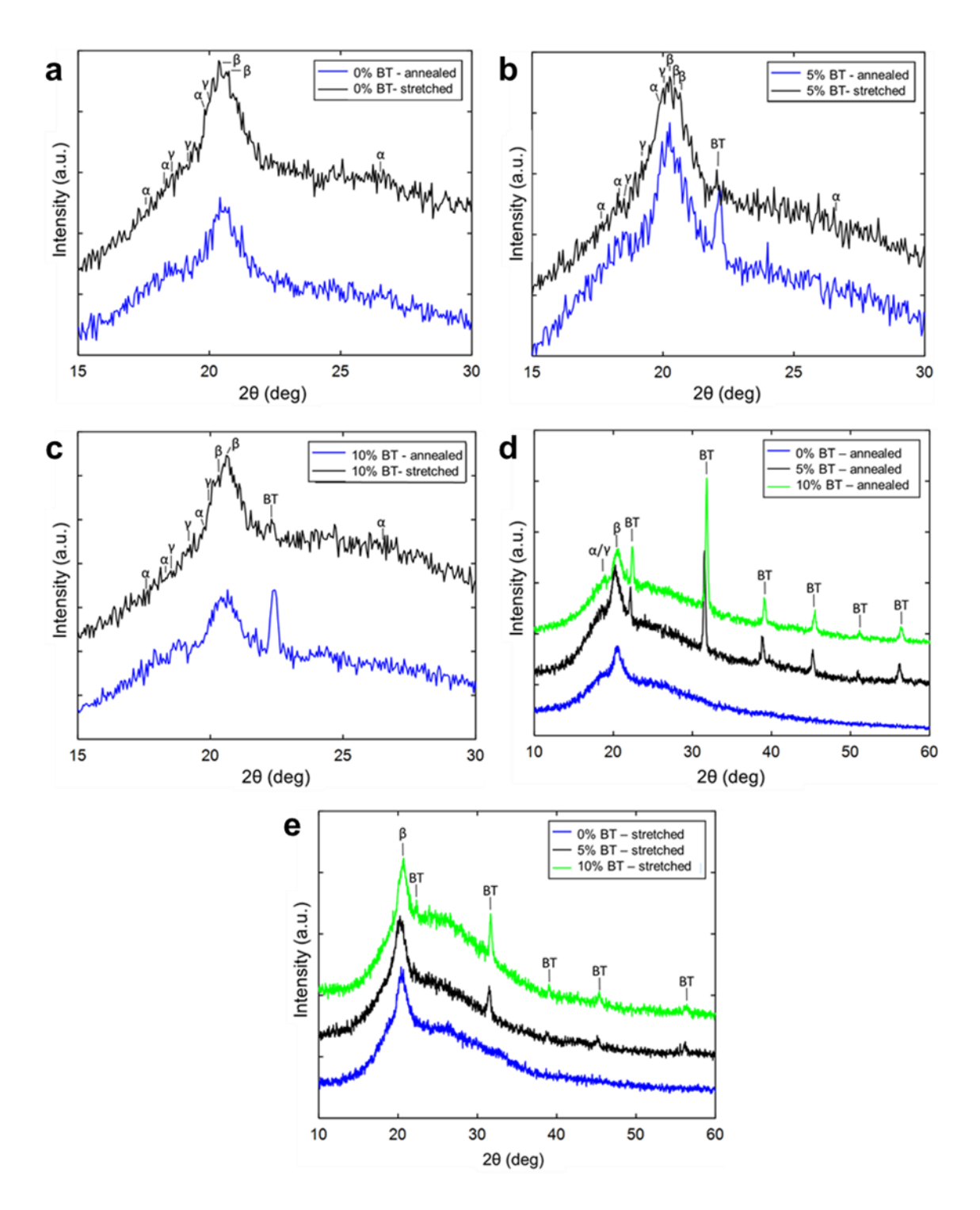


Figure 2.4: Comparison of XRD results for a) annealed PVDF films with 0, 5, and 10 wt% BaTiO<sub>3</sub>, b) stretched PVDF films with 0, 5, and 10 wt% BaTiO<sub>3</sub>, c) pure PVDF annealed and stretched films, d) 5 wt% PVDF- BaTiO<sub>3</sub> annealed and stretched films, and e) 10 wt% PVDF- BaTiO<sub>3</sub> annealed and stretched films.

#### CHAPTER 3

# EFFECT OF PORE STRUCTURE ON THE PIEZOELECTRIC PROPERTIES OF PVDF-BATIO<sub>3</sub> COMPOSITE FILMS

## 3.1 Introduction

Polyvinylidene fluoride (PVDF) is a piezoelectric polymer with many favorable properties compared to crystalline or ceramic piezoelectrics, including: mechanical flexibility, chemical inertness, and ease of fabrication as a piezo-active thin film. Compared to crystalline or ceramic piezoelectrics, however, PVDF has lower stiffness and lower piezoelectric strain coefficients ( $d_{xx}$ ), leading to lower piezo-active response and limiting its power production. One method to increase PVDF piezoelectric performance is to create composite films with ceramic filler particles, such as PVDF- barium titanate (PVDF-BaTiO<sub>3</sub>). PVDF- BaTiO<sub>3</sub> composites demonstrate improved piezoelectric response due to the increased piezo-activity of the filler particle, while retaining the mechanical flexibility of the polymer matrix [1]. To-date, composite piezo-active films have found use in applications such as: pressure sensors [2], prospective medical implants like pacemakers [3], wearable energy harvesters [4], and filtration of gases and fluids [5]. In addition to good piezoelectric response, many applications of piezo-active films require porous piezoelectric materials. In applications such as tissue repair scaffolding [6], "self-charging

power cells" [7], and liquid or gas filtration devices, the porosity and pore structure of the piezo-active material may be as important as the piezoelectric response. Despite the importance of achieving high piezoelectric response and high porosity in such applications, to-date there have been no investigations of process-structure-property relationships for porous PVDF-BaTiO<sub>3</sub> composites. For PVDF-BaTiO<sub>3</sub> films, increasing piezoelectric performance often comes at the cost of reduced porosity through methods like hot-pressing and stretching [8-9]. The aim of this study is to combine highly piezo-active BaTiO<sub>3</sub> particles within a porous PVDF film through the use of coagulation baths, resulting in a functional-yet-porous film with good piezoelectric properties.

Previous studies have elucidated many important structure-property relationships of porous piezoelectric materials, including relationships between pore structure and piezoelectric activity. Porous structures are generally more flexible than the bulk material, so larger strains and voltage outputs can be expected for similar forces with small-to-moderate levels of porosity [10]. The addition of nanopores into solid BaTiO<sub>3</sub> material was found to improve  $d_{33}$  output by 35% when compared to dense material [11]. With increasing pore size and porosity, however, the material may begin to lose piezoelectric performance compared to the bulk material [12-14]. During modification of lead zirconate titanate (PZT) density for acoustic use, introducing 45% porosity in the PZT reduced piezoelectric  $d_{33}$  by 40% compared to 5% porous PZT [15]. When annealing sputtered zinc oxide thin films at different temperatures to control porosity, piezoelectric response increased up to 2.5x for 45 nm pores compared to bulk zinc oxide as pores were created, before decreasing sharply to 0.5x as pore size increased to 90 nm [16]. Pore structure and ordering also influence piezoelectric response, with smaller, highly ordered pores often

increasing piezo-activity compared to larger, disordered pores. When structured by freeze-templating, the most highly ordered middle region of porous PZT had higher piezoelectric response than the disordered top and bottom regions [17]. Finally, porosity can create additional complicating effects in ceramic and polymer piezoelectric materials. Introducing porosity in piezoelectric ceramics impacts ferroelectric domains and electric field distribution, reducing residual polarization by lowering material polarization near pores [18]. Pores also lower capacitance, create weaknesses and fatigue locations, and increase risk of dielectric breakdown [19-20]. The presence of these complex factors necessitates the study of process-structure-property relationships in porous piezoelectric materials.

In addition to the above effects present in porous piezo-active materials in general, porosity impacts the piezoelectric performance of polymer films by changing the crystallization of the polymer matrix compared to bulk polymer matrices. In this way, structured pores can facilitate greater piezoelectric responses in polymer films by increasing the amount of piezo-active crystal phases present during material crystallization. Working with PVDF, Zhang *et al.* found confinement created by freeze-templating caused much higher crystallization of piezo-active phases within the polymer, improving  $d_{33}$  by 3x compared to bulk PVDF films [21]. Pore separation also affects piezoelectric response. In a study of porous PVDF for sonic wave-driven nanogenerators, Cha *et al.* observed a sharp decrease in piezoelectric activity of porous PVDF when the distance between pores increased above 100 nm [22]. In the conversion of solid poly(vinylidene fluoride-trifluoroethylene) (PVDF-TrFE) nanorods to hollow tubes, a similar trend is observed, with the larger pore size of hollow tubes giving the matrix a different crystalline structure and resulting in half the polarization of rods with smaller domain sizes [23]. In a different study,

33% porous PVDF-TrFE was created and compared to commercial films, and found to have worse performance at every poling condition, with the pores resulting in less overall polarization after a poling procedure [24]. Clearly, the impact of porosity on polymer matrices will depend highly on the procedure and resulting pore structure, with some methods improving and others worsening piezoelectric characteristics.

Porosity may be introduced into films through a variety of methods. When working with materials that can be dissolved in a solvent, such as PVDF, the solution can be cast onto glass. Solvent evaporation under ambient conditions produces a thin film with low porosity from minor voids and defects [25]. Templating approaches use a sacrificial material to create porous structures. Pore shape can be manipulated by changing the sacrificial material structure, with long through-pores created by nanowire templates, and homogenously mesoporous films by nanoparticle templates [22]. Mao et al. prepared porous PVDF films by zinc oxide nanoparticle templating. The researchers observed 3x the piezoelectric output voltage of non-porous PVDF with 30% porosity; increasing porosity beyond 30% lowered voltage outputs [26]. While there are comparably fewer studies of piezo-active composite films that are also porous, results indicate that these films can also achieve comparable or even improved piezoelectric response compared to their non-porous counterparts. Zhang et al. introduced polydimethylsiloxane (PDMS) into a PVDF matrix to tune the mechanical frequency response of the film to that of biological systems, resulting in films with comparable output voltage and current to non-porous films [27]. Utilizing engineered nanoparticles in composite piezoelectric materials can further improve film performance. Khan et al. made perovskite-polymer (hybrid halide perovskite–FAPbBr2I–PVDF) composites with 60% porosity and five times the voltage output of a 20% porous PVDF film with no fillers under the same compressive stress [28].

Phase inversion is a well-studied method to create controlled pores in polymer thin films [29]. In phase-inversion, the casting solvent is replaced with a secondary non-solvent or non-solvent mixture in a coagulation bath. The resulting demixing process (Figure 3.1) produces a porous film, with the specific structure depending on the choice of solvent, nonsolvent, polymer, and any additives [30]. Phase inversion is a facile method of achieving porosities greater than 60% in thin polymer films. Previous studies of PVDF coagulation baths have identified two main pore structures that can form in the polymer matrix: fingerlike channels and interconnected mesh. Adding ethanol to the non-solvent deionized (DI) water bath directs pore structure depending on the ratio of ethanol-to-water, with increasing ethanol concentration producing more interconnected mesh vs. finger-like structures [30-33]. The effect results from the speed with which phase inversion occurs in pure DI water vs. ethanol-water mixture, with the slower ethanol-solvent interaction allowing mesh structures to form in the PVDF. To-date, phase inversion has not been applied to ceramicpolymer composite piezoelectric thin films, and questions remain as to the effect of this method on the porous structure and resulting piezo-activity of the composite.

This work investigates, for the first time, the effects of pore structure on the piezoelectric activity of PVDF- BaTiO<sub>3</sub> composite films produced by phase inversion. By varying the ethanol-water ratio of the phase inversion process, PVDF- BaTiO<sub>3</sub> composite films with different pore structures are created. The effect of pore structure on the ability to electrostatically pole both the BaTiO<sub>3</sub> and PVDF components of the composite films is explored. The effect of pore structure on the mechanical properties and the piezoelectric voltage response of the composite films is examined when the films are subjected to

loading under tension and compression. The results are correlated with the pore structure and porosity of the films determined from SEM imaging, and the observed trends in piezoelectric performance and porosity discussed. A transition from finger-like structures to interconnected mesh is observed in the PVDF- BaTiO<sub>3</sub> composites as ethanol concentration increases, resulting in increasing Young's modulus and lower voltage output under compressive loading. Finger-like structures are found to be most effective for achieving high piezoelectric response and good porosity for the flexible, composite structures. It is anticipated that the results presented here can guide future designs of highly porous ceramic-polymer piezoelectric materials synthesized by phase inversion.

### 3.2 Methods

## 3.2.1 PVDF- BaTiO<sub>3</sub> Porous Film Fabrication

BaTiO<sub>3</sub> particles were purchased from Stanford Advanced Materials (BaTiO<sub>3</sub>, 300-700 nm particle size, tetragonal structure). All other materials were purchased from Millipore Sigma and used as received. PVDF powder (average MW~534,000 g/mol) was dissolved in N, N-dimethylformamide (DMF) at 12 wt% (w/w) in a 45°C water bath. Large BaTiO<sub>3</sub> particles were lightly broken down using a spatula, and a suspension of BaTiO<sub>3</sub> particles was created in DMF such that total PVDF-DMF ratio becomes 15 wt% (w/w) once mixed. The homogeneous BaTiO<sub>3</sub> dispersion was added to the PVDF-DMF solution at room temperature and sonicated for 1 hour. PVDF-BaTiO<sub>3</sub> films were made by drop-casting the prepared slurry onto a glass plate using a doctor blade and Kapton tape to obtain uniform film thicknesses of ~50 μm (after annealing). The coated glass plates were immediately immersed in the prepared coagulation baths for 20 minutes at room

temperature (Figure 3.1). Coagulation baths were prepared with DI water: ethanol weight ratios of 100:0 ("DI"), 85:15 ("DI15E"), 70:30 ("DI30E") and 55:45 ("DI45E"). The films were dried at 60°C in an oven to evaporate the DMF, then annealed for 5 hours at 90°C. The composite films have a PVDF: BaTiO<sub>3</sub> ratio of 80:20 (w/w%). An electric field of 15 MV/m at 120°C was applied for 30 minutes to pole the BaTiO<sub>3</sub> particles in the films followed by a 30-minute cooling period under the same electric field. Two stainless steel plates (2 mm thickness) were used as electrodes for the poling process. For comparison with the porous composite samples, a commercial, non-porous, pure PVDF piezoelectric film was purchased from TE Connectivity (52 μm thickness) and tested under the same conditions as the PVDF- BaTiO<sub>3</sub> films.

#### 3.2.2 Characterization

PVDF-BaTiO<sub>3</sub> film morphology was characterized by scanning electron microscopy (SEM) imaging using a FEI Quanta 600F. To obtain clean cross-sections of the films, the films were immersed in liquid nitrogen prior to breaking. Cross-sectional SEM images were taken close to the center of each 6 x 3 cm<sup>2</sup> film. PVDF-BaTiO<sub>3</sub> film porosity was measured by immersing the films in 1-butanol for 1 hour, with the mass of the films measured before and after immersion [32]. Porosity (ε) was calculated using Equation 3.1:

$$\varepsilon = \frac{\frac{m_b}{\rho_b}}{\frac{m_p}{\rho_p} + \frac{m_b}{\rho_b}} \tag{3.1}$$

where  $\rho_p$ ,  $\rho_b$  are the densities of PVDF and 1-butanol, respectively, and  $m_p$ ,  $m_b$  are the mass of the dry film and film after soaking, respectively. Young's moduli (Y) of PVDF-BaTiO<sub>3</sub> films were measured with an Instron 5969 using a 1 kN load cell. Dog bone-shaped films were subjected to <2% strain to be in the elastic region of the stress-strain curve.

Young's moduli of the films were extracted from the collected stress-strain data following Equation 3.2:

$$Y = \frac{T}{S} \tag{3.2}$$

where *T* is applied stress and *S* is strain. Customized 3D-printed clamps were used to secure PVDF-BaTiO<sub>3</sub> films in the Instron. The voltage response of the films under tensile stress was measured by applying 1-2% strain along the length of the film. For compressive stress testing, films were placed between two metal discs of 176 mm<sup>2</sup>. Force was applied to the metal discs in the Instron resulting in compressive stress through the thickness of the film. The films were stressed at 1, 3, 5, 10, and 20 N forces over 10 cycles each to test open circuit voltage response and deformation. Voltage response was measured for the commercial film sample under the same conditions.

## 3.3 Results and Discussion

Figure 3.2 presents cross-sectional SEM images of PVDF-BaTiO3 films fabricated under four coagulation bath water: ethanol weight ratios: 1) 100:0, referred to hereafter as "DI" films (Figure 3.2a); 2) 85:15, referred to as "DI15E" films (Figure 3.2b); 3) 70:30, referred to as "DI30E" films (Figure 3.2c); and 4) 55: 45, referred to as "DI45E" films (Figure 3.2d). SEM images in Figure 3.2 are consistent with the orientation of the films during drop-casting (i.e. the "top" surface in the images was at the solution-air interface during fabrication, and the "bottom" surface in the images was positioned along the glass slide). The films show a trend of finger-like to mesh-like structure conversion as bath ethanol content rises. DI films (Figure 3.2a) are characterized by finger-like structures running vertically from the top to bottom surface

of the film. The average width of the finger-like structures is 8.5 µm; smaller circular pores within those structures have approximately 0.82 µm average diameter. DI15E films (Figure 3.2b) have finger-like structures confined to the top surface of the films, with mesh-like structures present in the bottom-half. The average width of the finger-like structures is less than that of DI films at approximately 3.84 µm. Smaller circular pores in both upper and lower regions of the DI15E films have also decreased in size, with an average diameter of 0.68 µm. Above 30% ethanol content (DI30E and DI45E films), finger-like structures are not found anywhere along the cross-sectional images, and the film structure becomes entirely mesh-like (Figure 3.2c, d). The average pore size of the mesh-like films is approximately 0.55 µm and 0.58 µm for DI30E and DI45E films, respectively. Pore formation in coagulation baths, including pore structure and size, depends on the coagulation capability of the non-solvent in the non-solvent-induced phase inversion processes. The precipitation rate of PVDF is highest in pure DI water. With the addition of the ethanol, the solvent/non-solvent mixing rate is reduced and the precipitation rate of PVDF decreases [31]. This results in the different morphologies observed in the films. A high precipitation rate of PVDF produces larger pore structures and more continuous pores (i.e. finger-like structures in Figure 3.2a, b). In Figure 3.2b, finger-like structures preferentially form at the polymer/non-solvent interface, where solvent/non- solvent mixing occurs more rapidly than at the polymer-glass interface. The results presented in Figure 3.2 for PVDF-BaTiO<sub>3</sub> composite films match previous studies of coagulation bath pore formation with pure PVDF films [30-33], indicating that the introduction of 20 wt% BaTiO<sub>3</sub> particles does not visibly affect the phase-inversion process of PVDF. The liquid-liquid demixing mechanism overcomes the localized impact BaTiO<sub>3</sub> particles have on the surrounding matrix, making coagulation baths a useful simple tool for guiding porous composite film structure. To ensure repeatability of the observed pore structures, three independently-prepared films were imaged for each of the coagulation bath conditions. Similar trends in pore structure and size were observed in all three batches of films.

Table 3.1 provides average porosity and Young's modulus measurements for PVDF-BaTiO<sub>3</sub> films prepared under varying coagulation bath conditions. Each reported value is an average of measured values for three batches of films prepared independently. The results are plotted in Figure 3.3 to show a clear relationship between coagulation bath ethanol content and the resulting film porosity and Young's modulus. Error bars represent standard deviation of measurements. A negative correlation is observed between ethanol content and porosity. This is likely due to the conversion of larger finger-like pore structures to smaller mesh-like pores with increasing ethanol content (Figure 3.2). However, despite the decrease in porosity, even the DI45E film has high porosity near 60%, with all other films remaining above 60% porosity. With decreasing porosity and pore size, we observe an increase in Young's modulus of the films. This trend matches expectations for porous film performance, as more material necessarily provides more resistance to applied force. Within the range of porosities tested, relatively small changes in film porosity result in large changes in Young's modulus; for example, a 7% decrease in the absolute value of porosity from DI to DI45E samples results in a 64% change in Young's modulus from 224 MPa to 368 MPa. We measured the Young's modulus of the commercial PVDF film (2.5% porosity) to be 2 GPa; as expected, the porous films are significantly more compliant than the non-porous commercial film.

The piezoelectric performance of the PVDF-BaTiO<sub>3</sub> films was tested under

compressive and tensile loading conditions. Under compressive loading, the porous structure of the films was observed to permanently deform if the applied compressive force was 10 N or higher. At greater than 10 N forces, the piezoelectric voltage decreased with every cycle and the films became effectively non-responsive after ~30 cycles. SEM inspection of the films after compression at  $\geq 10$  N loading confirmed the permanent deformation of porous structures in all films. All subsequent compressive testing was performed at lower forces to ensure sustained voltage output with repeated cycling. Figure 3.4a plots the open circuit piezoelectric voltage response of a DI film under 3 N of cyclic compressive force. The film produced a stable peak-to-peak voltage (V<sub>pp</sub>) response of 400 mV over the ten cycles measured. Similar voltage profiles were observed for all other PVDF-BaTiO<sub>3</sub> films under the same loading conditions, with differences in V<sub>pp</sub>. Figure 3.4b compares the piezoelectric voltage response of the PVDF-BaTiO<sub>3</sub> films as a function of porosity under consistent 3 N compressive loading. Interestingly, the voltage response is highest for DI and DI15E samples, with a substantial decrease in V<sub>pp</sub> occurring between DI15E and DI30E samples. The results indicate that porosity and pore structure have a significant effect on piezoelectric voltage response in PVDF-BaTiO<sub>3</sub> films, with the DI film producing  $7x\ V_{pp}$  output compared to the DI45E film. The large observed increase in V<sub>pp</sub> with increasing porosity is much larger than might be expected given the modest changes in porosity. Of particular note is the sharp decrease in piezoelectric performance observed when the finger-like structures disappear between the DI/DI15E and DI30E/DI45E pairings. It is hypothesized that these observations can be attributed to differences in the interaction between ceramic BaTiO<sub>3</sub> particles and the PVDF polymer matrix that arise with different film morphologies. Under tensile loading, all four PVDF-

BaTiO<sub>3</sub> film morphologies produced low  $V_{pp}$  output. Typical  $V_{pp}$  responses ranged from 10-20 mV under tensile strain of 1-2%. We believe this is due to poor stress transfer from the PVDF matrix to the BaTiO<sub>3</sub> particles in the longitudinal direction. In addition, the  $d_{31}$  coefficient of BaTiO<sub>3</sub> is lower than  $d_{33}$ , resulting in lower piezoelectric response in tension vs. compression.

Under the poling conditions applied in this study (15 MV/m), the PVDF matrix is assumed to be weakly poled, and the majority of the piezoelectric response is assumed to arise from the BaTiO<sub>3</sub> particles. Electrostatic poling of PVDF films is typically performed at 50-120 MV/m [34-35], while BaTiO<sub>3</sub> particles of the size used here (300-700 nm) may be poled near 10 MV/m [36-37]. Introducing porosity into PVDF-BaTiO<sub>3</sub> films through coagulation baths makes electrostatic poling substantially more difficult, with film breakdowns commonly observed even at relatively low applied fields. For porous PVDF-BaTiO<sub>3</sub> films, dielectric breakdown was consistently observed at poling fields >18 MV/m. At 15 MV/m, it is assumed that the well-poled BaTiO<sub>3</sub> particles contribute most of the piezoelectric response in the composite PVDF-BaTiO<sub>3</sub> films. This suggests that more effective stress transfer to the BaTiO<sub>3</sub> particles occurs with the finger-like structure *vs*. interconnected mesh.

We propose two possible mechanisms by which the polymer pore structure affects stress transfer to the ceramic particles: 1) variations in localized stress states around pores, and 2) changing BaTiO<sub>3</sub> particle orientation during deformation. A finite element analysis by Tim Kowalchik revealed the stress within the finger-like structure appears more aligned, and would stress corresponding BaTiO<sub>3</sub> particles in compression primarily in alignment with their poling direction. Whereas within the mesh-like structure, the various connections

between cavities allow large stresses to form in a multitude of directions. While BaTiO<sub>3</sub> particles will be stressed in compression, there will be larger variations in total stress directions, compromising the corresponding piezoelectric voltage production.

# 3.4 Conclusion and Summary

The results presented in this study show a large difference in PVDF-BaTiO<sub>3</sub> composite film performance based on the different morphology of the films. There is a pronounced structural variation as ethanol: DI water ratio varies in the coagulation baths. DI and DI15E films present larger finger-like pore structures, while DI30E and DI45E films consist entirely of mesh-like structures. There is a noted decrease in finger width and pore size between DI and DI15E samples, and pore size further decreases between the finger-like DI/DI15E and mesh-like DI30E/DI45E pairing. There is a slight decrease in film porosity with increasing ethanol content, shifting from 64.9% with the DI sample to 58.2% with the DI45E sample. This corresponds to an expected increase in Young's modulus, with the DI45E sample having 64% higher stiffness than the DI sample. The piezoelectric response of films under compressive loading reveals greater V<sub>pp</sub> with increasing porosity and increasing finger-like structures (400 mV for the DI film vs. 57 mV for DI45E film under 3 N). We hypothesize that the lack of finger-like structures in the DI30E and DI45E films leads to the observed difference in V<sub>pp</sub>. The finger-like structures may be more uniformly stressing the BaTiO<sub>3</sub> particles along the cavity walls, while meshlike structures may be allowing particles to shift and change alignment during deformation. Finger-like pore structures have a much more ordered stress distribution compared to mesh-like structures, with a well-aligned compressive stress constituting the majority of stresses in the finger-like films. The mesh-like structure has poor alignment between stresses and large variations in stress values throughout the structure with the presence of large shear stresses between pore connections. In combination, these could lead to the difference in piezoelectric performance of the discrete film morphologies.

#### 3.5 References

- [1] A. Chiolerio, M. Lombardi, A. Guerriero, G. Canavese, S. Stassi, R. Gazia, V. Cauda, D. Manfredi, A. Chiodoni, A. Verna, M. Cocuzza, L. Montanaro, and C. F. Pirri, "Effect of the fabrication method on the functional properties of BaTiO<sub>3</sub>: PVDF nanocomposites," *J. Mater. Sci.*, vol. 48, no. 20, pp. 6943–6951, Oct. 2013, doi: 10.1007/s10853-013-7500-9.
- [2] Y. Yang, H. Pan, G. Xie, Y. Jiang, C. Chen, Y. Su, Y. Wang, and H. Tai, "Flexible piezoelectric pressure sensor based on polydopamine-modified BaTiO<sub>3</sub>/PVDF composite film for human motion monitoring," *Sens. Actuators A Phys.*, vol. 301, pp. 111789, Dec. 2020, doi: 10.1016/j.sna.2019.111789.
- [3] Z. Xu, C. Jin, A. Cabe, D. Escobedo, N. Hao, I. Trase, A. B. Closson, L. Dong, Y. Nie, J. Elliott, M. D. Feldman, Z. Chen, and J. X. J. Zhang, "Flexible energy harvester on a pacemaker lead using multibeam piezoelectric composite thin films," *ACS Appl. Mater. Interfaces*, vol. 12, no. 30, pp. 34170–34179, Jun. 2020, doi: 10.1021/acsami.0c07969.
- [4] L. M. Swallow, J. K. Luo, E. Siores, I. Patel, and D. Dodds, "A piezoelectric fibre composite based energy harvesting device for potential wearable applications," *Smart Mater. Struct.*, vol. 17, no. 2, pp. 025017, Apr. 2008, doi: 10.1088/0964-1726/17/2/025017
- [5] M. T. Darestani, H. G. L. Coster, and T. C. Chilcott, "Piezoelectric membranes for separation processes: Operating conditions and filtration performance," *J. Membr. Sci.*, vol. 435, pp. 226–232, May 2013, doi: 10.1016/j.memsci.2013.02.024.
- [6] Y. Zhang, L. Chen, J. Zeng, K. Zhou, and D. Zhang, "Aligned porous barium titanate/hydroxyapatite composites with high piezoelectric coefficients for bone tissue engineering," *Mater. Sci. Eng. C*, vol. 39, no. 1, pp. 143–149, Jun. 2014, doi: 10.1016/j.msec.2014.02.022.
- [7] A. Ramadoss, B. Saravanakumar, S. W. Lee, Y. S. Kim, S. J. Kim, and Z. L. Wang, "Piezoelectric-driven self-charging supercapacitor power cell," *ACS Nano*, vol. 9, no. 4, pp. 4337–4345, Mar. 2015, doi: 10.1021/acsnano.5b00759.
- [8] A. Jain, P. K. J. Prashanth, A. Kr. Sharma, A. Jain, and P. N. Rashmi, "Dielectric and piezoelectric properties of PVDF/PZT composites: A review," *Polym. Eng. Sci.*, vol. 55, no. 7, pp. 1589–1616, Jul. 2015, doi: 10.1002/pen.24088.
- [9] F. Khan, T. Kowalchik, S. Roundy, and R. Warren, "Stretching-induced phase transitions in barium titanate-poly(vinylidene fluoride) flexible composite piezoelectric films," *Scripta Mater.*, vol. 193, pp. 64–70, Mar. 2021, doi: 10.1016/j.scriptamat.2020.10.036.
- [10] M. M. Abolhasani, M. Naebe, M. Hassanpour Amiri, K. Shirvanimoghaddam, S. Anwar, J. J. Michels, and K. Asadi, "Hierarchically structured porous

- piezoelectric polymer nanofibers for energy harvesting" *Adv. Sci.*, vol. 7, no. 13, pp. 2000517, Jul. 2020, doi: 10.1002/advs.202000517.
- [11] K. Maeda, I. Fujii, K. Nakashima, G. Fujimoto, K. Suma, T. Sukigara, and S. Wada, "Preparation of barium titanate porous ceramics and their sensor properties," *J. Ceram. Soc. Jpn.*, vol. 121, no. 8, pp. 698-701, Aug. 2013, doi: 10.2109/jcersj2.121.698.
- [12] J. I. Roscow, J. Taylor, and C. R. Bowen, "Manufacture and characterization of porous ferroelectrics for piezoelectric energy harvesting applications" *Ferroelectrics*, vol. 498 no. 1, pp. 40-46, May 2016, doi: 10.1080/00150193.2016.1169154.
- [13] J. I. Roscow, Y. Topolov, C. R. Bowen, J. Taylor, and A. E. Panich, "Understanding the peculiarities of the piezoelectric effect in macro-porous BaTiO<sub>3</sub>," *Sci. Technol. Adv. Mater.*, vol. 17, no. 1, pp. 769–776 Nov. 2016, doi: 10.1080/14686996.2016.1245578.
- [14] S. Karmakar, R.Kiran, V. Singh Chauhan, and R. Vaish, "Effect of porosity on energy harvesting performance of 0.5Ba(Ca<sub>0.8</sub>Zr<sub>0.2</sub>)O<sub>3</sub>– 0.5(Ba<sub>0.7</sub>Ca<sub>0.3</sub>)TiO<sub>3</sub> ceramics: A numerical study," *Energy Technol.*, vol. 8, no. 5, pp. 1901302, May 2020, doi:10.1002/ente.201901302.
- [15] T. Zeng, X. L. Dong, S. T. Chen, and H. Yang, "Processing and piezoelectric properties of porous PZT ceramics," *Ceram. Int.*, vol. 33, no. 3, pp. 395–399, Apr. 2007, doi: 10.1016/j.ceramint.2005.09.022.
- [16] P. C. Lee, Y. L. Hsiao, J. Dutta, R. C. Wang, S. W. Tseng, and C. P. Liu, "Development of porous ZnO thin films for enhancing piezoelectric nanogenerators and force sensors," *Nano Energy*, vol. 82, p. 105702, Apr. 2021, doi: 10.1016/j.nanoen.2020.105702.
- [17] R. Guo, C. A. Wang, and A. K. Yang, "Effects of pore size and orientation on dielectric and piezoelectric properties of 1-3 type porous PZT ceramics," *J. Eur. Ceram. Soc.*, vol. 31, no. 4, pp. 605–609, Nov. 2011, doi: 10.1016/j.jeurceramsoc.2010.10.019.
- [18] Y. Zhang *et al.*, "Understanding the effect of porosity on the polarisation-field response of ferroelectric materials," *Acta Mater.*, vol. 154, pp. 100–112, Aug. 2018, doi: 10.1016/j.actamat.2018.05.007.
- [19] S. Xie *et al.*, "Flexural fracture mechanisms and fatigue behaviors of Bi<sub>4</sub>Ti<sub>3</sub>O<sub>12</sub>-based high-temperature piezoceramics sintered at different temperatures," *Ceram. Int.*, vol. 44, no. 14, pp. 16758–16765, Jun. 2018, doi: 10.1016/j.ceramint.2018.06.107.
- [20] T. Zeng, Q. Lou, Y. Bai, X. Dong, and Y. Wang, "The dielectric breakdown properties of porous PZT95/5 ferroelectric ceramics," *Ferroelectrics*, vol. 478, no.

- 1, pp. 118–126, May 2015, doi: 10.1080/00150193.2015.1011528.
- [21] Y. Zhang, C. R. Bowen, and S. Deville, "Ice-templated poly(vinylidene fluoride) ferroelectrets," *Soft Matter*, vol. 15, no. 5, pp. 825–832, Dec. 2019, doi: 10.1039/c8sm02160k.
- [22] S. Cha *et al.*, "Porous PVDF as effective sonic wave driven nanogenerators," *Nano Lett.*, vol. 11, no. 12, pp. 5142–5147, Dec. 2011, doi: 10.1021/nl202208n.
- [23] K. Choi, S. C. Lee, Y. Liang, K. J. Kim, and H. S. Lee, "Transition from nanorod to nanotube of poly(vinylidene trifluoroethylene) ferroelectric nanofiber," *Macromolecules*, vol. 46, no. 8, pp. 3067–3073, Apr. 2013, doi: 10.1021/ma302679g.
- [24] A. Navid, C. S. Lynch, and L. Pilon, "Purified and porous poly(vinylidene fluoride-trifluoroethylene) thin films for pyroelectric infrared sensing and energy harvesting," *Smart Mater. Struct.*, vol. 19, no. 5, pp. 055006, Mar. 2010, doi: 10.1088/0964-1726/19/5/055006.
- [25] A. Seema, K. R. Dayas, and J. M. Varghese, "PVDF-PZT-5H composites prepared by hot press and tape casting techniques," *J. Appl. Polym. Sci.*, vol. 106, no. 1, pp. 146–151, Oct. 2007, doi: 10.1002/app.26673.
- [26] Y. Mao, P. Zhao, G. McConohy, H. Yang, Y. Tong, and X. Wang, "Sponge-like piezoelectric polymer films for scalable and integratable nanogenerators and self-powered electronic systems," *Adv. Energy Mater.*, vol. 4, no. 7, p. 1301624, Jan. 2014, doi: 10.1002/aenm.201301624.
- [27] Z. Zhang, C. Yao, Y. Yu, Z. Hong, M. Zhi, and X. Wang, "Mesoporous piezoelectric polymer composite films with tunable mechanical modulus for harvesting energy from liquid pressure fluctuation," *Adv. Funct. Mater.*, vol. 26, no. 37, pp. 6760–6765, Oct. 2016, doi: 10.1002/adfm.201602624.
- [28] A. A. Khan *et al.*, "Maximizing piezoelectricity by self-assembled highly porous perovskite-polymer composite films to enable the internet of things," *J. Mater. Chem. A*, vol. 8, no. 27, pp. 13619–13629, Jul. 2020, doi: 10.1039/d0ta03416a.
- [29] M. Mulder, "Phase inversion membranes," in *Encyclopedia of Separation Science*, I.D. Wilson, Ed. Cambridge, MA, USA: Academic Press, pp. 3331–3346, 2000, doi: 10.1016/B0-12-226770-2/05271-6.
- [30] J. Cao, H. Zhang, W. Xu, and X. Li, "Poly(vinylidene fluoride) porous membranes precipitated in water/ethanol dual-coagulation bath: The relationship between morphology and performance in vanadium flow battery," *J. Power Sources*, vol. 249, pp. 84–91, Mar. 2014, doi: 10.1016/j.jpowsour.2013.10.069.
- [31] M. B. Thürmer, P. Poletto, M. Marcolin, J. Duarte, and M. Zeni, "Effect of non-solvents used in the coagulation bath on morphology of PVDF membranes," *Mater.*

- Res., vol. 15, no. 6, pp. 884–890, May 2012, doi: 10.1590/S1516-14392012005000115.
- [32] A. L. Ahmad, W. K. W. Ramli, W. J. N. Fernando, and W. R. W. Daud, "Effect of ethanol concentration in water coagulation bath on pore geometry of PVDF membrane for Membrane Gas Absorption application in CO<sub>2</sub> removal," *Sep. Purif. Technol.*, vol. 88, pp. 11–18, Dec. 2011, doi: 10.1016/j.seppur.2011.11.035.
- [33] S. P. Deshmukh and K. Li, "Effect of ethanol composition in water coagulation bath on morphology of PVDF hollow fibre membranes," *J. Membr. Sci.*, vol. 150, no. 1, pp. 75–85, Nov. 1998, doi: 10.1016/S0376-7388(98)00196-3.
- [34] J. M. Kenney, and S. C. Roth, "Room temperature poling of poly(vinylidene fluoride) with deposited metal electrodes," *J. Res. Natl. Bur. Stand.*, vol. 84, no. 6, pp. 447-453, Nov.- Dec.1979, doi: 10.6028/JRES.084.022.
- [35] S. Qin, X. Zhang, Z. Yu, and F. Zhao, "Polarization study of poly(vinylidene fluoride) films under cyclic electric fields," *Polym. Eng. Sci.*, vol. 60, no. 3, pp. 645–656, Jan. 2020, doi: 10.1002/pen.25323.
- [36] S. H. Shin, Y. H. Kim, M. H. Lee, J. Y. Jung, and J. Nah, "Hemispherically aggregated BaTiO<sub>3</sub> nanoparticle composite thin film for high-performance flexible piezoelectric nanogenerator," *ACS Nano*, vol. 8, no. 3, pp. 2766–2773, Mar. 2014, doi: 10.1021/nn406481k.
- [37] Marian Olszowy, "Piezoelectricity and dielectric properties of PVDF/BaTiO<sub>3</sub> composites," in *Proc. SPIE 3181, Dielect. Relat. Phenom. Mater. Physico-Chem. Spectrom. Investig. Appl.*, Sep. 16-20 1994, doi: 10.1117/12.276252.

Table 3.1: Average film porosity and Young's modulus measurements of PVDF-BaTiO<sub>3</sub> films prepared under varying coagulation bath conditions compared with commercial, non-porous PVDF.

Coagulation bath	Porosity (%)	Y (MPa)
conditions		
DI	64.91 ±0.41	224 ±12.73
DI15E	$63.30 \pm 0.87$	251 ±3.54
DI30E	60.33 ±1.15	310 ±9.90
DI45E	58.20 ±1.45	368 ±2.12
Commercial PVDF	2.5	2000

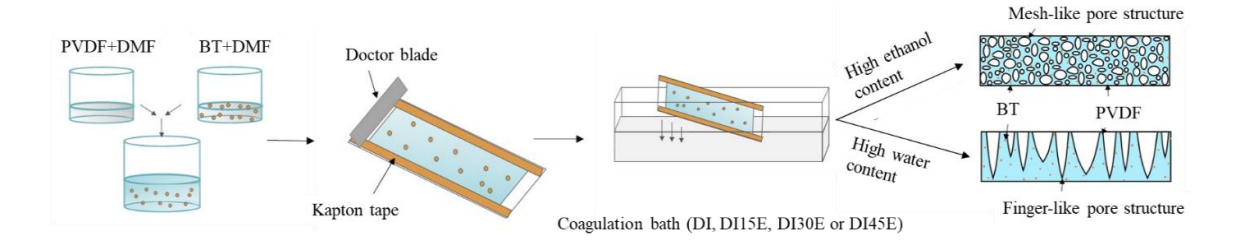


Figure 3.1: Fabrication of porous PVDF-BaTiO<sub>3</sub> composite films via coagulation bath phase inversion. PVDF and BaTiO<sub>3</sub> solutions in DMF are mixed to form a homogeneous composite solution before drop-casting on a glass slide and immersion in a coagulation bath. A transition from finger-like pore structures to mesh-like pores occurs with increasing ethanol content of the coagulation bath.

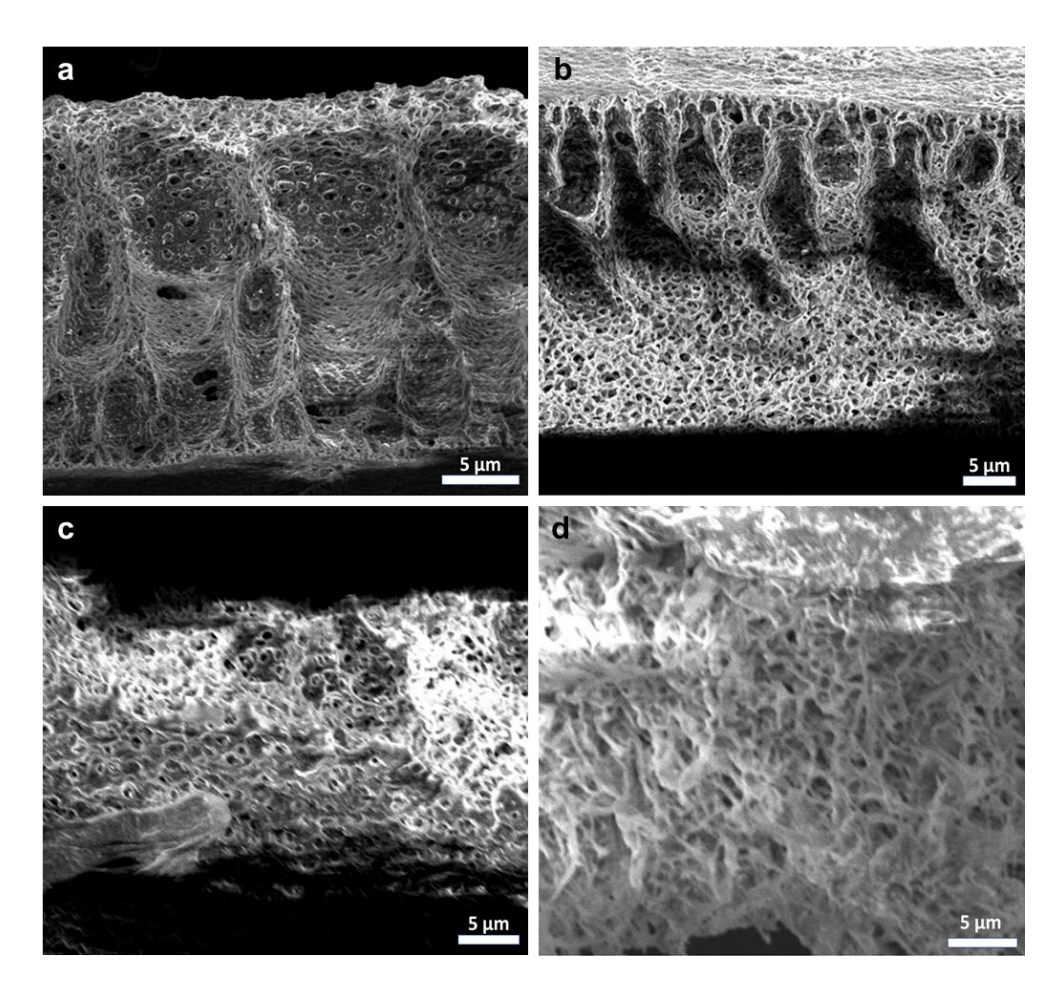


Figure 3.2: Cross-sectional SEM images of PVDF-BaTiO<sub>3</sub> films fabricated in a) DI water bath (DI), b) DI-15% ethanol bath (DI15E), c) DI-30% ethanol bath (DI30E), and d) DI-45% ethanol bath (DI45E).

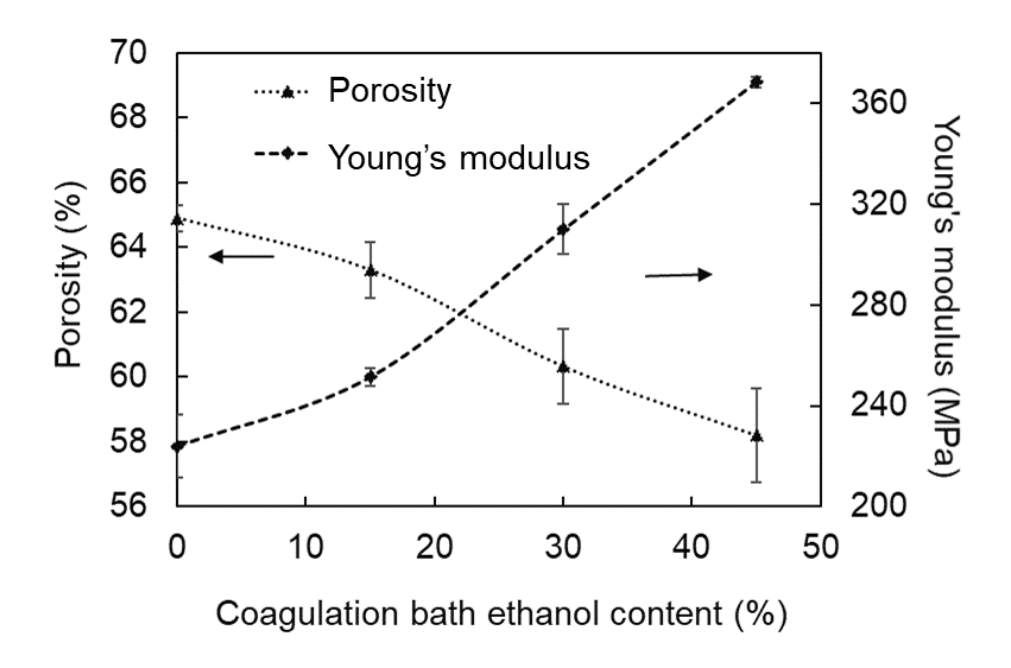


Figure 3.3: Effect of coagulation bath ethanol content on the porosity and Young's modulus of PVDF-BaTiO<sub>3</sub> films. Increasing ethanol content results in decreasing porosity and increasing Young's modulus.

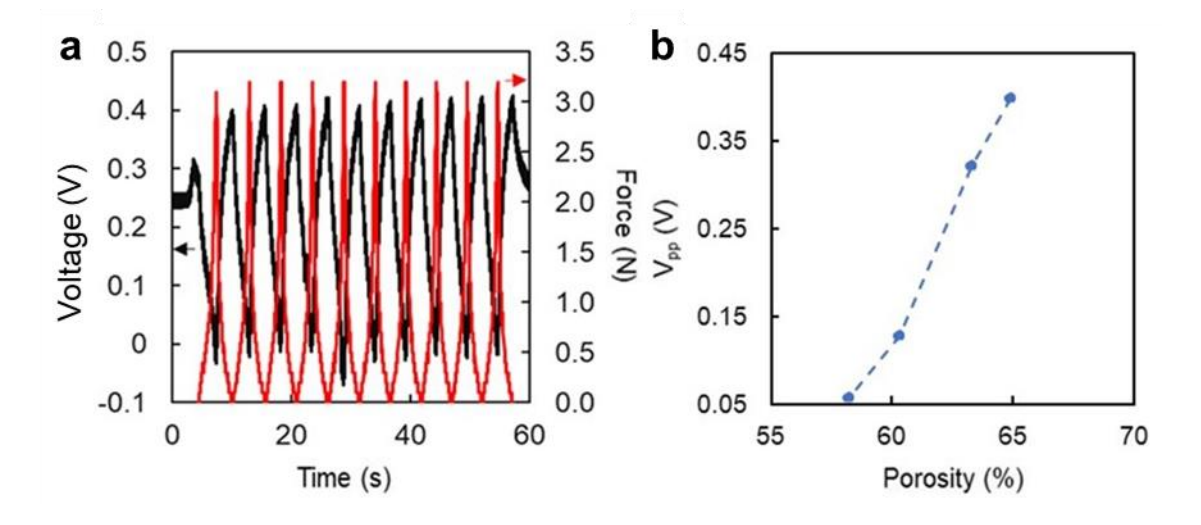


Figure 3.4: a) Piezoelectric voltage response of the DI film under compressive loading. b) Effect of PVDF-BaTiO<sub>3</sub> film porosity on the resulting peak-to-peak voltage response ( $V_{pp}$ ) under 3 N compressive loading.

#### CHAPTER 4

# DESIGN OF HEATED CELLS FOR IN-SITU ABSORPTION AND REFLECTANCE UV-VIS SPECTROELECTROCHEMISTRY

## 4.1 Introduction

SEC is the combination of electrochemistry and spectroscopy measurements which enables simultaneous collection of complementary information involving reduction-oxidation (redox) reactions. SEC can provide a thorough picture of electron transfer processes occurring within an electrochemical cell, including information on structural changes during redox events [1]. SEC methods have been applied in various fields including analytical chemistry, materials science, biophysics, and chemical biology. Ultraviolet-visible (UV-Vis) spectroscopy measures sample absorption or reflectance of light in the UV and visible range. For electrolyte studies, UV-Vis absorption spectroscopy and the Beer-Lambert Law can be used to measure solute concentrations *in-operando*; these concentrations can be correlated with redox reactions using SEC to gain insight into reaction mechanisms and kinetics [2]–[4]. These types of cells use optically transparent electrodes [5]. For *in-situ* characterization of electrode materials, reflectance UV-Vis spectroscopy can provide insight into electrode structure-activity correlations [6] and electrode structure/electronic evolution during cell operation [7].

SEC cell design requirements can vary significantly for different in-situ

studies, necessary to create custom SEC cell designs beyond what is readily available on the market. Temperature control is particularly important for many UV-Vis spectroelectrochemistry experiments. Numerous designs for optically transparent thin-layer electrode (OTTLE) cells [8]–[10] have been proposed and developed, including temperature-controlled cryostated OTTLE cells [11]. In some cases, greater temperature ranges or ramp rates may be required than achievable with commercially-available, temperature-controlled UV-Vis spectrophotometers, and cells using special techniques like externally-circulated fluids have been proposed [5]. In other cases, researchers may not have access to temperature-controlled spectrophotometers, such that the availability of simple, easy-to-replicate cell designs incorporating temperature control is advantageous.

In-operando SEC measurements are of considerable value in the study of lithiumion batteries (LIBs). For example, SEC measurements play a vital role in understanding
formation and composition of passivation layers on electrodes [12]. These layers are
critical for battery performance, aging and safety. To-date, SEC studies of LIBs operating
at elevated temperatures are currently limited. At high temperatures, LIBs experience
problems including: anode solid electrolyte interface degradation, thermal run-away,
electrolyte decomposition, and cathode decomposition [13], [14]. SEC can be leveraged to
investigate alternative electrolytes and electrodes for high-temperature LIBs. Easy-toreplicate cell designs that support high-temperature LIB SEC research are needed for the
continued advancement of this field.

In this work, we present two SEC cell designs for *in-situ* UV-Vis spectroscopy studies of high-temperature LIBs. The first design uses a standard quartz cuvette with a cartridge heater for rapid heating of the electrolyte during transmittance measurements

(Figure 4.1). The design can also be used in reflectance mode using the integrated sphere detector of a UV-Vis spectrophotometer. The second design is a "Conflat"-type [15] disc cell for reflectance mode UV-Vis spectroscopy using the integrated sphere detector. The disc cell achieves rapid heating with an integrated Peltier heating device. Both designs can be easily fabricated for <\$100 (USD) using a combination of off-the-shelf, additively manufactured (*i.e.*, 3D printed), and machined parts. The designs provide complete sealing for use with air- and moisture-sensitive LIB electrolytes outside of an inert atmosphere. This paper details the design and fabrication process for each cell for ease-of-replication by readers. Experimentally measured heating rates and sealing pressures are provided for both designs.

# 4.2 Experimental

All designs were prepared using the computer-aided design software SolidWorks (Dassault Systèmes SE, France). Appendix B Table B.1 and Table B.2 provide a complete bill-of-materials for the cuvette and disc cell designs, respectively. Detailed design drawings for custom 3D-printed and machined parts are provided in Appendix B Figure B.1a-e for the cuvette design; Figure B.2a-d for the disc cell design). All 3D-printed parts were fabricated from acrylonitrile butadiene styrene (ABS) plastic; machined parts were fabricated using mill, lathe, waterjet cutter and drill press tools. A Perkin Elmer Lambda 950 UV-Vis-near infrared (NIR) spectrophotometer was used for testing the fit of cuvette and disc cell designs within the standard holders of a typical UV-Vis instrument.

The temperatures of both cells were controlled using an Arduino Uno along with a MAX31856 Precision Thermocouple to Digital Converter breakout board. The relay

connected to the heaters was controlled by the Arduino based on the thermocouple input. The sealing pressure of each cell was measured by submerging the cell in water, internally pressurizing with helium, and checking for bubbles to identify a leak. For the cuvette cell, the pressure was slowly increased to a maximum of 40 psi with no bubbles observed. The pressure in the disc cell was incremented in 5 psi intervals until bubbles were observed at 30 psi. Repeated chronopotentiometry measurements of both cells were conducted using a Gamry Interface 1000e potentiostat with 60 s charge and discharge cycles. The cells were assembled with graphite electrodes on 316 stainless steel mesh current collectors with 0.5 M Na<sub>2</sub>SO<sub>4</sub> electrolyte and a Celgard separator.

#### 4.3 Results and Discussion

# 4.3.1 Cuvette Cell Design

The cuvette cell design for heated UV-Vis SEC uses a standard 45 mL cuvette to hold the cell components, electrolyte, and heater (Figure 4.1). The cuvette is sized to fit in the holder of a standard UV-Vis spectrophotometer. The lid is custom-designed to provide an air-tight seal for UV-Vis measurements with air- and moisture-sensitive electrolytes. The upper part of the lid consists of an aluminum plate with holes for electrode and heater external connections. Two screws are used to secure the aluminum plate to a 3D-printed (ABS) collar that wraps around the top of the cuvette. A silicone gasket inserted between the plate and the collar seals the lid components together when screwed in place. The lid has two small holes for electrode connections (3 mm diameter) and a larger hole for the cartridge heater (4 mm diameter). These holes may be sealed with putty or other silicone sealant; sealing testing performed here used Loctite Fun-Tak Mounting Putty. During

pressure testing, the cuvette cell held to 40 psi internal cell pressure with no apparent leaks (Table 4.1).

The cuvette design is configured for two-electrode measurements with a holder for a separator placed between the electrodes. If desired, three-electrode measurements can be accommodated by modifying through-hole placement in the lid. In the two-electrode configuration, a 3D-printed frame holds the cathode, anode, and separator together in a sandwich form. Wires extending through the frame supports provide electrical connections to electrodes.

The cuvette cell design uses a 50 W swaged cartridge heater to provide rapid heating of the electrolyte. The heater is inserted into a custom sleeve machined from 316 stainless steel that connects to the underside of the lid (Appendix B Figure B.1b). The sleeve improves the uniformity of electrolyte heating by providing a larger surface area for heat transfer and protects the less corrosion-resistant heater surface (321 stainless steel) from electrolyte exposure. The sleeve has an elliptical opening for the light beam to pass through. The cartridge heater duty cycle is controlled by a digital outlet timer connected to the 120 VAC power input of the heater. Figure 4.1b provides a photograph of a fully-assembled cuvette cell.

The temperature ramp rate of the cell and the final, stabilized temperature can both be controlled by varying the duty cycle of the heater. Figure 4.2a provides a plot of cuvette electrolyte temperature as a function of time for varying heating pulses (2-20 s). Electrolyte temperature was measured without anode/cathode/separator assembly, providing an estimate of maximum ramp rates that can be achieved for pure deionized (DI) water solution. Figure 4.2b plots electrolyte temperature (measured at the center of the cuvette

using a Type K Teflon coated thermocouple) as a function of time for an assembled cell with the cartridge heater energized for 15 s. The starting temperature was 295.4 K. The maximum temperature ramp rate was 0.3 K/s, which was sustained for approximately 40 s. The maximum temperature reached was 308.7 K, and the cell remained stabilized around that temperature for approximately 120 s. Higher temperatures can be reached by modifying the duty cycle of the heater. Figure 4.2c plots electrolyte temperature *vs.* time for an assembled cell with a target temperature of 313 K held for 700 s. Temperature was measured by a thermocouple placed on the metal sleeve adjacent to the heater. The precision of temperature control is limited by the sampling frequency of the MAX31856 breakout board, and the high power of the cartridge heater. Switching to a lower power heater and using a higher frequency thermocouple-to-digital converter are both options for reducing fluctuations when the cell is held at a constant target temperature.

# 4.3.2 Disc Cell Design

The disc cell (Figure 4.3) follows the general design approach of the two-electrode Conflat cell [15]. The cell body is machined from a 1" diameter 316 stainless steel rod (Appendix B Figure B.2a). Stainless steel 316 was chosen for its good chemical resistance over a wide temperature range [16]. Grooved steps inside the cell body allow battery components along with a rubber O-ring to fit in the cell. A 1" (25.4 mm) cell diameter was chosen to: 1) match the approximate beam diameter of the spectrophotometer, 2) fit standard CR2032 disc electrodes, and 3) ensure uniform heating over the cell using a common Peltier heating device. Typical Peltier heating modules are 1.57" (40 mm) in diameter [17]. The cell body can be scaled to larger or smaller diameter, or be made from

a different machinable metal, according to needs. A custom machined polytetrafluoroethylene (PTFE) ring isolates anode and cathode within the cell (Appendix B Figure B.2d). A custom 316 stainless steel 'Q'-shaped ring (Appendix B Figure B.2b) provides an electrical connection to the top electrode, with the cell body providing an electrical connection to the bottom electrode. A machined polyethylene terephthalate glycol (PETG) disc serves as a viewing window for the top electrode. Any machinable UV-transparent sheet (*i.e.*, glass, quartz, polyethylene terephthalate, *etc.*) can be used for the viewing window. Four screws and an O-ring ensure an air-tight seal for the fully-assembled cell. Sealing tests of the disk cell indicated that the cell can withstand 30 psi with no apparent leaks (Table 4.1). In the photograph of a constructed disc cell in Figure 4.3b, a stainless-steel mesh electrode is used as the top electrode, which can be seen through the circular viewing window.

Heating of the disk cell is accomplished using a Peltier device positioned underneath the cell body. Reversal of the Peltier device enables the disc cell design to also provide active cooling during UV-Vis SEC experiments. The duty cycle of the Peltier (operated at 3.4 V) is controlled by an Arduino using a relay. An immersive thermocouple in the cell provides active temperature data to the Arduino, which then holds the heater at the set temperature. Figure 4.3c plots temperature *vs.* time measurements of the Peltier top surface and the inside of the disc cell for a target cell temperature of 333 K. The maximum temperature ramp rate measured inside the disc cell was 0.45 K/s, and the final temperature measured after 300 s was 325 K (slightly below target) (Table 4.1).

# 4.3.2 Supercapacitor and UV-Vis Testing

Cuvette and disc cell electrochemical stability was evaluated using repeated chronopotentiometry measurements of two-electrode cells with symmetric graphite-graphite supercapacitor electrodes. The cells were charged and discharged at 298 K (room temperature) and at 313 K (Appendix B Figure B.3). The results for both cells indicate comparable charge-discharge stability at room temperature and 313 K. Figure 4.4 provides transmittance (Figure 4.4a) and reflectance (Figure 4.4b) spectra in the 300-700 nm wavelength range for the cuvette and disc cell, respectively. UV-Vis spectra were measured without any electrodes or electrolyte in the cell to determine the baseline reflectance or transmittance of the designs.

### 4.4 Conclusion

This chapter shows two easy-to-fabricate, low-cost designs for UV-Vis SEC cells with temperature control and air-tight sealing. The designs are highly adaptable, have good temperature ramp capabilities, and provide a do-it-yourself option for researchers without access to temperature-controlled UV-Vis spectrophotometers. The cells can facilitate pathways to study high-temperature LIBs and gain new insights into the charge-discharge mechanisms of battery materials of interest at elevated temperatures.

#### 4.5 References

- [1] Y. Zhai, Z. Zhu, S. Zhou, C. Zhu, and S. Dong, "Recent advances in spectroelectrochemistry," *Nanoscale*, vol. 10, no. 7, pp. 3089–3111, Jan. 2018, doi: 10.1039/c7nr07803j.
- [2] Q. Yu and S. Ye, "In situ study of oxygen reduction in dimethyl sulfoxide (DMSO) solution: A fundamental study for development of the lithium-oxygen battery," *J. Phys. Chem. C*, vol. 119, no. 22, pp. 12236–12250, Jun. 2015, doi: 10.1021/acs.jpcc.5b03370.
- [3] T. Takashima, K. Ishikawa, and H. Irie, "Detection of intermediate species in oxygen evolution on hematite electrodes using spectroelectrochemical measurements," *J. Phys. Chem. C*, vol. 120, no. 43, pp. 24827–24834, Oct. 2016, doi: 10.1021/acs.jpcc.6b07978.
- [4] O. L. Gribkova, V. A. Kabanova, O. D. Iakobson, and A. A. Nekrasov, "Spectroelectrochemical investigation of electrodeposited polypyrrole complexes with sulfonated polyelectrolytes," *Electrochim. Acta*, vol. 382, p. 138307, Apr. 2021, doi: 10.1016/j.electacta.2021.138307.
- [5] I. S. Zavarine and C. P. Kubiak, "A versatile variable temperature thin layer reflectance spectroelectrochemical cell," *J. Electroanal. Chem.*, vol. 495, no. 2, pp. 106–109, Jan. 2001, doi: 10.1016/S0022-0728(00)00394-6.
- [6] S. Wahl, S. M. El-Refaei, P. Amsalem, A. G. Buzanich, N. Koch, and N. Pinna, "Operando diffuse reflectance UV-vis spectroelectrochemistry for investigating oxygen evolution electrocatalysts," *Catal. Sci. Technol.*, vol. 10, no. 2, pp. 517–528, Dec. 2019, doi: 10.1039/c9cy02329a.
- [7] M. Kobielusz, A. Nitta, W. MacYk, and B. Ohtani, "Combined spectroscopic methods of determination of density of electronic states: Comparative analysis of diffuse reflectance spectroelectrochemistry and reversed double-beam photoacoustic spectroscopy," *J. Phys. Chem. Lett.*, vol. 12, no. 11, pp. 3019–3025, Mar. 2021, doi: 10.1021/acs.jpclett.1c00262.
- [8] D. Martín-Yerga, A. Pérez-Junquera, D. Hernández-Santos, and P. Fanjul-Bolado, "Time-resolved luminescence spectroelectrochemistry at screen-printed electrodes: following the redox-dependent fluorescence of [Ru(bpy)<sub>3</sub>]<sup>2+</sup>," *Anal. Chem.*, vol. 89, no. 20, pp. 10649–10654, Sep. 2017, doi: 10.1021/acs.analchem.7b01734.
- [9] M. J. Simone, W. R. Heineman, and G. P. Kreishman, "Long optical path electrochemical cell for absorption or fluorescence spectrometers," *Anal. Chem.*, vol. 54, no. 11, pp. 2382–2384, Nov.1982, doi: 10.1021/ac00250a058.
- [10] R. A. Wilson, T. S. Pinyayev, N. Membreno, and W. R. Heineman, "Rapid prototyped optically transparent thin-layer electrode holder for spectroelectrochemistry in bench-top spectrophotometers," *Electroanalysis*, vol. 22,

- no. 19, pp. 2162–2166, Oct. 2010, doi: 10.1002/elan.201000267.
- [11] F. Hartl, H. Luyten, H. A. Nieuwenhuis, and G. C. Schoemaker, "Versatile cryostated optically transparent thin-layer electrochemical (OTTLE) cell for variable-temperature UV-vis/IR spectroelectrochemical studies," *Appl. Spectrosc.*, vol. 48, no. 12, pp. 1522–1528, Dec. 1994, doi: 10.1366/0003702944027787.
- [12] A. J. Cowan and L. J. Hardwick, "Advanced spectroelectrochemical techniques to study electrode interfaces within lithium-ion and lithium-oxygen batteries," *Annu. Rev. Anal. Chem.*, vol. 12, pp. 323–346, Jun. 2019, doi: 10.1146/annurev-anchem-061318-115303.
- [13] D. R. Wright, N. Garcia-Araez, and J. R. Owen, "Review on high temperature secondary Li-ion batteries," *Energy Procedia*, vol. 151, pp. 174–181, Oct. 2018, doi: 10.1016/j.egypro.2018.09.044.
- [14] J. Zhang, L. Su, Z. Li, Y. Sun, and N. Wu, "The evolution of lithium-ion cell thermal safety with aging examined in a battery testing calorimeter," *Batteries*, vol. 2, no. 2, pp. 1–9, Apr. 2016, doi: 10.3390/batteries2020012.
- [15] K. Periyapperuma, T. T. Tran, S. Trussler, D. Ioboni, and M. N. Obrovac, "Conflat two and three electrode electrochemical cells," *J. Electrochem. Soc.*, vol. 161, no. 14, pp. A2182, Oct. 2014, doi: 10.1149/2.0721414jes.
- [16] Tameson, "Stainless steel 304 and 316 The differences," *Tameson.com*, 2020. https://tameson.com/stainless-steel-304-and-316.html (accessed Nov. 15, 2021).
- [17] Custom Thermoelectric, "History." Customthermoelectric.com https://customthermoelectric.com/tech-info/te-encyclopedia/history.html (accessed Nov. 15, 2021).

Table 4.1: Sealing pressure and temperature test results for cuvette and disc cell designs.

Test parameter	Cuvette cell	Disc cell
Sealing pressure achieved (psi)	> 40	30
Maximum temperature ramp rate for target temperature range (K/s)	0.3	0.67
Target and achieved stabilized cell	Target: 313	Target: 333
temperatures (K)	Achieved:	Achieved: 325
	313 ± 5	

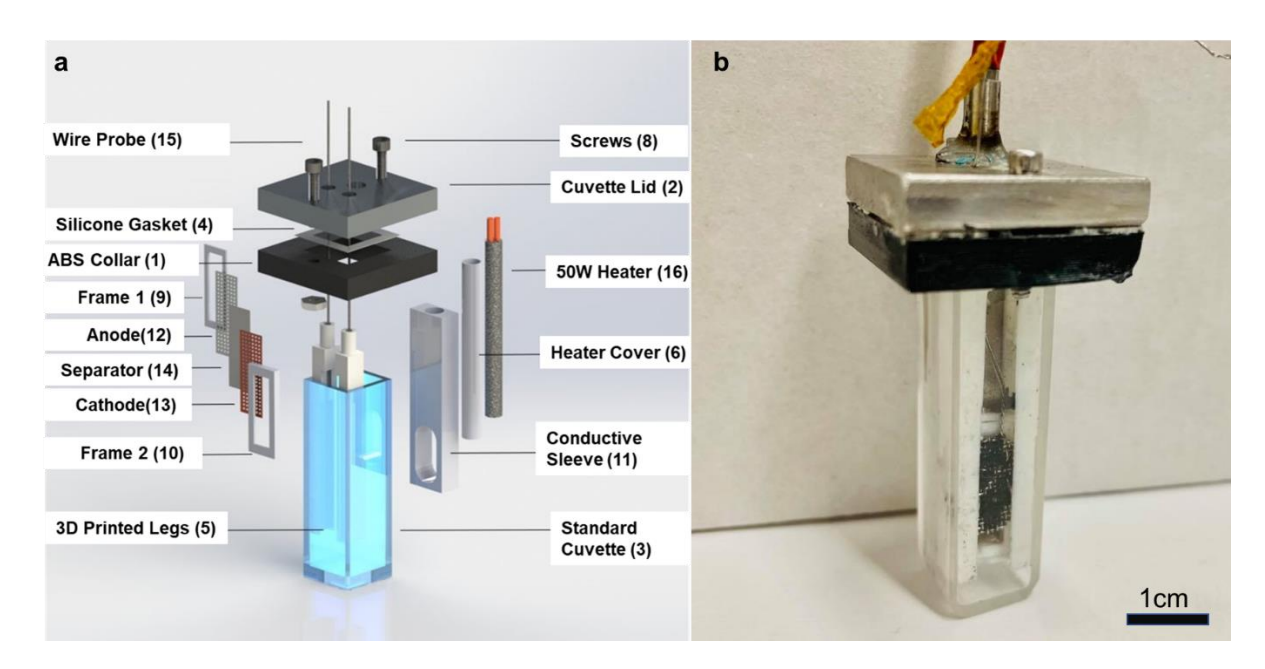


Figure 4.1: Cuvette cell design. a) CAD rendering showing an exploded view of cuvette cell components with numbers correspond to the bill-of-materials provided in Appendix B Table B.1. b) Photograph of an assembled cuvette cell.

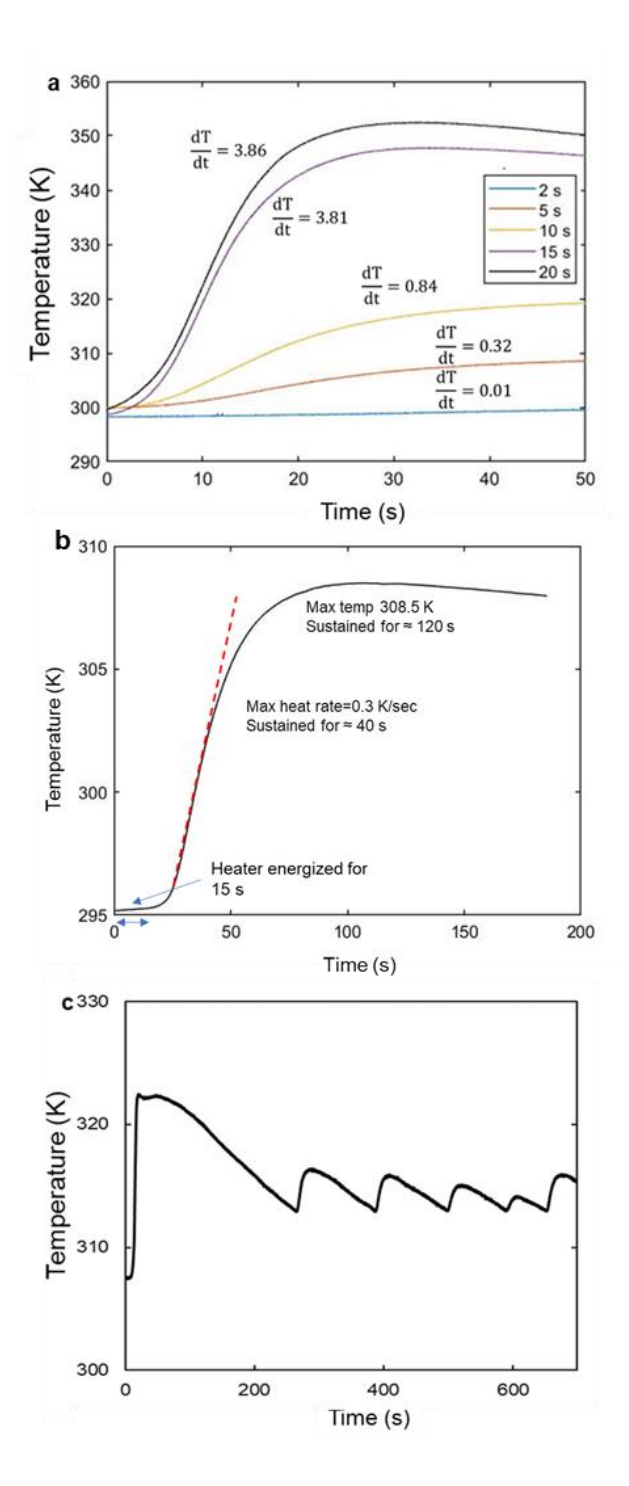


Figure 4.2: Cuvette cell heating rates and maximum temperatures reached for various heating times. a) Cuvette temperatures measured with pure DI water in the cuvette (no cell components). Legend indicates cartridge heating times for each curve. b) Cuvette temperatures measured with an assembled cell with heating applied for 15 s. c) Cell temperature stabilized around a target temperature of 313 K for 700 s.

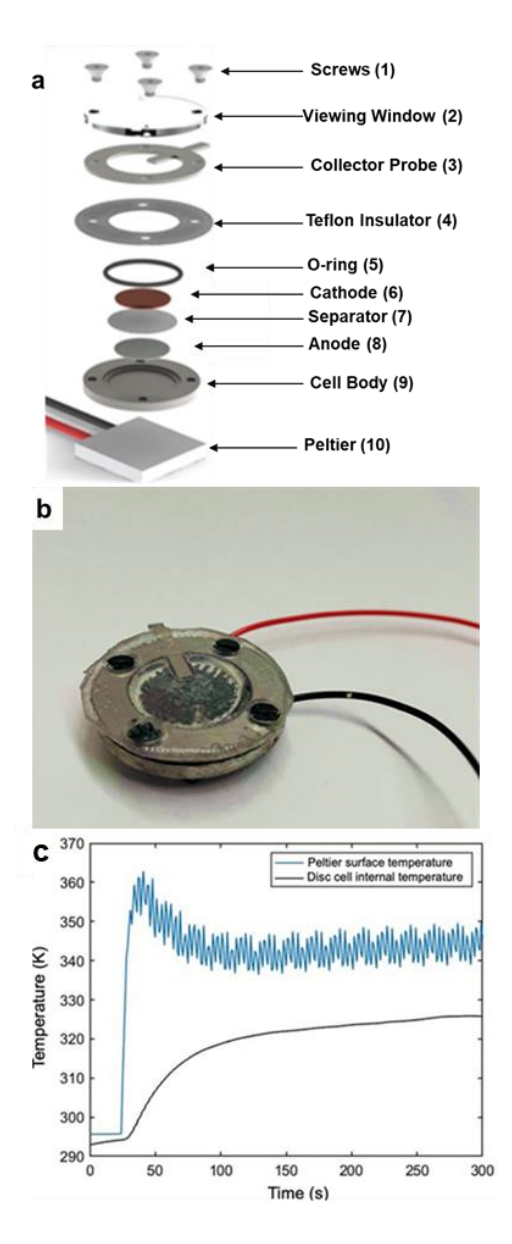


Figure 4.3: Disc cell design. a) CAD rendering showing an exploded view of disc cell components with numbers corresponding to the bill-of-materials provided in Appendix B Table B.2. b) Photograph of an assembled disc cell. c) Disc cell heating profile for a target internal temperature of 333 K. Peltier device surface temperature is modulated to create a rapid rise in disc cell internal temperature that stabilized slightly below the target temperature range.

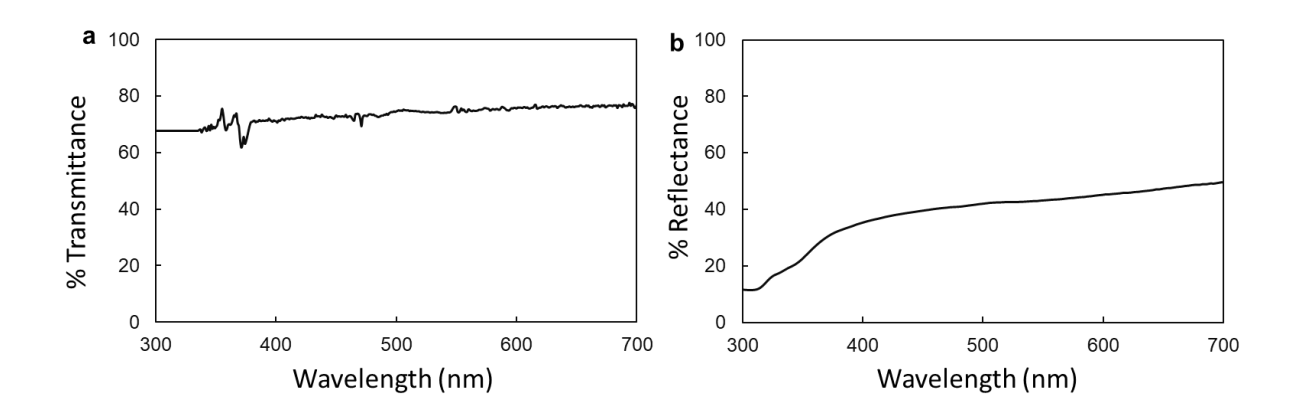


Figure 4.4: a) % Transmittance of the cuvette cell and b) % reflectance of the disc cell without electrodes or electrolyte in the 300-700 nm wavelength range.

#### CHAPTER 5

# HYBRIDIZATION OF THERMAL ENERGY HARVESTING IN A PYROELECTROCHEMICAL CELL

## 5.1 Introduction

Energy harvesting can facilitate powering large-scale wireless sensor networks for modern technology. An energy harvesting system typically has a rechargeable battery or supercapacitor where the harvested energy is stored. Typically, the harvested energy (i.e., mechanical, light, thermal) is converted to electrical energy, then conditioned via auxiliary circuits. The resulting electrical energy is stored as chemical energy in a battery or supercapacitor. Recently the hybridization of the energy generation and energy storage functions in a single device have garnered much attention. Wang et al. have studied piezoelectric self-charging power cells in which they replaced traditional polyethylene (PE) electrochemical separators with piezoelectric PVDF thin film separators [1], [2]. When mechanically stressed, the PVDF film generates an electric field which works as the driving force for ions to charge the cell. Using self-sustaining energy harvesting systems to power these sensor networks for Internet of Things (IoT) can eliminate the need for battery-enabled power and minimize cost and maintenance work needed.

Pyroelectric materials naturally have net unidirectional polarization in the absence of an electric field. Under thermal excitation, pyroelectric materials undergo a change in

polarization due to a change in the thermal vibration of the electric dipoles. Here we propose a pyroelectrochemical cell (PEC) that couples a pyroelectric energy harvester and an electrochemical cell to achieve energy harvesting and storage within a single device. In a PEC, the separator of the electrochemical cell is replaced by a porous pyroelectric film. When the pyroelectric film experiences a temperature change in time, the film generates an electric field which acts as a driving force for the cations and anions in an electrochemical cell to migrate in opposite directions. We hypothesize that a PEC can be charged by heating or cooling with the proper dipole orientation of the pyroelectric film. In this chapter, the surfaces of the pyroelectric film on the positive and negative end of the dipoles will be referred to as positive and negative sides, respectively. Figure 5.1 illustrates the charging mechanism of the PEC with heating. The electrochemical separator is replaced by a porous pyroelectric thin film (Figure 5.1a). Figure 5.1b illustrated the cell under equilibrium temperature. The solvated ions in the electrolyte along with the polarized separator are in charge equilibrium. When the cell is heated, a pyroelectric field is generated across the separator (Figure 5.1c). The pyroelectric field causes a charge imbalance inside the cell, which results in the migration of cations in the direction of the electric field. The polarized separator is placed so that the cations migrate to the anode, and anions migrate to the cathode during a heating cycle. In a supercapacitor, charge separation in the electrochemical double layer increases the open circuit potential (OCP) of the cell.

This work aims to provide the first proof-of-concept demonstration of a PEC device. We have selected porous PVDF as the pyroelectric separator material. PVDF is mechanically flexible, electrochemically inert, and easy to fabricate as a porous thin film, making it an ideal material for a supercapacitor separator. To further enhance the

pyroelectric properties of the PVDF separator, we have incorporated BaTiO<sub>3</sub> ceramic nanoparticles into the film to create a polymer-ceramic composite. The ceramic nanoparticles are themselves electroactive and help form electroactive phases in the PVDF polymer network during PVDF film casting by providing nucleation sites for β-phase PVDF [3], [4]. The ionic conductivity and chemical stability of the porous PVDF-BaTiO<sub>3</sub> is tested via cyclic voltammetry (CV) and electrochemical impedance spectroscopy (EIS) to verify the effective separator functionality of the pyroelectric film. We present two- and three-electrode cells to test the charging-discharging capability of the PEC with temperature change. To test the self-charging properties of the cell, a controlled positive temperature ramp is applied, and the corresponding OCP is measured. The effect of the temperature ramp on the charge state of the cell with and without a pyroelectric separator is compared to identify OCP changes arising from the pyroelectric effect vs. cell temperature change. The possibility of the integrated cell has been demonstrated through at least three repetitions on two- and three-electrode cells, and the stored energy per cycle has been quantified.

### 5.2. Methods

#### 5.2.1 Materials

PVDF powder (average MW~534,000 g/mol) and dimethylformamide (DMF) from MilliporeSigma were used for film synthesis. Both materials were used as received. BaTiO₃ particles were purchased from Stanford Advanced Materials (300-700 nm particle size, tetragonal structure). Graphite powder (<45 μm, ≥99.99% trace metals basis) and carbon black (SuperP Conductive, 99+% (metals basis)) were purchased from,

MilliporeSigma and Alfa Aesar respectively. Sodium sulfate (ACS reagent, ≥99.%, anhydrous, granular) was purchased from MilliporeSigma and used as purchased. Stainless steel (22 μm thick), copper sheets (75 μm thick) were purchased from McMaster Carr. Graphite-coated copper foils (LIB anode -double-layer CMS graphite coated on copper foil (241 mm length x 2mm width x 9 μm thickness)) were purchased from MTI. Cartridge and Peltier heaters were purchased from Walmart (Swaged Cartridge heater, 5W) and Digi-key (Peltier Module 9.5W @ 5°C 4 A 15°C, 15x15 mm²).

#### 5.2.2 Pyroelectric Separator Fabrication and Characterization

Porous PVDF-BaTiO<sub>3</sub> composite films were fabricated via the phase inversion method [5], [6] using a room temperature DI water coagulation bath. A homogeneous slurry of PVDF-BaTiO<sub>3</sub> (8/2% wt/wt%) was coated onto a glass substrate which was then immersed into the coagulation bath for 2 minutes. Kapton tape was used for a reference to provide consistent film thicknesses during casting. The solvent- non-solvent demixing precipitated the polymer, forming the porous films. The films were dried at 6°C (1 hour) and annealed at 9°C (5 hours) before poling. An electric field of 15 MV/m was applied for 6 minutes (3 minutes at 12°C and 3 minutes during cooling) to pole the films. The porosity of the films was measured using a solvent uptake method [5]. The films were soaked in 1-butanol for one hour. Porosity was then calculated using Equation 5.1:

$$\varepsilon = \frac{\frac{m_b}{\rho_b}}{\frac{m_p}{\rho_p} + \frac{m_b}{\rho_b}} \tag{5.1}$$

where  $\rho_p$ ,  $\rho_b$  are the densities of PVDF and 1-butanol, respectively, and  $m_p$ ,  $m_b$  are the mass of the dry film and film after soaking, respectively.

The pyroelectric coefficient of poled PVDF-BaTiO<sub>3</sub> films was measured using a temperature ramp technique [7]. The films were metalized by sputtering 1 nm Ti and 5 nm Au to create electrical contacts. A metalized film of known surface area (~2 cm<sup>2</sup>) was mounted onto a silicon wafer (for known thermal conductivity). Using an IR lamp, the temperature was increased from room temperature (28.2°C) to 31°C at a ramp rate of .8°C/s. A type-K surface thermocouple was used to measure the temperature of the samples. The voltage signal was collected from the sample through a charge amplifier circuit (Figure 5.2). The pyroelectric coefficient was then calculated from the voltage and temperature using the Equation 5.2:

$$I = \frac{V_o}{R} = pA \frac{dT}{dt} \tag{5.2}$$

where I is the measured current,  $V_o$  is the op-amp output voltage, R is the feedback resistance in Figure 5.2, p is the pyroelectric coefficient, A is the sample surface area, and  $\frac{dT}{dt}$  is the temperature ramp rate.

#### 5.2.3 Electrochemical Testing

PEC OCP measurements were conducted using a three-electrode cell and a twoelectrode cell (modified Conflat cell [8]). The three-electrode cell used a 30mL beaker with a 3D printed lid (ABS- Acrylonitrile butadiene styrene) to hold the electrodes and 50 W cartridge heater in place (Figure 5.3a). The separator was held between the electrodes using a 3D printed frame (Figure 5.3b). The working electrode was graphite on a stainless-steel current collector. Graphite electrodes were prepared by mixing graphite, Super P (conductive additive), and PVDF (binder) into a homogeneous slurry in DMF at an 80:10:10 wt/wt ratio. 10 mg of slurry was coated onto a 316 stainless steel plate (dimension) and dried in the oven for 24 hours at 65°C. Cu foil was used as the counter electrode. The working and counter electrodes with the separator slid into the legs of the 3D printed lid (Figure 5.3b). The reference electrode was Ag/AgCl with 1 M KCl, and the electrolyte was 0.5 M Na<sub>2</sub>SO<sub>4</sub>. The cartridge heater was energized for heating times ranging from 6-8 s using a digital outlet timer (Nearpow, model: 250h/40h/80h/20h/160h) connected to the 120 VAC power input.

A custom-made miniature Conflat cell was used for the two-electrode cell. The two electrodes were graphite-coated Cu foil (15 mm diameter, 90 µm thickness), with 0.5 M Na<sub>2</sub>SO<sub>4</sub> as the electrolyte. The stacked electrodes and separator were placed inside the disc cell with an O- ring. The disc cell was machined from a stainless-steel rod of 1" diameter (Figure 5.3c). The cell was enclosed with a stainless-steel lid with a polymer gasket in between the top and bottom halves of the cell (Figure 5.3c). This cell was heated using a Peltier heating device. The heater covered the entire bottom surface of the cell to ensure uniform heating. The heater was powered using a DC voltage supply set at 3.4 V and manually turned on and off after 20 or 30 s.

The three-electrode beaker and the Conflat cells were characterized for temperature using a type-K surface and immersion thermocouple. Cell temperature was recorded using the National Instruments data acquisition unit (NI-9219). After each heating cycle, two-and three-electrode cells returned to room temperature without active cooling. A Gamry Interface 1000E potentiostat was used for all electrochemical testing. Along with the poled PVDF- BaTiO<sub>3</sub> films, unpoled PVDF-BaTiO<sub>3</sub> and cellulose (Celgard 3501) separators were used for characterizing the cells for thermal effect.

#### 5.3 Results

The primary objective of this research was to demonstrate and characterize the concept of an integrated PEC. The pyroelectric coefficient and porosity of the pyroelectric separator were characterized. The focus in the electrochemical characterization was to understand the impact of an internal electric field on the ion migration and resultant change in the electric double layer of the electrode. The symmetric supercapacitor and the three-electrode configuration cells were characterized for their charge storage capability. Furthermore, experiments were performed to understand the difference between pyroelectric and thermal effects occurring in the cell.

# 5.3.1 Separator Pyroelectric Effect

PVDF-BaTiO<sub>3</sub> film porosity was 64.91 %  $\pm 0.41$  % across three batches of the 50  $\mu$ m  $\pm 5$  % films. The pyroelectric coefficients of the films were measured using a temperature ramp technique using a charge amplifier circuit (Figure 5.2). The measured pyroelectric current, *I* in Figure 5.2, was used to calculate the pyroelectric coefficient, *p*, in Equation 5.2. Figure 5.4a plots the measured voltage and temperature for a sample. The initial voltage is non-zero owing to the internal polarization of the film. The pyroelectric coefficient ranged from 60-70  $\mu$ Cm<sup>-2</sup>K<sup>-1</sup> measured on three sets of films. Pure non-porous PVDF films have reported a pyroelectric coefficient of 30  $\mu$ Cm<sup>-2</sup>K<sup>-1</sup>. Figure 5.4b shows the cross-sectional image of the film. The finger-like structures in the film formed through phase inversion create channels for ion migration.

# 5.3.2 Separator Electrochemical Testing

The porous electroactive film needs to be chemically stable and have through pores enabling free ion migration. The film should impose little to no resistance to the flow of ions. Three-electrode CV measurements of symmetric graphite supercapacitor electrodes with a porous PVDF- BaTiO<sub>3</sub> separator indicate that separator is electrochemically stable over the 50-500 mV voltage range tested. The CV data showed chemical stability in the electrolyte and repeatability over the cycles. Figure 5.5a shows the 2<sup>nd</sup>, 5<sup>th</sup> and 10<sup>th</sup> cycle of the CV test. EIS measurements of the two-electrode Conflat cell with pyroelectric and Celgard separators are presented in Figure 5.5b. The EIS data shows lower series resistance compared to the commercial Celgard separator. This indicates that the PVDF-BaTiO<sub>3</sub> film provides sufficient through-channels for ion migration to act as a separator in an electrochemical cell. Consistency of EIS data measured with both orientations of the pyroelectric film suggests the PVDF-BaTiO<sub>3</sub> separators have similar ion interactions and electrochemical parameters (i.e., resistance, capacitance) irrespective of the pyroelectric orientation. Also, the EIS data indicates a semi- infinite / unrestricted diffusion process in the PEC which implies the diffusion flux is dominant in these cells.

Supercapacitor cells were tested using pyroelectric separators and a commercial Celgard separator as a control. Figure 5.6a shows the voltage change in the two-electrode cell (change from the starting OCP) when subjected to heating. Three cells were replicated to test for repeatability of the PEC cells. All the cells had the same components (electrode, electrolyte, current collectors, etc.) except the separators. The pyroelectric separators were placed such that the positive side is facing the anode of the cell. All three PECs showed charging of the cell with heating. The cells were heated using the Peltier heating device for

30 s at a ramp rate of 0.264 ° C/s. The voltage changed about 5 mV and stabilized at a higher energy state. In contrast, the Celgard separator (red line) showed a transient change in the voltage. Although the voltage initially fluctuated, it stabilized at the original voltage within 300 s (Figure 5.6a). Cell temperature returned to room temperature in 8 minutes. However, OCP measurements indicate that PECs remain charged for at least an hour (tested), as shown in Figure 5.6b. More tests are required to understand the cell operation over longer periods of time.

To understand and further explore the effect of the pyroelectric electric field on the cell, the working electrode was tested in the three-electrode configuration. The OCP of the cell is overlayed with temperature against time (Figure 5.6c). The positive side of the separator faced the working electrode in this configuration. Temperature was increased at 1° C/s to 30° C. Electrode potential increased from 114 mV to 136 mV. The plot shows the electrode holds its charged state as the cell temperature gradually decreases to room temperature while the magnitude of the generated pyroelectric field slowly went down due to cooling. The data suggests that chemical equilibrium is attained at the double layer of the working electrode due to the generated electric field in the separator, and the cell remains at the new equilibrium.

Unlike the Celgard separator, the direction of PVDF- BaTiO<sub>3</sub> separators' dipoles has an impact on the charging-discharging of the cell. The pyroelectric separators were flipped and tested on both sides to understand the process (Figure 5.7). When the positive side of the separator faced the anode, heating charged the cell. In contrast, the cell discharged and attained chemical equilibrium at lower OCP when the negative side of the separator faced the anode. In this orientation, there was a transient voltage increase in the

positive direction which can be attributed to the initial random movement of surface charges under thermal excitation.

According to the theory of pyroelectric materials, the pyroelectric current generated is directly proportional to the temperature ramp rate (Equation 5.1). The PEC was tested for different ramp rates in the three-electrode cell to determine if this proportionality appeared in the voltage response of the PEC. The cartridge heater in the cell had been energized for 6- and 8-s, respectively. The 6- and 8-s energization times correspond to 0.23 and 1.04°C/s, respectively. The energization times have been limited to 8 s to avoid localized overheating of the electrolyte and risk irreversible damage to the cell. The results (shown in Figure 5.8a) show that the increase in the potential for the 8-s energization is nearly three times larger than for the 6-s energization after 3000 s. The small dip in potential is hypothesized to be a transient thermal effect on the cell. The generated pyroelectric field potential then initiates the migration of ions which increases the cell potential. This electric field slowly diminishes to zero due to cooling while the electrode potential slowly stabilizes.

The electrode was heated repeatedly in the three-electrode cell. Figure 5.8b shows the change in OCP of the electrode with each heating step. The data suggests the double layer of charge builds up more charge with heating cycles in the PEC. The electrode potential increased from 104mV to 134 mV with three heating cycles. This suggests applied thermal energy in each heating cycle is converted and stored as chemical energy in the cell. The heating cycles can be repeated to attain a larger voltage change and therefore higher energy storage.

Table 5.1 shows the resultant ramp rate, generated voltage, and energy stored per

heating cycle. The energy was calculated using the following equations:

$$E_{out} = \frac{1}{2}C(V_2^2 - V_1^2) \tag{5.3}$$

where C is the calculated capacitance of the cell from the CV curve,  $V_2$  and  $V_1$  are the potential of the electrode before and after the heating cycle. The PEC converts thermal energy to pyroelectric-electrostatic energy (i.e. the voltage and charge that would be stored in the pyroelectric material if not integrated into the PEC) to electrochemical energy. The efficiency of the pyroelectric-electrostatic to electrochemical energy conversion was calculated from the following equations:

$$I = pA \frac{dT}{dt}$$

Generated charge, Q = pAdT

$$V = \frac{Q}{C} = \frac{pAdT}{\frac{\epsilon A}{h}} = \frac{pAdTh}{\epsilon A}$$

The pyroelectric-electrostatic energy is then

$$E_{in} = \frac{1}{2}QV = \frac{1}{2}. \ pAdT.\frac{pAdTh}{\epsilon A}$$
 (5.4)

$$\eta_{p \to e} = \frac{E_{out}}{E_{in}} = \frac{\frac{1}{2}C(V_2^2 - V_1^2)}{\frac{1}{2} \cdot pAdT \cdot \frac{pAdTh}{\epsilon A}}$$
 (5.5)

where,  $\epsilon$  is the dielectric permittivity, C is the capacitance, and h is the thickness of the separator. As shown in Table 5.1, this efficiency for the two tests run is 44.6% and 68%. As this is a fundamentally new device, there are no benchmarks to which these efficiencies can be compared, but efficiencies on the order of 50% seem reasonable. The stored electrochemical energy per cycle was 9.74  $\mu$ J/cm<sup>2</sup>. They pyroelectricity of the separators is almost entirely due to the BaTiO particles, not the PVDF. With improved poling such that both phases are strongly pyroelectric and system optimization, significant

improvements to the generated energy per thermal cycle are possible. However, even 10  $\mu$ J per thermal cycle may be enough to support a single measurement for a wireless sensor. The efficiency of the thermal energy to pyroelectric-electrostatic energy can be calculated from the following equation:

$$\eta_{th \to p} = \frac{\frac{1}{2} \cdot pAdT. \frac{pAdTh}{\epsilon A}}{msdT}$$
 (5.6)

where, s is the specific heat of the porous composite film, m is the mass of the separator, dT is the temperature difference. The input thermal energy is considered only to the separator not the whole cell for this calculation. Moreover, the assumption here is that the PVDF and BaTiO<sub>3</sub> in the film are both contributing to the pyroelectric effect. The efficiency is calculated to be 0.05%. The Carnot efficiency for the same temperature difference is 2.3%. With better pyroelectric coefficient and optimization, the thermal to pyroelectric-electrostatic efficiency can be increased.

Figure 5.9 shows the electrode potential decay over time. The data shows the charge holds up for 2 hours and then slowly discharges in 4-5 hours. The gradual increase in potential for two hours can be attributed to the slow decrease in pyroelectric field with cooling. After the electric field is diminished to zero, the electrode potential starts to discharge through leakage current.

## 5.4 Theory of PEC Operation

A temperature change will change the OCP of an electrochemical cell in the absence of a pyroelectric material. In the case of an electrochemical double-layer capacitor, the change in OCP will be due to changes in electrode double-layer structure upon heating or cooling. A PEC will experience this "thermal effect" in addition to effects arising from

the change in polarization of the pyroelectric separator. In formulating a "theory of operation" of the PEC, we first consider the change in the structure of the electric double layer due to the thermal effect alone. This theory is based on experimental OCP measurements of cells containing a Celgard separator. We then consider the change in OCP of the PEC as a combination of thermal effects and pyroelectric polarization.

# 5.4.1 Thermal Effect (Celgard Separator)

According to Stern theory, an electrochemical double layer can be approximated as a Stern layer and a diffuse layer [8], [9] (Figure 5.10a). The Stern layer consists of solvated ions electrostatically bound to the electrode surface. Beyond the Stern layer, the remaining compensating ions make up the diffuse layer [9]. Ions in the diffuse layer are subject to electrostatic attraction and thermal agitation. Figure 5.10a shows the negative electrode where solvated cations form the Stern and diffuse layer. The cell temperature change impacts the double layer charges in the supercapacitor. Figure 5.10b shows the thermal effect on the cell with a non-pyroelectric separator when subjected to a 25°C temperature change in 30 s. We hypothesize that increased thermal energy causes ions in the diffuse layer to migrate deeper into the electrolyte in the neutral region when the temperature increases, thus increasing the interface's diffuse layer length. As a result, the equivalent capacitance of the Stern and diffuse layers decreases. As an immediate response, the OCP of the cell increases to maintain the charge on the interface. The subsequent decrease in OCP may be explained by considering non-ideal faradaic reactions that could occur when cell temperature increases. With increasing temperature, we hypothesize that the rate of non-ideal faradic reactions on the electrode increases. According to the Nernst equation,

this corresponds to a decrease in OCP, as observed in Figure 5.10b. As the temperature slowly stabilizes to room temperature again, we see the open-circuit voltage settling at equilibrium. While room temperature CV measurements of the PEC (Figure 5.5a) show ideal electrochemical double layer capacitance without the presence of faradaic reactions, it is likely that non-ideal faradaic effects occur at elevated cell temperatures. This hypothesis needs to be tested further in conjunction with multiphysics and thermal modeling.

# 5.4.2 Combined Thermal and Pyroelectric

Effect (PVDF- BaTiO<sub>3</sub> Separator)

In the PEC, thermal effects occur simultaneously with the pyroelectric effect. Figure 5.11 illustrates the cell's charging mechanism under the pyroelectric effect in accordance with actual results. The negative side of the separator faces the electrode (Figure 5.11a). With increasing temperature, the polarization of the separator decreases due to increased thermal vibration. This decrease in polarization generates an electric field in the separator (Figure 5.11b). The generated pyroelectric field creates an electrostatic force gradient that acts on the ions inside the cell. The positive and negative charges (ions) move in opposite directions to attain charge neutrality screening the internal electric field. If the separator is placed such that the positive ions move in the direction of the anode and negative ions toward the cathode, we hypothesize that more solvated ions appear at the electrode-electrolyte interface at each electrode increasing the OCP of the cell (Figure 5.11c). The opposite phenomenon occurs when the pyroelectric separator orientation is reversed (Figure 5.7). When the positive side faces the cathode, a decrease in polarization

of the separator will cause positive ions to move from anode to cathode, thus decreasing the OCP. The electrostatic charge separation prohibits the ions from moving back after the temperature reaches its equilibrium value (Figure 5.11d).

#### 5.5 Conclusion

This work provides a first proof-of-concept demonstration of the direct conversion of thermal energy to stored electrochemical energy *via* a pyroelectric separator. Experimental results indicate that a temperature change can be used to induce a net change in the OCP of a PEC. The change in OCP of the cell is proportional to the temperature ramp rate, as expected for a voltage change arising from the pyroelectric effect. Reversing the orientation of the poled pyroelectric separator in the cell discharges the cell upon heating, also as expected for results arising from the pyroelectric effect. Successive heating cycles result in successive step increases in OCP, suggesting that this mechanism could be used to charge the cell to higher voltages.

The experimental results demonstrated in this chapter support the theoretical hypothesis of the charging mechanism of the PEC. Understanding the impact of an internal pyroelectric field on the ion migration and double-layer charge is essential for future optimization of the PEC. This needs further thermal and multiphysics modeling to support the hypothesis and experimental results presented here. The symmetric supercapacitor cell provides a new pathway for powering low voltage/low power devices in remote sensing technologies. This device can provide power to portable electronics, environmental sensors without the need for bulky energy storage devices and circuits [10], [11]. The system

requires optimization for application-specific use. The thermal to pyroelectric conversion is limited by the pyroelectric coefficient of the film and the temperature ramp rate.

#### 5.6 References

- [1] A. Ramadoss, B. Saravanakumar, S. W. Lee, Y. S. Kim, S. J. Kim, and Z. L. Wang, "Piezoelectric-driven self-charging supercapacitor power cell," *ACS Nano*, vol. 9, no. 4, pp. 4337-4345, Mar. 2015, doi: 10.1021/acsnano.5b00759.
- [2] J. H. Lee, J. Kim, T. Y. Kim, M. S. Al Hossain, S. W. Kim, and J. H. Kim, "All-in-one energy harvesting and storage devices," *J. Mater. Chem. A.*, no. 21, pp. 7983-7999, Apr. 2016, doi: 10.1039/c6ta01229a.
- [3] A. D. Hussein, R. S. Sabry, O. Abdul Azeez Dakhil, and R. Bagherzadeh, "Effect of adding BaTiO<sub>3</sub> to PVDF as nano generator," *J. Phys. Conf. Ser.*, vol. 1294, no. 2, pp. 022012, Oct. 2019, doi: 10.1088/1742-6596/1294/2/022012.
- [4] M. Sharma, J. K. Quamara, and A. Gaur, "Behaviour of multiphase PVDF in (1–x)PVDF/(x)BaTiO<sub>3</sub> nanocomposite films: Structural, optical, dielectric and ferroelectric properties," *J. Mater. Sci. Mater. Electron.*, vol. 29, no. 13, pp. 10875–10884, Mar. 2018, doi: 10.1007/s10854-018-9163-4.
- [5] A. L. Ahmad, W. K. W. Ramli, W. J. N. Fernando, and W. R. W. Daud, "Effect of ethanol concentration in water coagulation bath on pore geometry of PVDF membrane for Membrane Gas Absorption application in CO<sub>2</sub> removal," *Sep. Purif. Technol.*, vol. 88, pp. 11–18, 2012, doi: 10.1016/j.seppur.2011.11.035.
- [6] M. B. Thürmer, P. Poletto, M. Marcolin, J. Duarte, and M. Zeni, "Effect of non-solvents used in the coagulation bath on morphology of PVDF membranes," *Mater. Res.*, vol. 15, no. 6, pp. 884–890, Nov. 2012, doi: 10.1590/S1516-14392012005000115.
- [7] I. Lubomirsky and O. Stafsudd, "Invited review article: Practical guide for pyroelectric measurements," *Rev. Sci. Instrum.*, vol. 83, no. 5, p. 051101, May 2012, doi: 10.1063/1.4709621.
- [8] Department of Chemical Engineering and Biotechnology, "The electrical double layer," University of Cambridge, https://www.ceb.cam.ac.uk/research/groups/rg-eme/Edu/the-electrical-doublelayer (accessed Nov. 08, 2021).
- [9] Thiruvalluvar University, "Theories of structure of double layer," https://www.tvu.edu.in/wp-content/uploads/2019/10/Structure-of-double-layer-Models.pdf, pp. 1–12 (accessed Feb. 01, 2022).
- [10] H. Sun, Y. Zhang, J. Zhang, X. Sun, and H. Peng, "Energy harvesting and storage in 1D devices," *Nat. Rev. Mater.*, vol. 2, no. 6, pp. 1–12, Apr. 2017, doi: 10.1038/natrevmats.2017.23.
- [11] Y. Zi *et al.*, "Effective energy storage from a triboelectric nanogenerator," *Nat. Commun.*, vol. 7, no. 1, pp. 1–8, Mar. 2016, doi: 10.1038/ncomms10987.

Table 5.1: Energization time, ramp rate,	voltage, and energy	generated per cycle in the
three-electrode cell.		

Energization	Calculated	Voltage	Energy stored	Efficiency
Time (sec)	ramp	Generated	per cycle	(Pyroelectric to
	Rate (°C/s)	(mV)	$(\mu J/cm^2)$	electrochemical)
				%
6	0.231	8	2.9	68
8	1.04	22	9.74	44.6

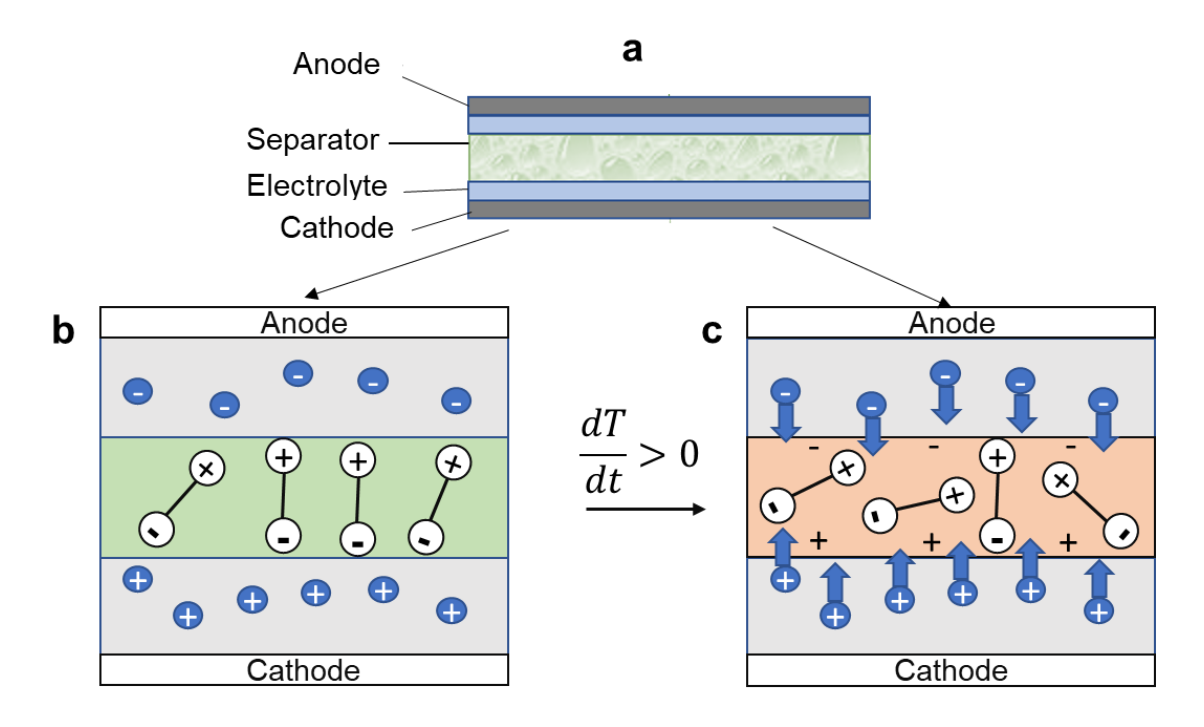


Figure 5.1: a) In a PEC, the conventional separator is replaced by a pyroelectric film, which charges under the influence of a temperature change with time (dT/dt). b) Solvated cations and anions surrounding the polarized pyroelectric separator in thermal equilibrium (dT/dt=0). c) An electric field generates across the film due to decreasing material polarization, which initiates ion migration in the cell.

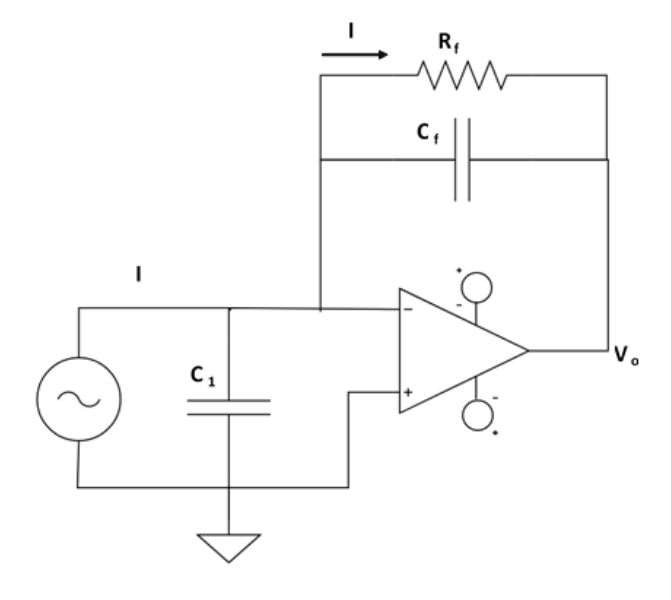


Figure 5.2: Charge amplifier circuit for measuring the generated pyroelectric current.

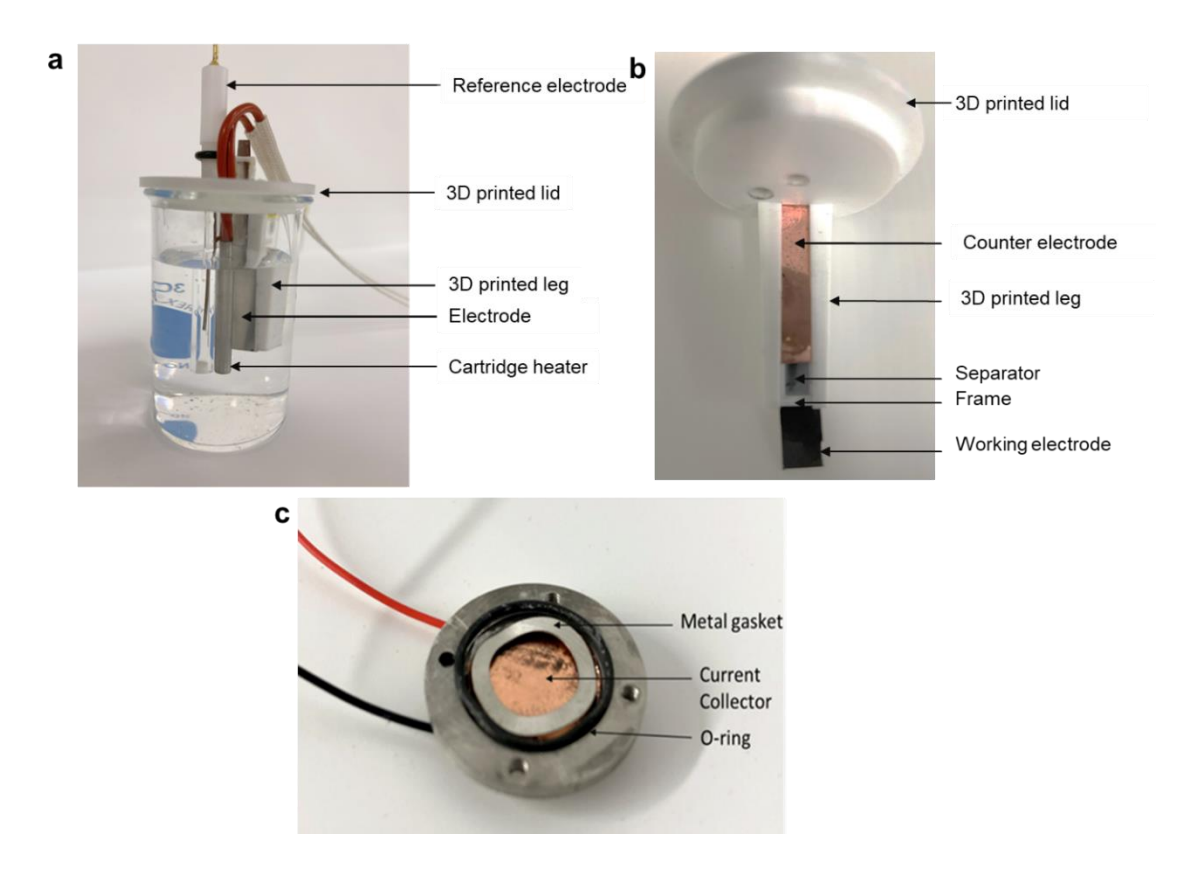


Figure 5.3: Cell configuration. a) three-electrode cell in a beaker, b) the electrodes and the separator in the 3D printed leg of the three-electrode cell, b) two-electrode conflat cell with all the components on top of a Peltier heating device.

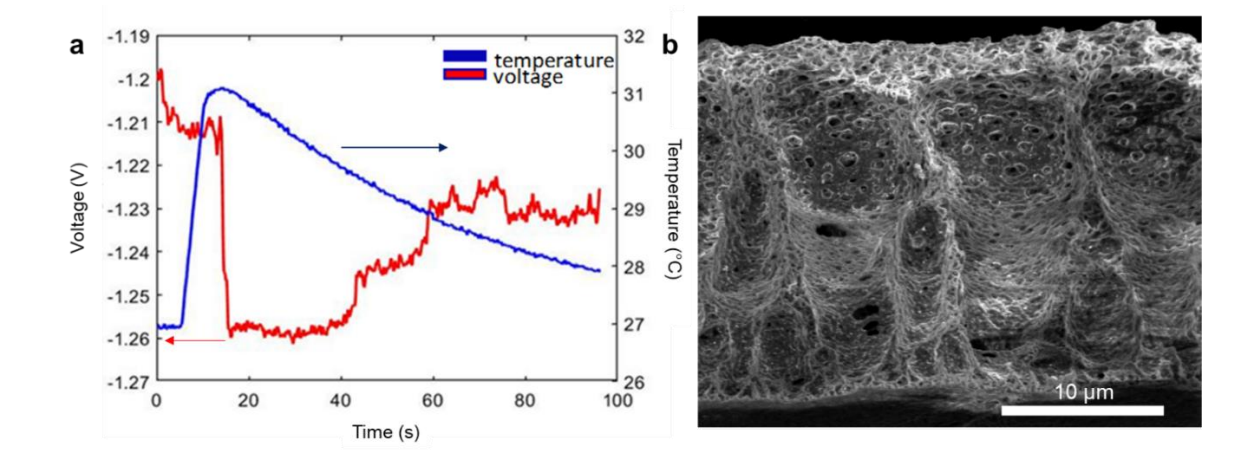


Figure 5.4: Separator characterization (a) Measured voltage and temperature signals through a temperature ramp technique, (c) SEM image showing the PVDF- BaTiO<sub>3</sub> film through pores across the separator cross-section.

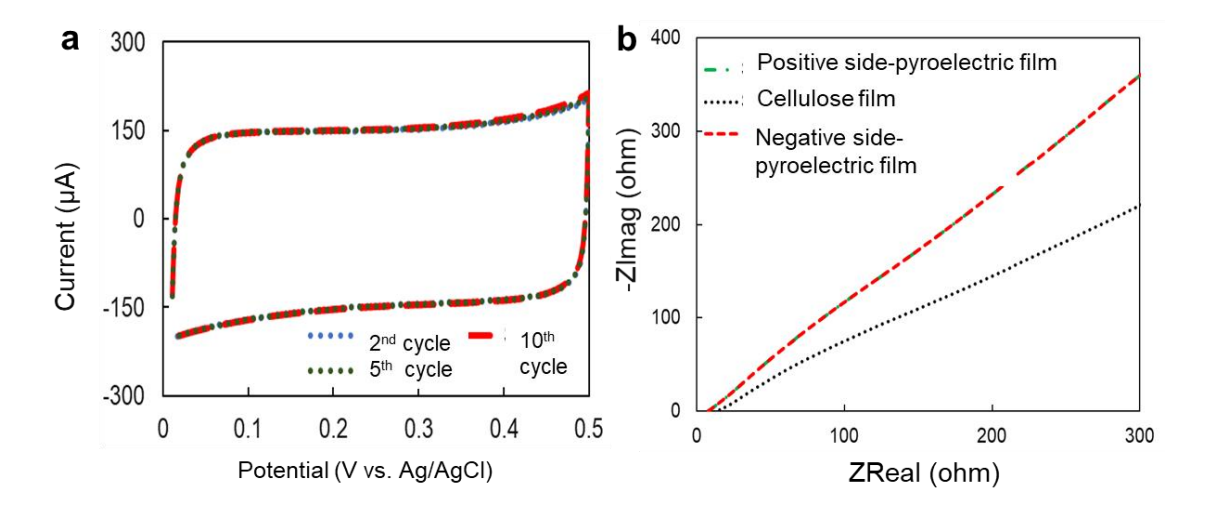


Figure 5.5: Electrochemical characterization. a) 2<sup>nd</sup>, 5<sup>th</sup>, and 10<sup>th</sup> cycle of a CV test in the three-electrode cell. b) Nyquist plot of the EIS on the two-electrode cell for pyroelectric and Celgard separators shows the PVDF-BaTiO<sub>3</sub> films have good ion migration channels.

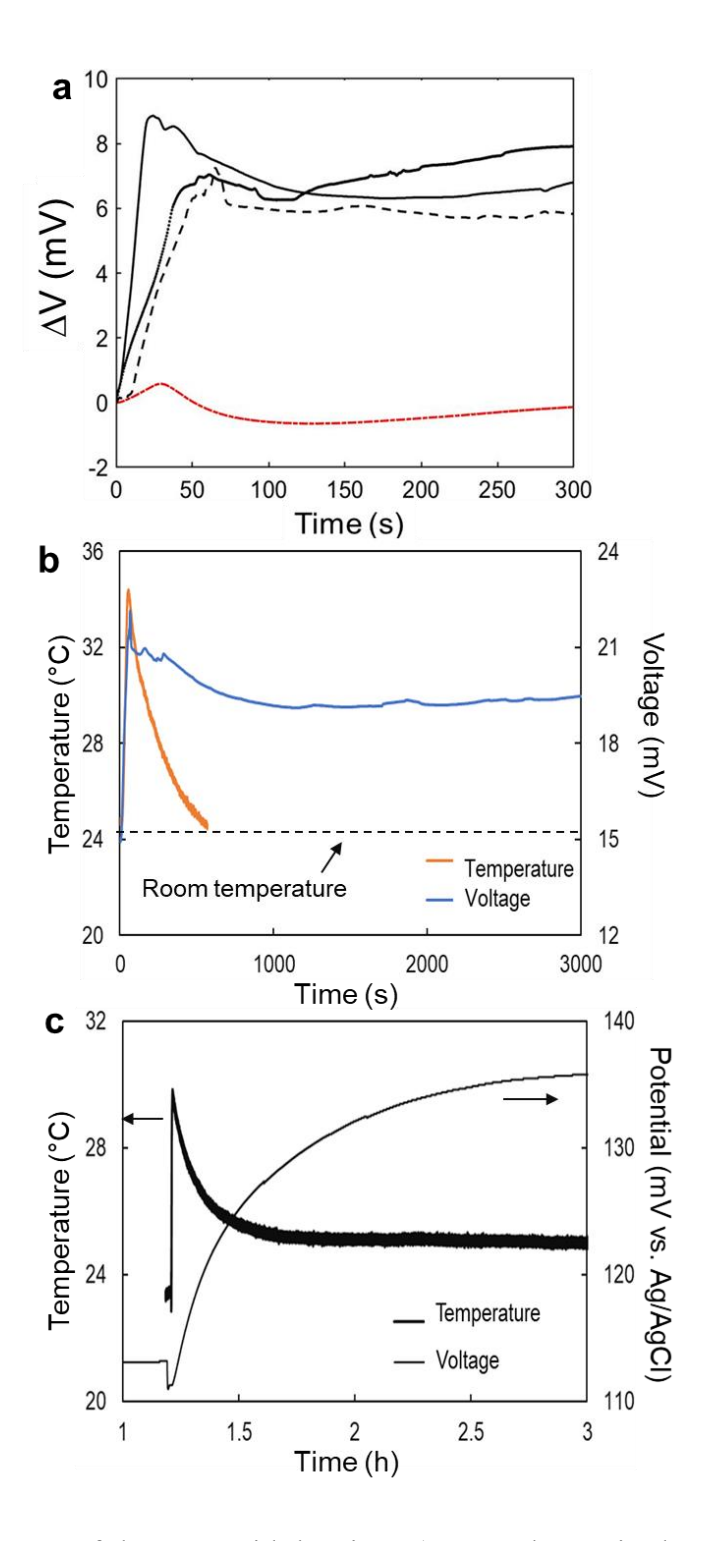


Figure 5.6: OCP response of the PEC with heating. a) OCP change in the two-electrode cell (three replicates) with increased temperature with pyroelectric separators and a Celgard separator (red line). The PEC data is from three different pyroelectric separator samples with the same electrode, electrolyte, and current collectors. b) Time vs. temperature and OCP in the two-electrode cell c) Time vs. temperature and electrode potential in the three-electrode cell showing the changed energy state of the working electrode.

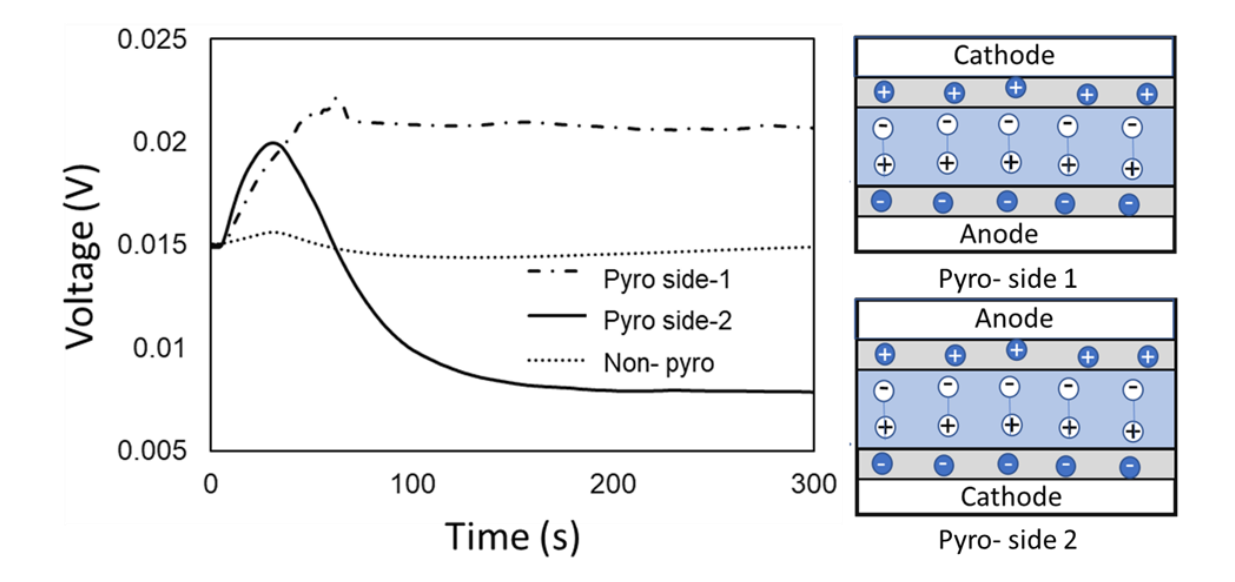


Figure 5.7: Comparison of pyroelectric and thermal effect on Celgard separator and pyroelectric films (side 1 and side 2). Flipping polarization changes the direction of voltage change for the pyroelectric films.

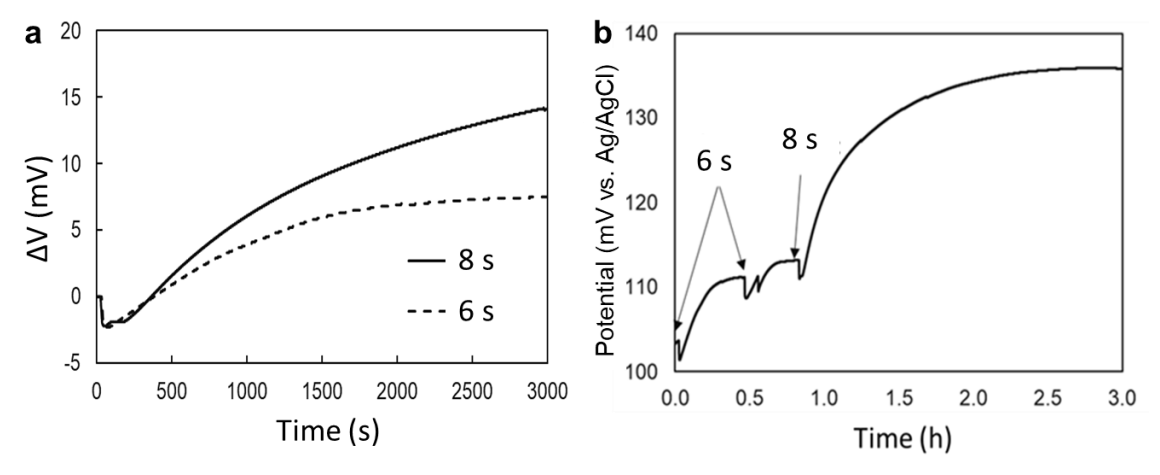


Figure 5.8: Varying energization times. a) Voltage changes with different energization times repeated on the same cell. b) Three heating cycles show an increasing change in the electrode's potential vs. a reference electrode.

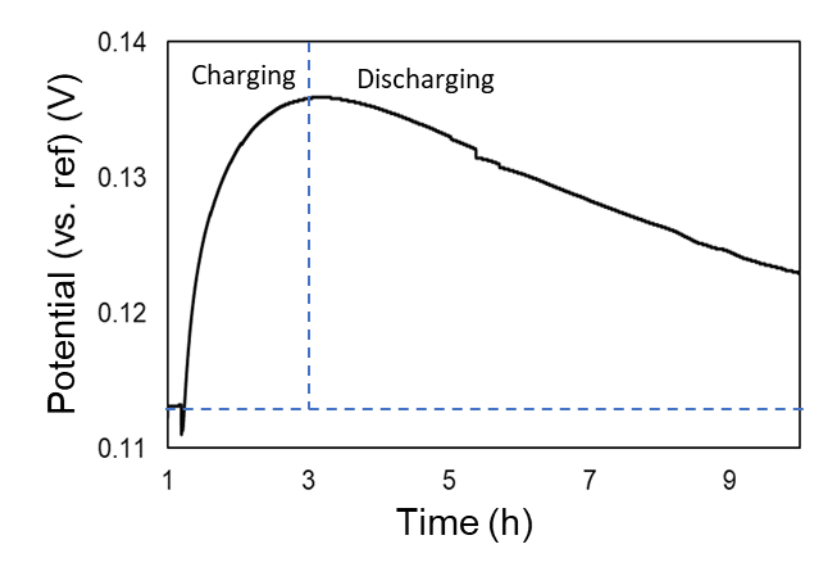


Figure 5.9: The electrode potential over 9 hours to understand the self-discharging of the cell after charging through the pyroelectric effect. The cell shows slow discharging 2 hours after the heating cycle.

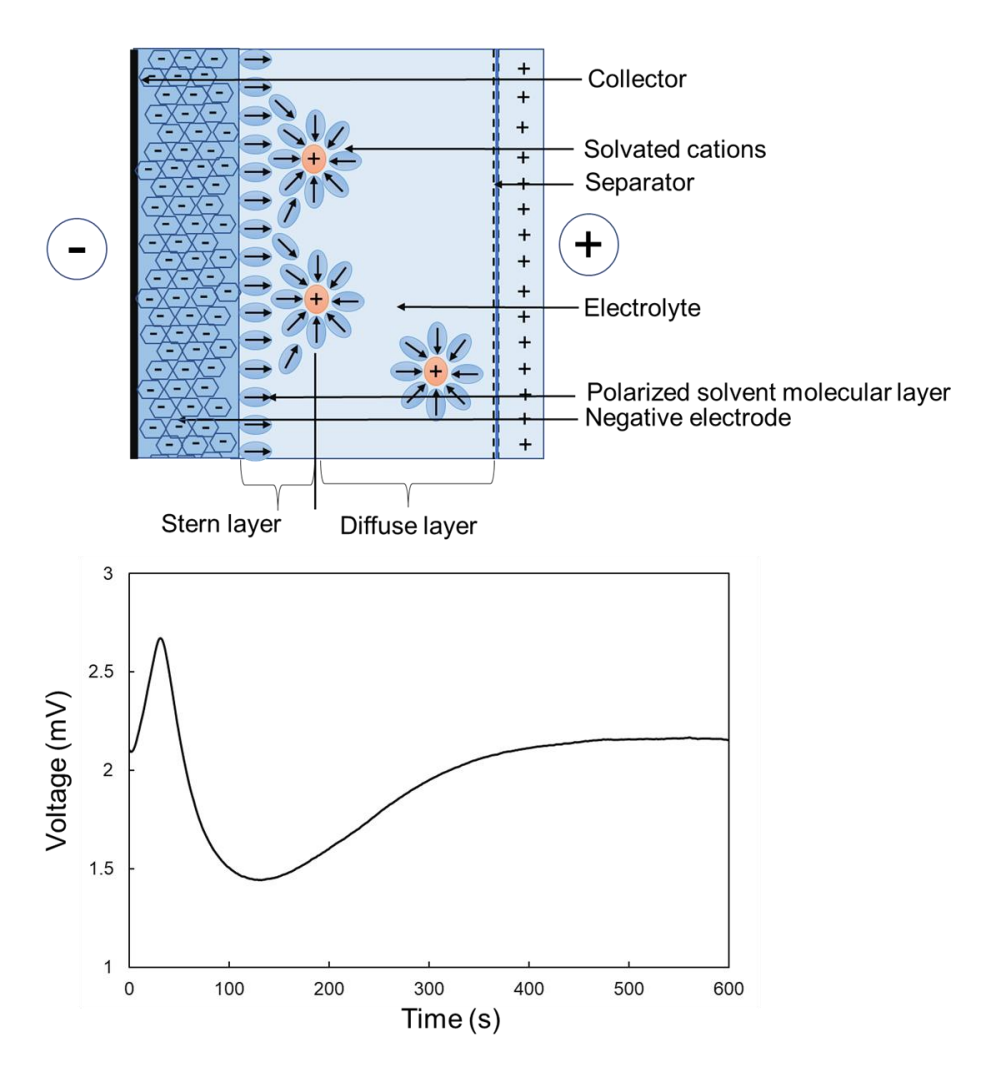


Figure 5.10: Double layer of charge at electrochemical cell electrode and electrolyte interface and b) resultant cell voltage-change due to thermal effect.

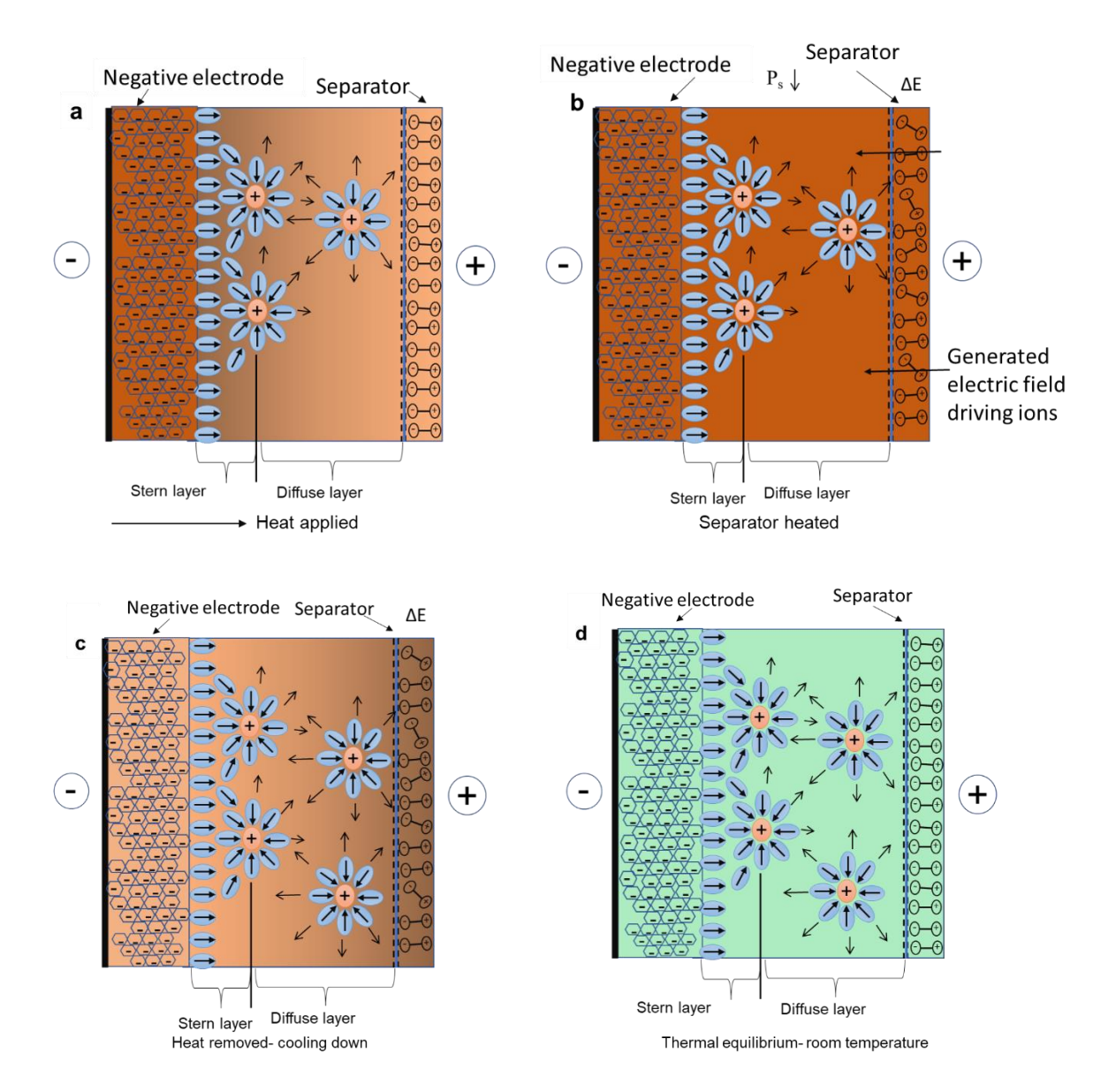


Figure 5.11: Electrode-electrolyte interface with pyroelectric separator. a) temperature applied slowly progresses towards the separator. b) and c) the separator generates an internal electric field which causes charge imbalance in the cell, the ions migrate to screen the electric field and insert themselves in the electric double layer. d) after the thermal excitation is removed, the temperature drops down to equilibrium, the dipoles inside the pyroelectric material stabilize, the polarization reaches equilibrium, the cations and anions in the electrolyte are stabilized in the double layer at a different energy state.

#### CHAPTER 6

#### **CONCLUSION**

This research is motivated by the drive towards modern wireless monitoring technology. Energy harvesting can be the answer to powering large numbers of sensors/nodes in an Internet of Things (IoT) network. This dissertation has demonstrated a pathway to power low-power devices to facilitate modern technology. The focus of this research revolved around the demonstration of novel PEC cells. From synthesizing a porous composite film with good pyroelectric properties to incorporating it in the PEC, we have filled-in some knowledge gaps in available research.

In Chapter 2, we have studied the efficacy of stretching a PVDF- BaTiO<sub>3</sub> composite film to increase the electroactive phase content in the films for the first time. The results here indicate a promising shift of PVDF  $\alpha$  and  $\gamma$  phases to  $\beta$  phase upon stretching of PVDF-BaTiO<sub>3</sub> composite films. The study highlights a tradeoff between mechanical elasticity and  $\beta$  phase content of the composite films for application-specific usage. Previously the inclusion of ceramic fillers and stretching of pure PVDF films have been studied independently. The optimal filler ratio to enable mechanical drawing of composite films to maximize  $\beta$  phase content has been overlooked. This study has presented a guideline for designing composite structures with optimal filler ratio to maximize  $\beta$  phase content.

In Chapter 3, we have investigated the morphology of porous PVDF-BaTiO<sub>3</sub> composite films. We have presented a simple fabrication approach with controlled pore structures through phase inversion. The impact of pore structures on force transfer between polymer matrix and electroactive ceramic fillers has been studied through optical and mechanical characterization. Previous works have investigated the impact of porosity on electroactive performance. This work has studied how the morphology in the composite structure impacts the resultant electroactive performance. The different pore structures result in significantly varying electroactive performance, despite similar porosity in the films. This study can guide the design of porous ceramic-polymer structures for many applications in the future.

We have designed and demonstrated two easy-to-fabricate, highly adaptable structures to facilitate *in-operando* SEC study. This is crucial for studying high-temperature battery materials, charge-discharge mechanisms, and temperature effects on the cell in a controlled way. Chapter 4 presents the construction and design details with all necessary parts for any researcher to develop their own, facilitating the research of next-generation battery materials.

Chapter 5 demonstrates the basic functionality of the PEC. Most energy harvesting systems require an external reservoir (battery or supercapacitor) to store the harvested energy. Also, no integrated system has been demonstrated for intermittent thermal energy harvesting. Unlike thermoelectric devices, the PEC systems do not require maintaining spatial temperature gradient or external power sources. There is room for device optimization with existing options for electrode and electrolytes for the broad temperature range. The electrochemical characterization explains the practicality of using a porous

composite film in place of a Celgard separator. The study investigates the effect of temperature fluctuations on the electrode-electrolyte interface for the first time. Thermoelectric and other thermal energy harvesters have low efficiency and the tradeoff between thermal conductivity and ionic conductivity of the electrolytes limit further development of these cells with existing materials. In PEC, higher thermal conductivity is desired to gain higher temperature ramp across the separator. The self-charging capability of the demonstrated PEC shows a pathway to harvesting the thermal energy from temperature fluctuations. The PEC shows 22mV voltage change with  $8\mu J$  energy in a single heating cycle ( $\Delta T = 8$  °C). With optimization this device can generate enough energy to power periodic measurement cycles of a remote sensor. Thus, this integrated device can provide a novel approach to meet the increasing energy demand for modern technology.

### 6.1 Future Work

The efficiency and energy calculations show that the pyroelectric material limits the device's performance. The efficiency for the thermal to pyroelectric energy is <0.1%. The key parameters influencing this efficiency are: film surface area, pyroelectric coefficient of the film and, temperature ramp rate. The device optimization must be done considering the operating environmental conditions. The temperature ramp rate during heating and cooling must be calibrated so that the cooling rate is significantly smaller than the heating rate and thus, cooling does not discharge the stored charge during the heating cycle.

The film surface area is constricted as we want to keep the device size small.

Although larger surface area increases the pyroelectric current, larger devices will increase

system loss and leakage resistance. The temperature ramp rate is also limited in the environment. The pyroelectric coefficient of the film can be improved by taking extra measures.

### 6.1.1 Corona Poling

PVDF poling requires a high electric field compared to BaTiO<sub>3</sub> particles. Literature states PVDF is poled under 20-100 MV/m at 90°C for efficient poling [1], [2]. In contrast, BaTiO<sub>3</sub> particles are optimally poled under <30 MV/m at 120°C [3]. The electric field is highly dependent on the BaTiO<sub>3</sub> particle size. Moreover, the porous structure of our films limits the maximum field that can be applied to the films. Corona poling can be an effective alternative that removes the constraint of breakdown in the film. It can confirm consistent poling of both PVDF and BaTiO<sub>3</sub>.

### 6.1.2 Coupling SMA to the Composite Film

Shape Memory Alloy (SMA) physically reverses deformation due to temperature-induced stress. Gusarov et al. presented a novel energy harvester coupling SMA ribbons on the surface of a PVDF thin film to increase the energy density of the harvester [4]. Our group is currently building a model for the coupled energy harvester using Nitinol SMA ribbons and PVDF- BaTiO<sub>3</sub> composite film. Figure 6.1 shows the induced stress concentration on the film due to a change in temperature of the SMA ribbon. The ring tries to reverse the deformation to its original shape resulting in a tensile force on the attached film. Thus, a temperature change will cause SMA ribbons to cause piezoelectric voltage generation in the PVDF- BaTiO<sub>3</sub> films complementing the pyroelectric energy generation.

Another important consideration for future cells is to reduce the leakage current of the cell through design optimization. The success of this novel device in natural conditions depends on the cell to hold the charge harvested through random, long temperature events for a couple of hours.

In conclusion, the demonstration of the novel PEC for harvesting energy from intermittent temperature changes utilizing the pyroelectric nature of PVDF and BaTiO<sub>3</sub> establishes a pathway for direct thermal to electrochemical energy conversion and a potentially promising energy harvesting technology. This research provides evidence of a new phase conversion technique in composite films and investigates the tradeoff surrounding mechanical flexibility and electroactive performance of the composite structure. The simple approach to creating porous electroactive composite thin films and understanding the impact of pore structure on the mechanical performance of the thin films puts forward several research applications. We have incorporated important features in the design of our prototype that are easily adaptable and can play a vital role in research involving: battery materials, temperature effect (high temperature, temperature ramp), aging of battery materials, etc. Most importantly, the electrochemical data and energy density calculations show the viability of the PEC in harvesting temporal thermal energy.

### 6.2 References

- [1] J. M. Kenney and S. C. Roth, "Room temperature poling of poly(vinylidene fluoride) with deposited metal electrodes.," *J. Res. Natl. Bur. Stand.*, vol. 84, no. 6, pp. 447–453, Nov-Dec 1979, doi: 10.6028/jres.084.022.
- [2] L. Ruan, X. Yao, Y. hang, L. Zhou, G. Qin, and X. Zhang, "Properties and applications of the β phase poly(vinylidene fluoride)," *Polymers (Basel)*, vol. 10, no. 3, pp. 1–27, Feb 2018, doi: 10.3390/polym10030228.
- [3] M. Olszowy, "Piezoelectricity and dielectric properties of PVDF/BaTiO<sub>3</sub> composites," in *Proc. SPIE 3181 Dielectr. Relat. Phenom. Mater. Physico-Chem. Spectrom. Investig. Appl.*, vol. 3181, pp. 69–72, Sep. 16-20, 1994, doi: 10.1117/12.276252.
- [4] B. Gusarov *et al.*, "Thermal energy harvesting by piezoelectric PVDF polymer coupled with shape memory alloy," *Sensors Actuators A Phys.*, vol. 243, pp. 175–181, Jun. 2016, doi: 10.1016/j.sna.2016.03.026.

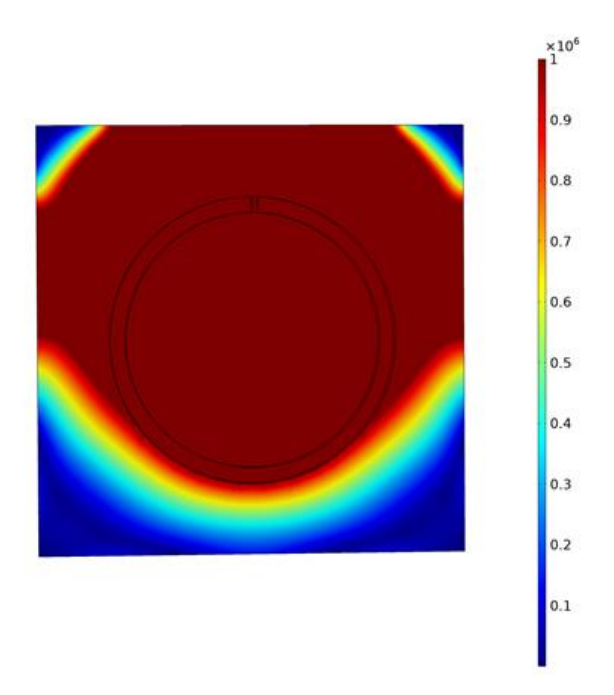


Figure 6.1: Surface plot of Von Mises stress in PVDF film for  ${<}50~\mu m$  SMA ring displacement.

# APPENDIX A

QUANTIFICATION OF  $\beta$  AND  $\gamma$  Phases

Close-up views (Figures A.1-A.3) of the FTIR spectra provided in Chapter 2 (Figure 2.3a-c) show increasing  $\beta$  phase peaks and decreasing  $\gamma$  phase peaks when BaTiO<sub>3</sub>-PVDF composite films are stretched. The characteristic  $\gamma$  phase peak at 812 cm<sup>-1</sup> remains relatively unchanged when the film is annealed, but is significantly reduced with stretching (Figure A.1).

In contrast, the emerging peaks at 464 cm<sup>-1</sup> and 445 cm<sup>-1</sup> (Figure A.2) show  $\beta$  phase formation with stretching. Thus, the FTIR results indicate an increasing  $\beta/\gamma$  ratio with mechanical drawing in the composite films. Additionally, the unique  $\gamma$  (1234 cm<sup>-1</sup>) and  $\beta$  (1276 cm<sup>-1</sup>) peaks show the same trends with stretching of the composite films (Figure A.3).

To quantitatively evaluate the electroactive  $(\beta+\gamma)$  phase fraction, the Beer-Lambert law has been used:

$$F(\beta + \gamma) = \frac{A_{\beta + \gamma}}{A_{\beta + \gamma} + 1.26A_{\alpha}} \tag{A.1}$$

where  $A_{\alpha}$  and  $A_{\beta+\gamma}$  are the absorption bands at 763 cm<sup>-1</sup> and 840 cm<sup>-1</sup>, respectively, and the factor 1.26 represents the absorption coefficient ratio of  $\beta$  and  $\alpha$  phases  $\left(\frac{K_{\beta}}{K_{\alpha}}\right)$  (Table 2.1) [1]. Some researchers have used peak-to-valley height ratios to separate electroactive PVDF phases in the FTIR results [2]. For PVDF films with multiple phases, the exclusive  $\beta$  and  $\gamma$  peaks near 1276 cm<sup>-1</sup> and 1234 cm<sup>-1</sup>, respectively, have been used with their nearest valleys to define the peak-to-valley height. Equation A.2 has been used to separate the electroactive phase content into counterparts:

$$F(\beta) = F(\beta + \gamma) \left( \frac{\Delta H_{1276}}{\Delta H_{1276} + \Delta H_{1234}} \right) \tag{A.2}$$

where  $F(\beta + \gamma)$  is the total electroactive phase, and  $F(\beta)$  is the percentages of  $\beta$  phase [2]. Figure A.4 provides a visual representation of this method.

To our knowledge this method has been only been reported with pure PVDF films, and has not been validated for composite films. The addition of BaTiO<sub>3</sub> nanoparticles affects the PVDF spectrum due to the overlap of PVDF and BaTiO<sub>3</sub> peaks and valleys in the 540-1400 cm<sup>-1</sup> region [3]. This compromises the ability to accurately quantify the electroactive phases separately in BaTiO<sub>3</sub>-PVDF composite films, and the values generated from Equation A.2 and reported in Table A.1 should be used as an estimate only, with further investigation required by other analysis methods such as XRD.

## References

- [1] R. Gregorio, M. Cestari, and F. E. Bernardino, "Dielectric behaviour of thin films of β-PVDF/PZT and β-PVDF/BaTiO<sub>3</sub> composites," *J.Mater. Sci.*, vol. 31, no. 11, pp. 2925–2930, Jun. 1996, doi: 10.1007/BF00356003.
- [2] X. Cai, T. Lei, D. Sun, and L. Lin, "A critical analysis of the  $\alpha$ ,  $\beta$  and  $\gamma$  phases in poly(vinylidene fluoride) using FTIR," *RSC Adv.*, vol. 7, no. 25, pp. 15382–15389, Mar. 2017, doi: 10.1039/c7ra01267e.
- [3] M. Singh, B. C. Yadav, A. Ranjan, M. Kaur, and S. K. Gupta, "Synthesis and characterization of perovskite barium titanate thin film and its application as LPG sensor," *Sens. Actuators B Chem.*, vol. 241, pp. 1170-1178, Mar. 2017, doi: 10.1016/j.snb.2016.10.018.

Table A.1: Calculated  $F(\beta)$  content in the composite films using Equation A.2.

BaTiO <sub>3</sub> content	Sample	F(β)
5 wt%	Annealed	$30\% \pm 10\%$
	Stretched	$40\% \pm 10\%$
10 wt%	Annealed	$34\% \pm 5\%$
	Stretched	$51\% \pm 5\%$

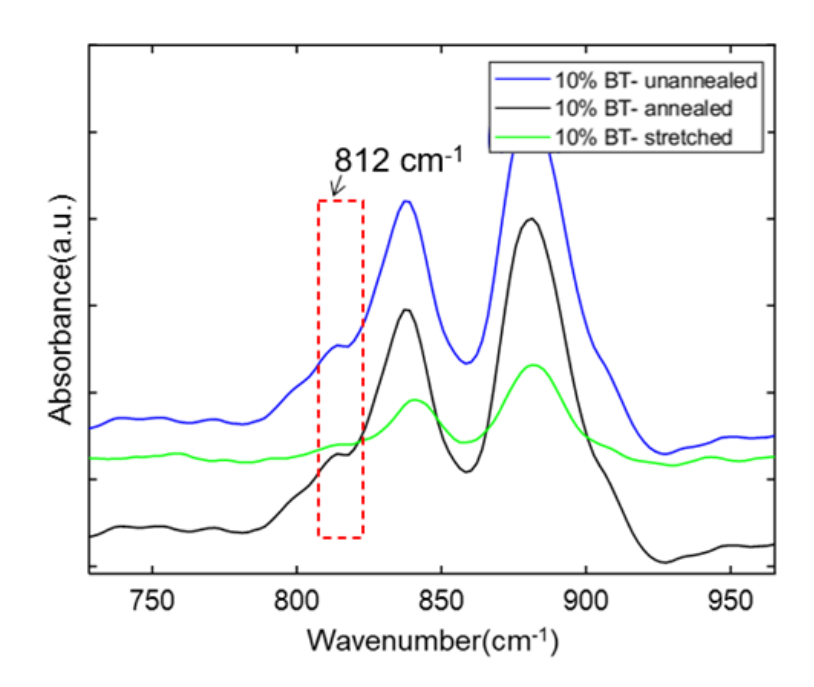


Figure A.1: FTIR spectra showing the decrease in  $\gamma$  phase shoulder at 812 cm<sup>-1</sup> due to stretching.

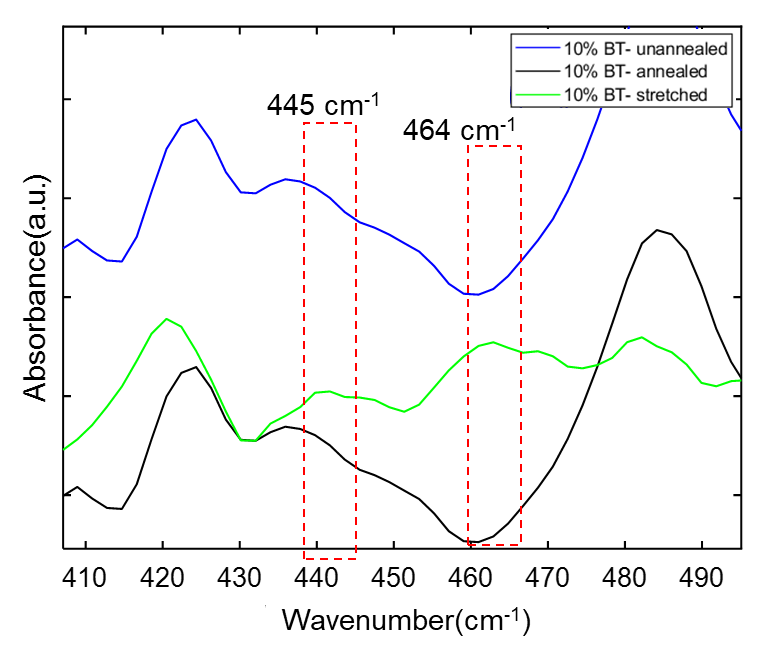


Figure A.2: FTIR spectra showing the formation of  $\beta$  phase peaks at 445 cm<sup>-1</sup> and 464 cm<sup>-1</sup> after stretching.

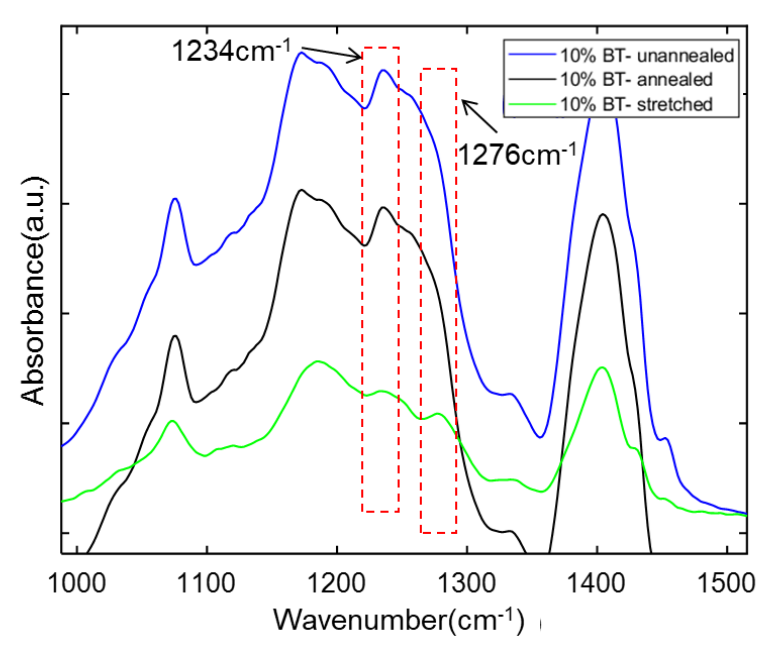


Figure A.3: FTIR spectra show increasing unique  $\beta$  phase (1276 cm<sup>-1</sup>) and decreasing unique  $\gamma$  phase (1234 cm<sup>-1</sup>) peaks with stretching of BaTiO<sub>3</sub>-PVDF composite films.

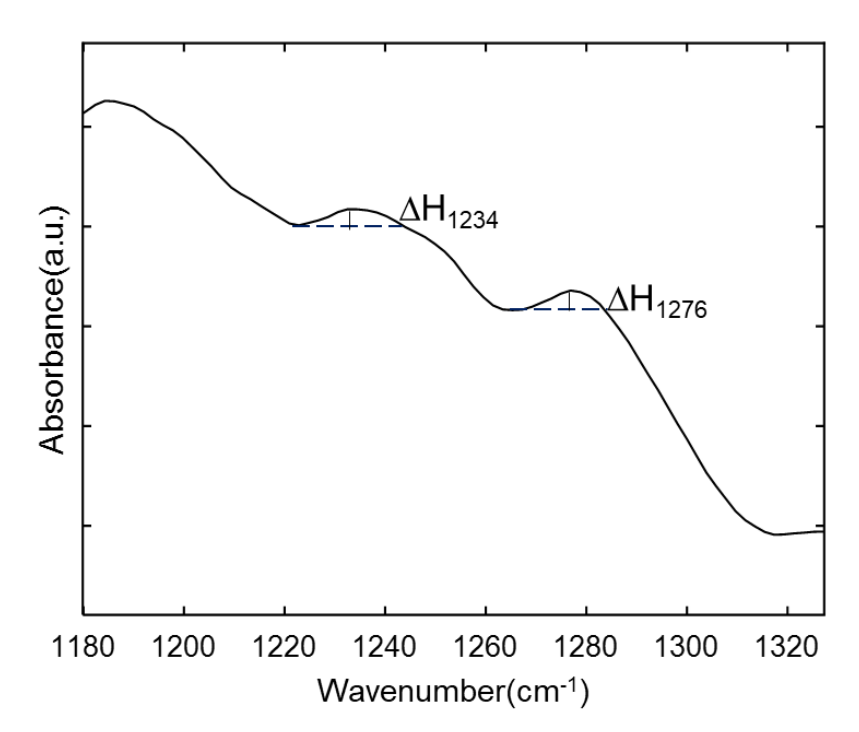


Figure A.4: Visual representation of the  $H_{1234}$  and  $H_{1276}$  peak-to-valley height in Equation A.2.

# APPENDIX B

MANUFACTURING DETAILS

Mechanical drawings (Full-page PDF versions of all drawings and CAD files are available at: https://advancedenergy.mech.utah.edu/projects/heated-spectroelectrochemical-cell-designs/).

Table B.1: Cuvette cell bill-of-materials.

Item	Part Name	Part Source	
1	Cuvette collar	3D printed	
2	Cuvette lid	Machined as per part drawing-mcmaster.com/9083K35	
		(Figure B.1a)	
3	Cuvette body	Amazon Part No. B00914AE5W	
4	Silicone Gasket	Cut from mcmaster.com/6459N121	
5	Leg Inserts (x2)	3D printed (Figure B.1c)	
6	Steel Tube	mcmaster.com/50415K61	
7	Nuts (x2)	mcmaster.com/90480A003	
8	Screws	mcmaster.com/92196A074	
9	Frame 1 (0.3off)	3D printed (Figure B.1d)	
10	Frame 2 (0.5off)	3D printed (Figure B.1e)	
11	Conducting Sleeve	Machined as per part drawing- mcmaster.com/9083K35	
		(Figure B.1b)	
12,	Current Collector 1,	Cut to desired shape using appropriate wire mesh	
13	2		
14	Separator	Cut to desired shape	
15	Wire Probe	mcmaster.com/92705K12 – Insulate using heat-shrink wrap	
16	50W Heater	walmart.com/ip/TEMPCO-HDC19102-Swaged-Cartridge-	
	D	Heater-180W-sqIn/44005079	
	Parts used but not shown in Figure 4.1a		
17	Thermocouple	https://www.jkem.com/product/thin-wire-thermocouple/	
	(Type K Teflon- Coated)		
18	Adhesive Putty	mcmaster.com/7576A2	
10	(To seal wires & TC)	memaster.com/73/0A2	
19	JB Weld Extreme	Amazon Part No. B01IBOBY74	
1)	Heat	A MINAZON I ARCINO. DO LIDOD I / 4	
	(To secure heater		
	parts)		
20	Digital outlet timer	Nearpow, model: 250h/40h/80h/20h/160h	
20	Digital datiet tiller	1100 pow, 1110 doi: 2001/1011/10011/2011/10011	

Table B.2: Disc cell bill-of-materials.

Item	Part name	Part Source	
1	Nylon Screw	2-56x 3/32 Nylon screw	
		mcmaster.com/92929A108	
2	Viewing Window	1/16 " PETG sheet (12"x12")	
		mcmaster.com/85815K11 (Figure B.2c)	
3	Conductor sheet	3/16" 316 steel bars	
		mcmaster.com/9083K35 (Figure B.2b)	
4	PTFE Insulator	0.001" PTFE film (3"x6")	
		mcmaster.com/ 8569K13 (Figure B.2d)	
5	O-ring	16 mm O-ring	
		mcmaster.com/9263K113	
6,8	Current Collector	Cut to desired shape using appropriate wire mesh	
	1,2		
7	Separator	Cut to desired shape	
9	Disc base	1 diameter 316 stainless steel rod	
		mcmaster.com/89325K24 (Figure B.2a)	
10	TEC heater	Peltier heater	
		digikey.com/TEC-20-33-31/9741968	

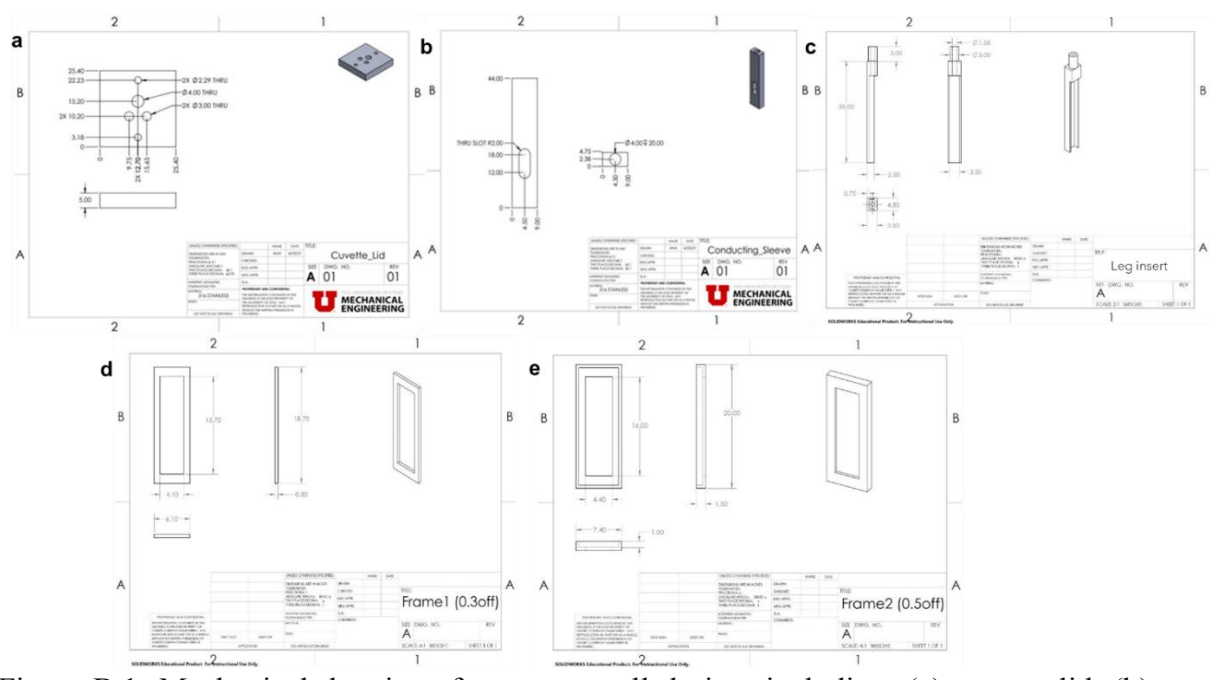


Figure B.1: Mechanical drawings for cuvette cell design, including: (a) cuvette lid, (b) conducting sleeve, (c) leg inserts, (d) Frame 1, (e) Frame 2.

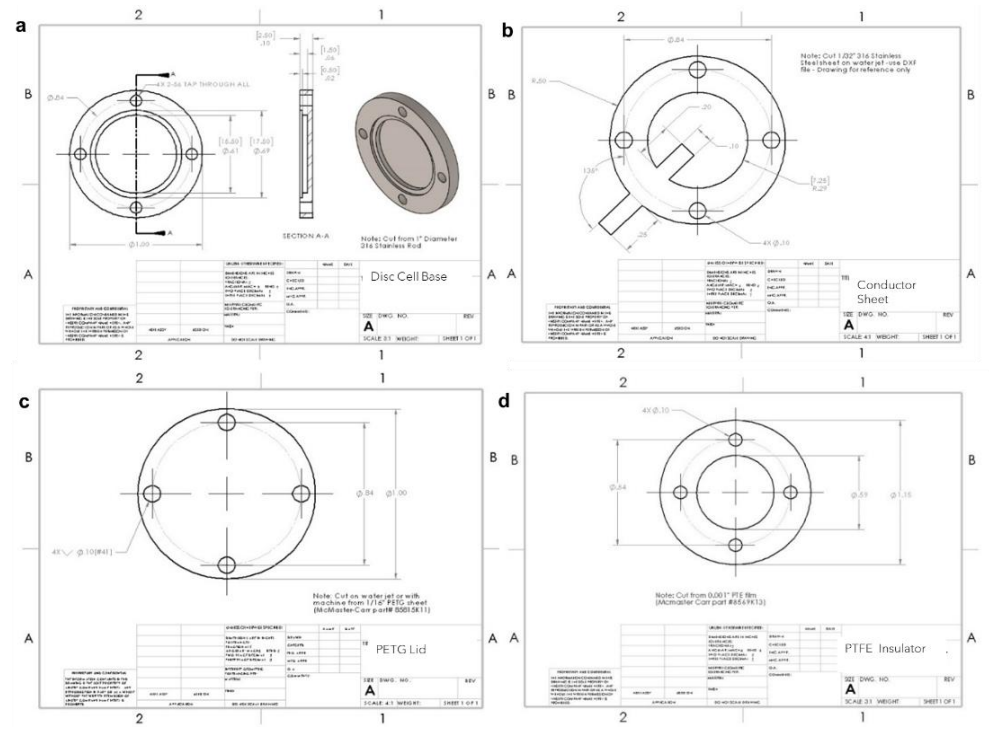


Figure B.2: Mechanical drawings for disc cell design, including: (a) disc cell base, (b) conductor sheet, (c) PETG lid, (d) PTFE insulator.

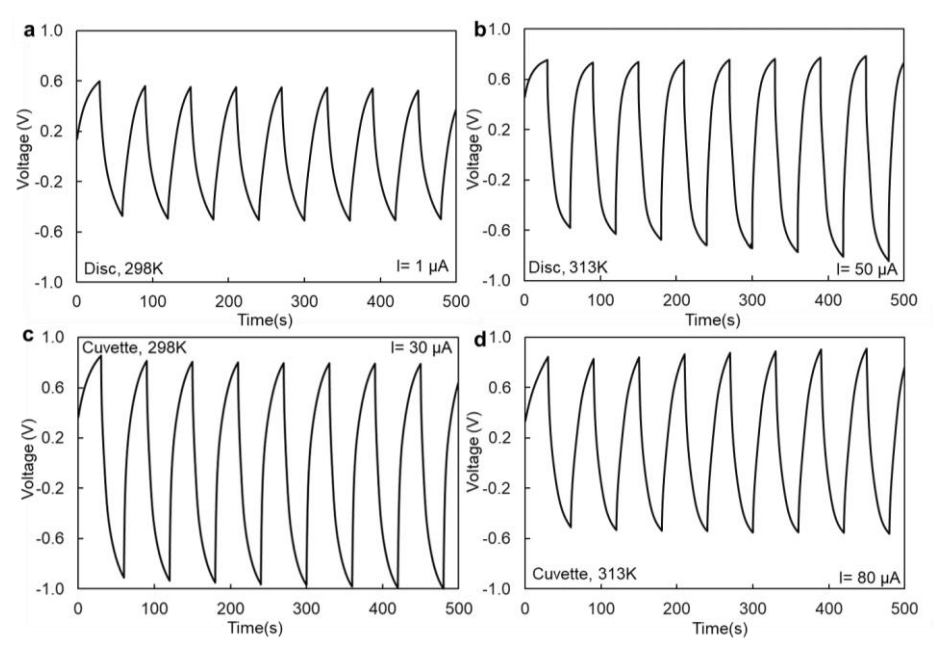


Figure B.3: Repeated chronopotentiometry measurements of graphite-graphite supercapacitor cells tested using: a) disc cell at 298 K (room temperature), b) disc cell at 313 K, c) cuvette cell at 298 K, d) cuvette cell at 313 K. Charge-discharge current was adjusted to maintain a 60 s discharge across tests.